RESOLUTION OF DIGITAL ELEVATION MODEL ON THE DEVELOPMENT OF FLOOD MODELS IN SHIRORO DAM, NIGERIA

BY

ADESINA, Ekundayo Abayomi

PhD/SET/2016/906

DEPARTMENT OF SURVEYING AND GEOINFORMATICS
FEDERAL UNIVERSITY OF TECHNOLOGY
MINNA

OCTOBER 2023

Abstract

Flooding is one of the most devastating natural disasters, occurring annually in many parts of the world. It remains a significant natural hazard despite recent advances in the scientific mechanisms causing it and increased expenditure on flood defenses. Floodplains are a desirable location for communities in the areas with the highest concentrations of people and property; they have been utilized globally for food production, frequently under the control of physical infrastructure (such as levees or dams), and have reduced these advantages and made agricultural production and related human settlements vulnerable to flood damage. As a result of the abundance of barriers that are utilised for hydropower generation, irrigation, and fish farming, the risk is always significant for individuals who reside in floodplains. Developing flood models is imperative for policymakers to make timely decisions about emergency responses and future planning. However, the accuracy of such models relies on the nature of the resolution of the Digital Elevation Models (DEM) used in their development. The study investigates the impacts of 1 m resolution Unmanned Aerial Vehicle (UAV)-derived DEM, 10 m resolution Interferometric Synthetic Aperture Radar (InSAR)-derived DEM, and 30 m resolution Shuttle Radar Topographic Mission (SRTM)-derived DEM) in flood modelling along the floodplain of Shiroro Dam, Niger State, Nigeria. The performance of the three DEMs for flood modelling was examined with the aid of flood inundation modelling (3D analyst) tools in the ArcScene environment of ArcGIS 10.4, using results obtained from the Shallow Water Equation (SWE) as initial input. The choice of materials and methods used is in parts of this work. Using the shallow-water equation (evaluated using MATLAB by integrating obtained river channel bathymetric information and topographic information from the three DEMs as input), the study determined the discharge volume, discharge rate, and flow velocity at some identified nodes along the river channel and its tributaries, thus providing a basis for determining possible flood levels within the study area. The flood levels were identified for each of the three DEMs using the start and end nodes as major identification points along the 12 river channels in the study area. Flood levels of 150 m and 250 m were identified for the UAV-derived DEM, while for the InSAR 10 m DEM, 160 m and 270 m were identified. The flood levels SRTM 30 m DEM were 200 m and 280 m. Flood events covering the two flood levels were then simulated in the ArcScene environment of ArcGIS 10.4 software to estimate the vulnerability of settlements within the study area. Comparing the impacts of the UAV-derived 1 m resolution data with InSAR 10 m resolution and SRTM 30 m resolution data yields Root Mean Square Errors (RMSE) of 0.249 m, 0.352 m, and 0.455 m, respectively. The analysis, however, showed that the UAV-derived 1 m DEM reliably predicted the flood risk situation due to its high resolution of the other two DEMs, InSAR 10 m and SRTM 30 m, which produced higher estimate of the the flood risk situation in the study area. Thus, the accuracy of the DEM plays a significant role in generating flood inundation maps by adequately presenting the topographic data of the river channel and the floodplain. DEMs with higher resolution and accuracy provide more reliable maps for flood simulations. The study recommends that low-resolution derived DEMs from InSAR 10 m and SRTM 30 m are insufficient for flood hazard estimation; higher-resolution UAV-derived 1 m DEM.

TABLE OF CONTENTS

CHAPTER ONE

1.0   INTRODUCTION

CHAPTER TWO

2.0   **LITERATURE REVIEW**

CHAPTER THREE

3.0   **MATERIALS AND METHODS**

LIST OF FIGURES

LIST OF TABLES

LIST OF APPENDICES

LIST OF ABBREVIATIONS

Abbreviation	Meaning
1D	One-dimensional
2D	Two-dimensional
3D	Three-dimensional
ASTER GDEM	Advanced Spaceborne Thermal Emission Reflection Radiometer Global Digital Elevation Map
CHP	Check points
DEM	Digital elevation model
DEFRA	Department for environment, food and rural affairs
DSM	Digital Surface Model
DTM	Digital Terrain Model
ES	Echo Sounder
ESD	Electrostatic Discharge
ESA	European Space Agency
ESRI	Environmental Systems Research Institute, Inc.
FFT	Fast Fourier Transformation
GE	Google Earth
GC	Ground Control
GFDRR	Global Network for Disaster Risk
GIS	Geographic Information System
GPS	Global Positioning System
GUI	Interface of Interferogram Formation
GNSS	Global navigation satellite system
GCP	Ground Control Point

GEV	Generalized Extreme Value Distribution
GCS	Ground Control Station
HEC-RAS	Hydrologic Engineering Centre-River Analysis System
HAND	Height Above Nearest Drainage
HEC-RAS	Hydrologic Engineering Center- River Analysis System
HSG	Hydrological Soil Group
IDP	Internally Displaced Persons
IDF	Inflow Design Flood
INSAR	Interferometric Synthetic Aperture Radar
INS	Inertial Navigation System
IW	Interferometric Wide Swath
KFF	Kemler File Format
LiDAR	Light Detection and Ranging
LGA	Government Areas
MAE	Maximum Absolute Error
MATLAB	Matrix Laboratory
MPP	Maximum Posteriori Probability
MWL	Mean Water Level
MSL	Mean Sea Level
NIGIS	Niger State Geographic Information System Agency

LIST OF ABBREVIATIONS

Abbreviation	Meaning
NIMET	Nigerian Meteorological Agency
NSEMA	Niger State Emergency Management Agency
NHSA	Nigerian Hydrological Services Agency
NEMA	National Emergency Management Agency
NASA	National Aeronautics and Space Administration
OEHHA	Office of Environmental Health Hazard Assessment
PMF	Probable Maximum Flood
PBIAS	Percent Bias
RC	Radio Connection
RS	Remote Sensing
RRI	Rainfall Runoff Inundation
RMSE	Root Mean Square Error
RRMSE	Relative Root Mean Square Error
SAR	Synthetic Aperture Radar
SRTM	Shuttle Radar Topographical Mission
SNAP	Sentinel Applications Platform
SNAPHU	Statistical-Cost Network-Flow Algorithm for Phase Unwrapping
SLC	Single-Look Complex
SLG	Slugging Percentage
SWAT	Soil and Water Assessment Tool
SWE	Shallow Water Equation
UAV	Unmanned Aerial Vehicle

LIST OF ABBREVIATIONS

Abbreviation	Meaning
UN	United Nations
USA	United State of America
US	United States
UTM	Universal Transverse Mercator
UNISDR	United Nations International Strategy for Disaster Reduction
UNESCO	United Nations Educational, Scientific and Cultural Organization
NEMA	National Emergency Management Agency of Nigeria
NSEMA	Niger State Emergency Management Agency
NIMET	Nigerian Meteorological Agency
VE	Venant Equation
VH	Vertical-Horizontal
VV	Vertical-Vertical
WB	World Bank
WGS	World Geodetic System

LIST OF SYMBOLS

Symbol	Meaning
Q	Discharge
A	Cross-sectional area
$\frac{\partial Q}{\partial t}$	Rate of discharge with respect to time
$\frac{\partial}{\partial x}\left(\frac{Q^2}{A}\right)$	Rate of discharge with respect to cross-sectional area
g	Acceleration due to gravity
S_f	Frictional slope
S_o	Reference slope
$\frac{\partial h_o}{\partial x}$	Channel bed-topography
R	Hydraulic radius
n	Manning coefficient of roughness
A	Cross-sectional area
S	Channel slope in the direction of flow
$\frac{\partial h_o}{\partial x}$	Obtained from the bathymetric observation
F_r	Flow rate
L	Length of reach
C	Coefficient or correction factor
T	Time in seconds
W_f	Water flux
$W_f > Q$	River section is potentially flood prone
$W_f \leq Q$	River section is not potentially flood prone

LIST OF SYMBOLS

Symbol	Meaning
φ	Signal phase
ρ	Signal range/distance measured
λ	Signal wavelength
n	Observation noise
z	Elevation of point
h	Height of satellite above ground level
θ	Azimuth

CHAPTER ONE

1.0   INTRODUCTION

1.1   Background to the Study

Natural factors like river overflow from precipitation, severe occurrences like hurricanes and earthquakes, and artificial factors like dam failures and expansion on floodplains are all potential causes of flooding (Mishra and Satapathy, 2021; Almoradie *et al.,* 2020). Floodplains are a desirable location for communities in the areas with the highest concentrations of people and property (Fang *et al.,* 2020). These floodplains have been utilized globally for food production, frequently under the control of physical infrastructure (such as levees or dams), which has reduced these advantages and made agricultural production and related human settlements vulnerable to flood damage. As a result of the existence of dams that are utilised for hydropower generation, irrigation, and fish farming, the risk is always significant for individuals who reside in floodplains (Adesina *et al.,* 2021).

The dams are often constructed with concrete or natural materials like rock and dirt, but they are occasionally severely built, poorly maintained, and situated close to human settlements. At the peak of rainy seasons, they have the potential to overflow, causing torrents of water to inundate floodplain communities. The water released by dam authorities also has a major when the floodplain of the reservoir is flooded. A strategy that would have reduced losses and suffering in the long term could have been undertaken if the extent and likely severity of the damages were understood. Unfortunately, poverty is widespread in emerging nations like Nigeria, where people heavily depend on the floodplains for their financial stability.

Consequently, it is impossible to expect the people who live in floodplains to relocate to other areas; hence, strategies must be developed to lessen the suffering caused by such occurrences. Yin *et al.* (2020), on the other hand, proposed a successful method of controlling flood risks, which is flood forecasting and early warning. This plan may include flood prevention, monitoring, recovery, readiness, and risk control (Wang *et al.,* 2020). In industrialized nations, studies on flood modelling are becoming more and more popular (Puno *et al.,* 2018). The use of higher resolution DEMs in flood inundation mapping, which results in more precise flood maps, has been the subject of several research (Puno *et al.,* 2015; Adesina *et al.,* 2021). The amount of ground surface area each cell in a DEM covers is known as its spatial resolution. Therefore, a higher-resolution digital elevation model (DEM) better represents topography since it has more cells per unit area than a lower-resolution DEM (ESRI, 2014a).

The utilisation of remote sensing technology has revolutionised the ability to monitor and comprehend the dynamic nature of the Earth's surface, offering valuable insights for various applications, including flood modelling (Jafarzadegan and Merwade, 2017; Hawker *et al.,* 2018; Bhuyian and Kalyanapu, 2018). Floods are natural disasters that cause widespread economic and environmental damage across the globe (Sanders *et al.,* 2020). Accurately predicting and modelling floods are crucial for effective disaster management, risk assessment, and mitigation strategies (Jones *et al.,* 2020). In recent years, researchers have increasingly emphasised the use of high-resolution Digital Elevation Models (DEMs) derived from remote sensing data to enhance the precision of flood models (Jafarzadegan and Merwade, 2017; Hawker *et al.,* 2018; Bhuyian and Kalyanapu, 2018).

Rainfall patterns, climatic changes, and global warming are a few factors that affect the occurrence and intensity of floods (Sanders *et al.,* 2020). Climate change-induced alterations in precipitation patterns, including increased rainfall intensity and frequency, have been observed in many regions (Jones *et al.,* 2018). Nigeria, for instance, encountered devastating flood events in 2012 that resulted in damages exceeding $16.9 billion, impacting property, oil production, agriculture, and other sectors (Komolafe, 2021; Egbenta *et al.,* 2015). These changes have heightened the risk of flooding in various areas, necessitating the development of reliable flood models capable of capturing the intricate dynamics of water movement and inundation. In flood modelling, the influence of DEM resolution on flood property estimation has been an ongoing area of research. DEMs serve as vital inputs by providing detailed information about the topography and elevation of the terrain (Jafarzadegan and Merwade, 2017). Higher resolution DEMs enable a more accurate representation of the land surface, which is essential for precise simulation of flood behaviour, such as flow pathways, floodplain extent, and flood depths (Hawker *et al.,* 2018). Various remote sensing techniques have been employed over the years to acquire DEM data at different resolutions, including Unmanned Aerial Vehicles (UAVs), Interferometric Synthetic Aperture Radar (InSAR), and the Shuttle Radar Topography Mission (SRTM), among others (Bhuyian and Kalyanapu, 2018).

UAVs are versatile and cost-effective tools for collecting high-resolution data. With advanced imaging sensors and LiDAR technology, UAVs can capture detailed topographic information at resolutions ranging from centimeters to meters (Jawak *et al.,* 2019). This fine-grained spatial resolution identifies small-scale topographic features, such as ditches, culverts, and artificial structures, significantly influencing flood flow patterns (Gupta *et al.,* 2020).

InSAR, another remote sensing technique, uses satellite-based radar systems to measure changes in surface elevation. Particularly in regions where complex terrain or cloud cover limits traditional topographic mapping techniques, inSAR has demonstrated its efficacy in producing accurate and high-resolution DEMs (Li *et al.,* 2020). The application of InSAR in deriving DEMs for flood modelling has led to an improved understanding of flood dynamics on a regional scale (Zhang *et al.,* 2019).

Shuttle Radar Topography Mission (SRTM) is a spaceborne radar mission that offers global DEM coverage with a relatively coarse resolution of approximately 30 meters (Farr *et al.,* 2007). Despite its coarse resolution, SRTM data has been extensively employed in flood modelling due to its global coverage and consistent data quality (Bhuyian and Kalyanapu, 2018). It has proven valuable for large-scale flood risk assessments and initial flood model development in regions with limited data availability (Jafarzadegan and Merwade, 2017). Other remote sensing methods, like airborne LiDAR, aerial photogrammetry, and satellite-based optical imagery, offer different resolutions and capabilities for DEM acquisition (Hawker *et al.,* 2018). Each technology presents unique advantages and limitations, influencing the suitability of DEM data for flood modelling purposes.

Given the crucial role of accurate and high-resolution DEMs in flood modelling, this study aims to explore the impact of DEMs derived from different remote sensing platforms with varying resolutions on the development of flood models. By comparing and evaluating their impacts on flood models using DEMs of different resolutions, the aim is to enhance the understanding of the relationship between DEM resolution and flood modelling accuracy (Jafarzadegan and Merwade, 2017; Hawker *et al.,* 2018; Bhuyian and Kalyanapu, 2018). This research will contribute to advancing flood prediction and

mitigation strategies, ultimately assisting in improved disaster management and planning for flood-prone regions.

1.2   Statement of the Research Problem

A DEM's spatial resolution is defined as the amount of ground surface area that each cell covers. Hence, a higher-resolution DEM contains more cells per unit area than a low-resolution DEM, which more accurately depicts topography (ESRI, 2014a). The development of flood models heavily relies on the accuracy and resolution of Digital Elevation Models (DEMs) derived from remote sensing data (Jafarzadegan and Merwade, 2017; Hawker *et al.,* 2018; Bhuyian and Kalyanapu, 2018). While the availability of different remote sensing platforms and techniques offers varying resolution DEMs, the impact of these resolutions on the accuracy and reliability of flood models remains to be determined (Jones *et al.,* 2020).

Recent literature has shown instances where flood models produced from various DEM sources, such as the SRTM and InSAR, have resulted in overprediction (Hawker *et al.,* 2018; Bhuyian and Kalyanapu, 2018). However, the literature needs more discussion regarding the flood models produced by these DEM sources that have demonstrated accuracy or optimal prediction capabilities. The impact of DEMs derived from UAVs, InSAR, SRTM, and other remote sensing mediums on the development of flood models and their influence on the accuracy of flood predictions and mitigation strategies investigated.

To provide a contextual background for the study, Niger State in Nigeria is selected as a relevant location due to its frequent exposure to flooding. The state experiences many natural catastrophes and significant damage caused by flooding, according to the National Emergency Management Agency (NEMA, 2019). However, the state's disaster

preparedness efforts could be improved by the need for baseline data and coordinated measures to mitigate the effects (Komolafe *et al.,* 2020; Komolafe *et al.,* 2021). This study problem arises from the need for more accurate and detailed flood models in the face of increasing rainfall intensities, changing climate patterns, and the potential influence of global warming on flood dynamics.

Understanding how different DEM resolutions obtained from various remote sensing platforms affect flood model accuracy is crucial for effective flood prediction, risk assessment, and mitigation strategies. The study investigated the impact of DEM resolution on flood modelling accuracy using UAVs, InSAR, and SRTM DEMs. The findings improved flood prediction, risk assessment, and mitigation strategies, not only in Niger State but also in similar regions facing similar challenges internationally.

1.3   Research Questions

The study answered the following questions:

i.   What are the topographic accuracies of UAV 1 m, InSAR 10 m, and SRTM 30 m DEMs?

ii.   How can the topographic accuracy of a high-resolution DEM of the study area be determined from the UAV data?

iii.   How can the flood extent of the study area be modelled accurately from UAV, InSAR, and SRTM DEMs?

iv.   Compared to UAV-derived data, how reliable are the DEMs from InSAR 10 m and SRTM 30 m for flood modelling?

1.4   Aim and Objective of the Study

The purpose of this study is to investigate the impact of resolution DEM topographic data requirements for the development of an optimal flood vulnerability model in the communities downstream of the Shiroro dam in Nigeria to improve future flood risk assessment for the area and other areas with similar physical characteristics.

The specific objectives of achieving the research goal are to:

i.   determine the topographic accuracies of the UAV 1 m, InSAR 10 m DEM and the open-source SRTM 30 m DEM.

ii.   generate a high-resolution DEM of the study area from primary UAV data and ascertain its topographic accuracy.

iii.   develop an accurate flood extent modelling approach using UAV, InSAR 10 m, and SRTM 30 m DEMs for enhanced flood prediction in the study area.

iv.   examine the accuracy of flood modelling using the various DEM sources (objectives 1–3) using NSEMA data.

1.5   Justification for the Study

The justification for conducting this study lies in the critical need for accurate flood modelling in the face of increasing rainfall intensities, changing climate patterns, and the potential influence of global warming on flood dynamics. By investigating the impact of high-resolution DEMs derived from various remote sensing platforms on flood modelling, researchers can better understand how to improve flood predictions and mitigation strategies. Previous studies have explored the impact of DEM resolution on flood property estimation (Jafarzadegan and Merwade, 2017; Hawker *et al.,* 2018; Bhuyian and Kalyanapu, 2018), research by Azizian and Brocca (2020) has highlighted

the importance of optimal resolution DEMs rather than solely relying on the highest resolution.

Evaluating remote sensing technologies such as Unmanned Aerial Vehicles (UAVs), Interferometric Synthetic Aperture Radar (InSAR), and the Shuttle Radar Topography Mission (SRTM), as well as other mediums like airborne LiDAR, aerial photogrammetry, and satellite-based optical imagery, will contribute to understanding their suitability and limitations in flood modelling applications. By comparing and evaluating the performance of flood models using different resolution DEMs, this study aims to uncover the relationship between DEM resolution and flood modelling accuracy. These insights will aid researchers and practitioners in selecting the most appropriate remote sensing platforms for acquiring DEMs based on specific project requirements and resource constraints.

The significance of accurate and high-resolution DEMs in flood modelling cannot be overstated (Jafarzadegan and Merwade, 2017; Hawker *et al.,* 2018; Bhuyian and Kalyanapu, 2018). These DEMs provide crucial topographic information that enables precise simulation of flood behaviour, including flow pathways, floodplain extent, and flood depths. By improving flood model accuracy by evaluating high-resolution DEMs, this research will advance flood prediction and mitigation strategies, enabling better disaster management and planning for regions prone to flooding.

This study's findings will enhance flood prediction accuracy and support effective disaster management, risk assessment, and mitigation strategies. It will lead to better preparedness and response strategies, potentially saving lives and minimising economic and environmental damage caused by floods (Jafarzadegan and Merwade, 2017; Hawker *et al.,* 2018; Bhuyian and Kalyanapu, 2018).

Flood risk assessment and management rely on accurate flood models to understand the spatial extent, intensity, and potential impacts of flooding (Azizian and Brocca, 2020). This study will provide more robust flood risk assessment and management tools by improving flood model accuracy by evaluating high-resolution DEMs. Based on these enhanced models, policymakers, urban planners, and emergency response teams can make informed decisions and implement proactive measures to reduce flood risks.

In conclusion, the justification for this study is rooted in its potential to enhance flood prediction accuracy, address climate change challenges, evaluate remote sensing technologies, guide data collection strategies, and support flood risk assessment and management. The practical implications of the findings will benefit flood modelling practitioners, researchers, and decision-makers, ultimately contributing to more effective flood disaster planning, response, and mitigation efforts.

1.6   Scope of the Study

The scope of this study encompasses a specific geographical area, namely Niger State in Nigeria, known for its frequent exposure to flooding. The study's which are the settlements to be covered are situated downstream of the Shiroro Dam in Shiroro Local Government Area of Niger State, Nigeria, between longitudes 6^0 20' and 6^0 50' and latitudes 9^0 50' and 10^0 10' north, with a population of 404,200 people and a total land area of 4,700 km^2 National Population Commission (NPC, 2006). The study covered 50 km by 40 km in length and breadth from the spillway gate of the dam to the downstream, which comprises all the vulnerable settlements.

The study focused on evaluating the impact of the resolution of Digital Elevation Models (DEMs) derived from various remote sensing platforms, such as Unmanned Aerial

Vehicles (UAVs), Interferometric Synthetic Aperture Radar (InSAR), and shuttle radar topography missions (SRTM), on flood modelling accuracy.

Regarding the study population, the research considered the entire communities downstream of Shiroro Dam, Niger State, and its associated river channels prone to flooding (NEMA, 2019). The coverage encompassed areas with known flood risk and historical flood events, focusing on rivers and their surrounding regions. The study acquired relevant data and DEMs that cover the selected study area, emphasizing obtaining comprehensive coverage to ensure a representative sample of the terrain. Data acquisition involves utilising remote sensing technologies to collect the necessary information. It includes obtaining high-resolution DEMs from UAVs, InSAR, and low-resolution SRTM. The data acquisition methods and platforms are determined based on their suitability for capturing accurate topographic information in the study area.

The acquired data have undergone processing to generate the high-resolution DEMs required for flood modelling purposes. The hydrological data for 20 years include rainfall, temperature, inflow, water level, and outflow (water discharge). The study's findings, based on analysed and compared different spatial resolution DEMs for flood models, look at how accurate and reliable this model is at simulating flood behaviour, such as flow paths, floodplain size, and flood depths. The study assessed the impact of DEM resolution on flood modelling accuracy and identified the limitations and strengths of each remote sensing platform for flood modelling.

The overall scope of this study is limited to the Shiroro downstream community area. The study emphasises data acquisition, processing, and analysis, aiming to provide insights into the relationship between DEM resolution and flood modelling accuracy and the

suitability and limitations of different remote sensing technologies in flood modelling applications.

1.7   Study Area

The study area was divided into the following themes: location, climate, rainfall, relief and drainage, hydrology, economic activities, vegetation, and land use, which were discussed in subsections 1.8.1 to 1.8.8.

1.7.1   Description of the study area

Shiroro Dam is 550,235 meters downstream of the Kaduna River's main tributary, the River Dinya. The River Kaduna, which originates in the western and northern portions of the Jos Plateau in north-central Nigeria and flows west and southwest from there, is the source of the dam. The rivers Koriga, Maarigna, and Durimi are the principal tributaries of the River Kaduna (Ikusemoran *et al.,* 2014).

The study's vulnerable villages were situated in Niger State, Nigeria, downstream of the Shiroro Dam, between longitudes 60 20' and 6^0 50' and latitudes 9^0 50' and 10^0 10' north. The map of the study area is presented in Figures 1.1 to 1.3, where Figure 1.1 shows the map of Nigeria where the map of Niger State was extracted, Figure 1.2 displays the map of Niger State where the map of the study area was extracted, and Figure 1.3 depicts the map of the study area. With a population of over 4 million, Niger State has a total land area of 72,397.81 km^2. The Niger Valley terrain covers 18,007.38 km^2 (24.94%), the plains cover 24,181.04 km2 (33.49%), the upland is 20616.09 km^2 (28.55%), and the remaining 9593.3 km^2 (13.02%) are made up of highlands (Mayomi *et al.,* 2014).
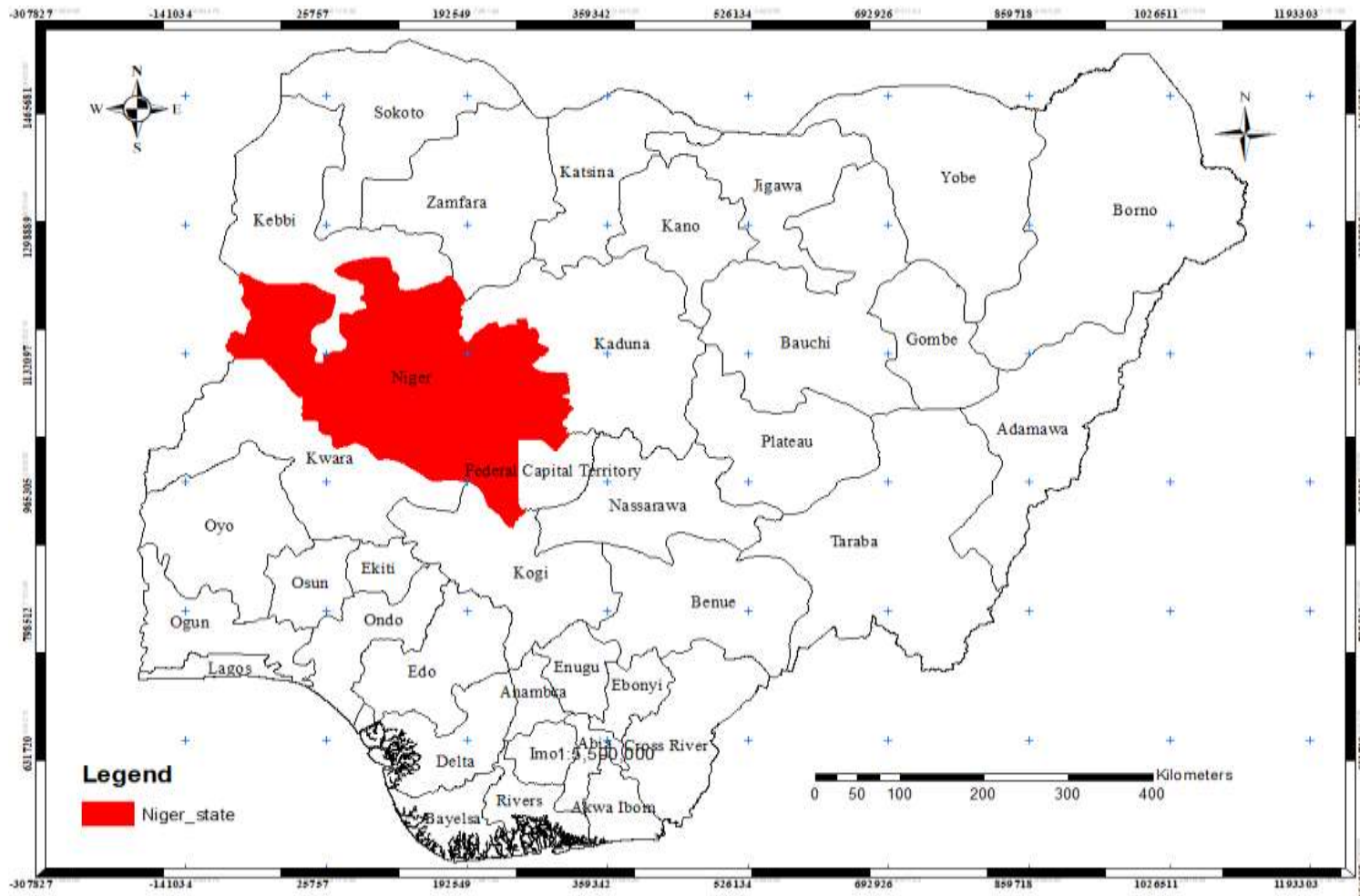
Figure 1.1: Nigeria map

Source: Niger State Ministry of Lands and Survey Department, Minna, 2017
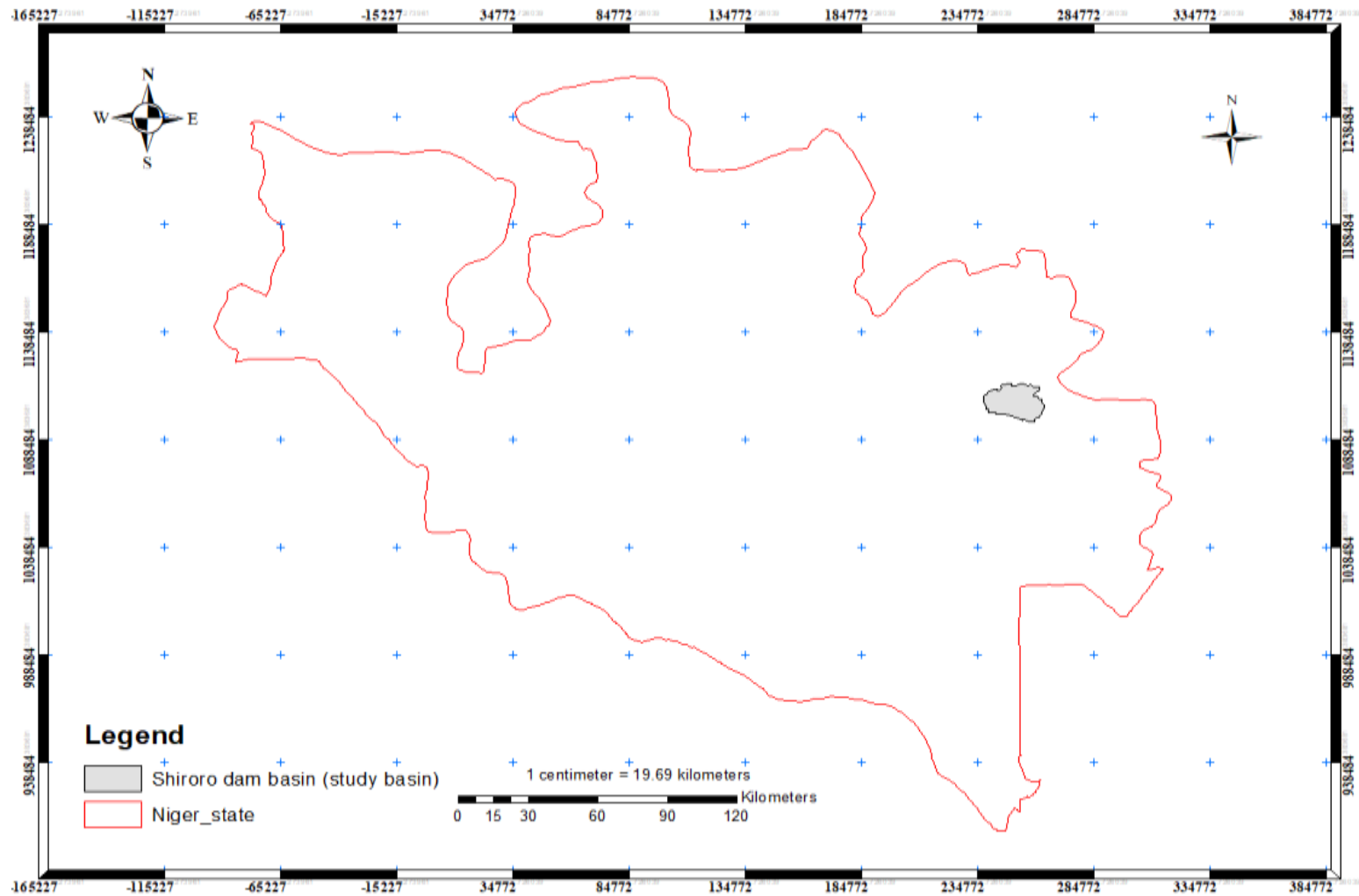
Figure 1.2: Niger State map

Source: Niger State Ministry of Lands and Survey Department, Minna, 2017
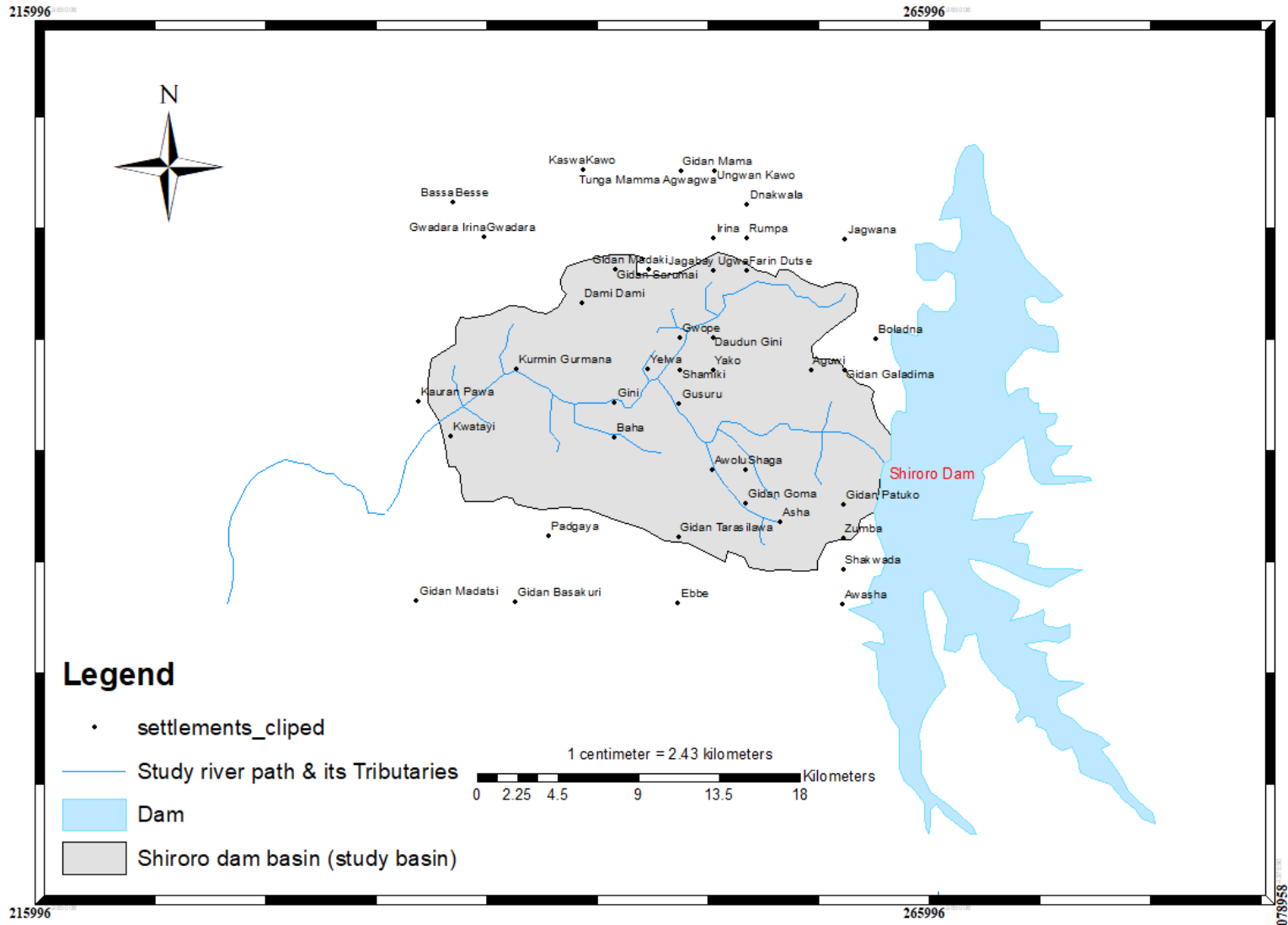
Figure 1.3: Study area map

1.7.2 Climate of the study area

According to Koppen's classification system, the study region's climate falls under the wet and dry (AW) group. The year-round minimum temperature often occurs between December and January, while the highest temperature, about 35°C, is recorded between March and June (Niger State, 2012). In addition, the study area is generally hot all year round, lying within the tropical zone with variation between winter and summer, the wet season from April to October, and the dry season from November until March (Yakubu, 2012). January through March sees very little rainfall, with an average of 5 mm in January and 40 mm in the far southwest in March.

The extreme Northwest experienced the least precipitation, 40 mm, with the North Central section of the study area receiving 70 mm or more by April. During May and July, the Shiroro Lake Watershed gets more than 100 mm, with a high of about 280–300 mm in July. All sections of the North Central Watershed get between 180 and 200 mm of precipitation during the study area's peak wet months of July, August, and September.
In the western portion of the region, rainfall totals exceed 300 mm. In a typical rainy year, September should see the highest rainfall totals of around 400 mm; in a dry year, that total may dip as low as 130–150 mm. The length of the rainy season (LRS), which runs from April 20 through May 20, lasts between 161 and 200 days.

1.7.3 Drainage pattern and relief in the study area

Shiroro Lake has an $8 \times 10 \text{ m}^3$ inflow capacity aided by about twelve smaller tributaries, with the Kaduna River serving as the primary source and constituting more than 70% of the overall capacity (Eze *et al.,* 2018). The tributaries feeding Kaduna's main rivers are the Muye, Sarkin Pawa, Guni, Koriga, Durumi, and Mariga rivers.

Unlike other rivers in northern Nigeria, the river is perennial. The upper and middle stretches of the river have a primarily straight channel, though some of them have extended sections with a low gradient in between a series of valley steps with a steep gradient. When it passes through hard rocks, its course is changed, and vast canyons have been cut across the region of the valley's more evident steeps. Height-variant and highly undulating landscapes can be found. Lowlands as low as 50 meters are common in the study region, as are solitary hills 600 meters or higher. Schist and gneiss predominate in the lower terrain, while granite rocks comprise most nearby highlands (Eze *et al.,* 2018).

1.7.4 Hydrology of the study area

The Niger and Kaduna Rivers are the two main rivers that flow through Niger State. The River Kaduna, a major tributary of the Niger River in central Nigeria, rises in the Jos Plateau and travels for over 350 km before emptying into the reservoir (Garba *et al.,* 2016). Before turning northwest to a curve 35 kilometers northeast of the Kaduna metropolis, it traverses across the Jos Plateau at Vom for 29 kilometers (Eze *et al.,* 2018). From there, it travels in a southerly and south-westerly direction for the remainder of its 550 km (340 mi) journey to the Niger at Muregi, where Shiroro Lake was built on the Kaduna River.

The presence of wet and dry seasons determines the river's flow regime. The reservoir is approximately 12.8 kilometers wide. While the dry season usually lasts from November to March, the rainy season extends from April to October and peaks in August and September (Eze *et al.,* 2018).

1.7.5 Economic activities in the study area

The main economic activities in the study area's southern lowlands, which constitute Nupe land, include the production of rice, sugarcane, and fish. At the same time, the Gbagyi villages cultivate rice in the upper floodplains of the River Kaduna. However, due to natural irrigation, rice farming is the main economic activity around Bida, Edozhigi, and Badeggi. At the same time, the Shiroro Dam's floodplain is mainly used to cultivate yam, cassava, sugar cane, and Guinea maize (Niger State, 2012).

1.7.6 Vegetation of the study area

The surrounding environment resembles a savannah, with isolated areas of mostly tree-lined woodlands and sparse patches of shrubs and grasses. The trees are short, broad-leaved plants that may grow to 16.5 m, while the grasses are between 1.5 m and 3.5 m tall. The grasses have underground solid root systems that allow them to regenerate even after being destroyed during dry season bushfires until the rains arrive the following year, in contrast to the trees that shed their leaves during the dry season to limit water loss through transpiration (Eze *et al.,* 2018).

1.7.7 Soil of the study area

Impermeable soils and rocks such as clay or shale are the most common soil types in the study area. It has a moderately high runoff potential (50 percent sand and 20 to 40 percent clay), is well-drained and shallow to moderately deep, and ranges from dark greyish brown to dark or intense brown to yellow-red (Shiroro Local Government, 1999).

1.7.8 Land use of the study area

The region is abundant in natural resources, including water, land, and producers of rice, yams, maize, cotton, groundnuts, millet, and guinea corn, with many farmers and some fishing communities (Shiroro Local Government, 1999).

CHAPTER TWO

2.0   LITERATURE REVIEW

2.1   Theoretical Framework

The condition where river discharge exceeds the allowable bank total limits is known as a flood. Rivers typically run in clearly defined channels, but banks are overtopped in situations of excessive flow, and floodplains are submerged. Fluvial flooding is the term for this form of flooding, the type considered in this thesis. Other frequent types of flooding include coastal and pluvial flooding, resulting from coastal water inundating land due to high tides, storm surges, and excessive rainfall in metropolitan areas that run off impervious surfaces. Storm surges or significant rainfall are two causes of floods (Wahl *et al.,* 2015; Leonard *et al.,* 2014). Table 2.1 provides definitions for the major flood constituents.

Table 2.1: Definitions of the main elements of a flood

Component	Definition
Annual Flood	Maximum daily flow during a year
Bank full Discharge	Discharge at which a river channel is full to capacity.
Flood Event	A series of flows that comprise of a progressive rise, culminating in a peak and then receding to a normal flow
Flood Extent	The areal extent of flood water on a floodplain
Flood Peak	Highest elevation reached by the flood waters during a flood event
Flood Stage	Elevation of the Water Surface
Return Period	Statistical occurrence of a flood of a particular magnitude at a location. e.g. A return period of 50 years means on average a flood of that magnitude occurs once every 50 years
River flood	Excessive water over channel capacity causes flooding
Coastal flood	Oceanic impacts cause floods in the inland
Urban flood	Rapid runoff exceeds storm drainage capacity
Flash flood	Unpredictable, local rainfall-related disasters occur
Fluvial flood	Floods occur on floodplains due to overflowing streams and embankments.

Source: Wahl *et al.* (2015)

The description of floods above relates to the physical aspect of a flood, or more specifically, the flood hazard. When assets or people are exposed to a condition known as exposure, a flood turns destructive (Arnell *et al.,* 2018). Vulnerability is the ability of the exposed to foresee, manage, and withstand the impact of the hazard. It is associated with a complex interplay of socio-cultural, political-institutional, and economic aspects (Winsemius *et al.,* 2015). Flood risk, which is described as the likelihood that a flood of a given magnitude and a given loss will occur within a given period (Hanington *et al.,* 2017; Njoku *et al.,* 2020), is the result of the combination of these variables.

2.1.1 Impact of flooding

Among natural disasters, flooding is one of the significant contributors to economic losses and deaths, with the frequency of its occurrences rising annually (Sayers *et al.,* 2018); hence, flooding is a severe issue that should not be underestimated (Wing *et al.,* 2018). According to UNISDR (2015), flooding has impacted 2.3 billion people over the past 20 years, killing 157,000. The nations with higher incomes typically experience the most significant economic losses because a relatively small number of major events can have a significant impact.

Despite the already high and globally devastating impacts of floods, increasing flood events are anticipated to have more disastrous implications for several reasons. One such reason is the global warming of the environment (Hirabayashi *et al.,* 2013; Dottori *et al.,* 2018; Kundzewicz *et al.,* 2014; Winsemius *et al.,* 2015; Arnell *et al.,* 2018; Arnell and Gosling, 2016). Additionally, as the world's population continues to rise, people are anticipated to construct residential buildings in more at-risk regions due to land pressures and marginalization, increasing their vulnerability to flooding (Jongman *et al.,* 2012). It

is anticipated that those most susceptible to inundation will be disproportionately more impacted by it in the future (Sayers *et al.,* 2018).

Flooding has continued to be a significant environmental issue in Nigeria. Available studies have shown that there is a frequent occurrence of flooding (Ishaya *et al.,* 2009; Kolawole *et al.,* 2011; Olajuyigbe *et al.,* 2012; Ejenma *et al.,* 2014; Komolafe *et al.,* 2015; Nkwunonwo and Whitworth, 2019; Adetuji and Oleyele, 2018; Onwuemele, 2018; Bamidele and Badiora, 2019). The studies emphasized that flooding harms people's ability to maintain their way of life and carry on their social and economic activities. Flooding has caused the loss of thousands of lives and properties in previous decades.

According to available studies, poor planning and policy implementation, indiscriminate waste disposal practices, and human activities in floodplains are the leading causes of flooding in Nigeria (Ekpoh, 2015; Udoh, 2015; Evans *et al.,* 2017). Flooding has specifically affected the livelihood of several people, property values, and the sustainability of the ecosystem. Notably, flooding as a natural hazard has detrimental effects on the ecosystem, both from the perspective of eco-biodiversity and from an economic standpoint. These factors have led authors to predict increased damages and fatalities from flooding in the future (Hirabayashi *et al.,* 2013; Dottori *et al.,* 2018; Sayers *et al.,* 2018; Winsemius *et al.,* 2015; Wing *et al.,* 2018; Alfieri *et al.,* 2017). Therefore, it is evident that accurate flood prediction is required to prepare for and control the risk of flooding in the present and the future.

Hydrodynamic models have been crucial for identifying present and potential flood hazards (Sampson *et al.,* 2015; Teng *et al.,* 2017; Wing *et al.,* 2018). Many flood-related applications and tools have been used, such as flood risk mapping (Wing *et al.,* 2017), flood damage evaluation (Merz *et al.,* 2010), real-time flood forecasting (Barthelemy *et*

al., 2018), flood-related engineering (Gallegos *et al.,* 2009), and water resource planning (Hanington *et al.,* 2017). However, most parts of the world do not have the required height data or a dense network of hydrologic measurements to drive hydrodynamic models, so the model results are subject to substantial uncertainties. In other words, information about the topography (obtained from a digital elevation model) is a crucial input into a hydrodynamic model and majorly influences the length of anticipated floods (Horritt and Bates, 2002; Beven and Westerberg, 2011).

2.2   Modelling Flood Inundation

Knowing which locations are most vulnerable to flooding helps plan and manage flood risk. Hydrodynamic models are the most widely used tool for simulating and forecasting flood risk (Bates and De Roo, 2000; Neal *et al.,* 2012; Sampson *et al.,* 2015). It is possible to use hydrodynamic models with one, two, or even three spatial dimensions at different scales and levels of complexity. Hydrodynamic models provide the water depth, velocity, and area extent as time-dispersed outputs. To that purpose, this section will first introduce hydrodynamic models and various approaches to evaluating flooding. Then, it will explain the selection of the hydrodynamic model this thesis uses.

2.2.1 Hydrodynamic models

A hydrodynamic model is a computer program that applies the concepts of computational fluid dynamics to mimic water flow. A hydraulic model is another name, also widely used in the literature, for a hydrodynamic model. Coastal, pluvial, and riverine flooding are all simulated using hydrodynamic models. Water is routed along a river channel in fluvial applications, and it is subsequently routed onto the floodplain when the river channel overtops (Bates and De Roo, 2000; Sampson *et al.,* 2015).

In pluvial applications, runoff from point sources such as maintenance holes (Leandro *et al.,* 2009) or rainfall (Sampson *et al.,* 2015) drives water through primarily metropolitan regions. Water from storm surges and tidal oscillations is directed up river channels or overtops coastal defenses in coastal applications (Bates *et al.,* 2005). Flood risk managers and planners use the outputs of these hydrodynamic models, a map of the spatial extent of flood inundation along a time series, to guide planning and risk mitigation methods.

Topography and friction characteristics are crucial in regulating flood predictions because the balance between gravitational forcing and friction controls a flood wave (Bates, 2012). Hydrodynamic models can depict flow in one (1D), two (2D), or three (3D) dimensions, even though water flows in three dimensions. 1D models are the most minor complex, while 3D models are the most complex and computationally demanding. A flood risk manager has to weigh the trade-offs between knowledge, computational resources, and data availability. Bates and De Roo (2000) state that "the best model will be the simplest one that gives the information requested by the user yet reasonably fitting the given data," they effectively capture the decision regarding model complexity. Table 2.2 presents the types of hydrodynamic models.

Table 2.2: Types of hydrodynamic models

Type	Description	Computation Time	Examples of Software
0D	No physical laws included in simulations	Seconds	ArcGIS
1D	Solution of 1D Saint-Venant equations	Minutes	HEC-RAS; MIKE 11
1D+	1D plus flood storage cell for floodplain flow	Minutes to Hours	HEC-RAS; MIKE 11
1D/2D	1D for river channel flow and 2D for floodplain flow	Minutes to Hours	LISFLOOD-FP; MIKE FLOOD; SOBEK; TUFLOW
2D	Solution of 2D shallow water equation	Hours to Days	CaMa-Flood; LISFLOOD-FP; MIKE21 TELEMAC 2D
2D+	2D plus a solution for vertical velocities using continuity only	Days	TELEMAC 3D
3D	Solution of 3D Shallow Water Equations	Days	Delft 3D

Source: Pender and Neelz (2007)

2.2.2 Flow in hydrodynamic models

The Shallow Water Equations (SWEs) are a set of mathematical formulas used in hydrodynamic models to determine water movement. The shallow water equations (SWEs) are a set of equations derived from the Navier-Stokes equations, which in turn are derived from Newton's second law of motion. These formulas are used in many computational fluid dynamics applications, including aerodynamics and climate modelling. Flow is calculated using various SWEs based on whether the flow is constant (uniform) (Vila *et al.,* 2017).

2.2.2.1 *Steady flow in open channels*

To have a steady flow, an open channel's flow characteristics (such as water depth and velocity) must not change over time (Chaudhry, 2007). Similar in that for a given channel

length, uniform flow is defined by a consistent mean velocity and constant water depth along the flow direction (Brandimarte, 2012). The discharge, bed slope, and Manning's roughness must all remain consistent for a steady or uniform flow. One can use Manning's or Chezy's equations to represent steady and uniform flows. By multiplying the square roots of hydraulic radius R and slope S by a coefficient known as the Chezy coefficient C, which connects channel roughness and hydraulic radius, the Chezy equation determines the mean velocity (Junwei *et al.,* 2018) (Equation 2.1-2.2).

$$V = C\sqrt{RCS} \tag{2.1}$$

Similarly, Manning's equation relates mean velocity to Manning's roughness coefficient n, the hydraulic radius R, and the slope S

$$V = \frac{1}{n}R^{\frac{2}{3}}S^{\frac{1}{2}} \tag{2.2}$$

Discharge Q was calculated using these Equations 2.3 (Randa *et al.,* 2022) , which can be combined with the sectional area of a channel A.

$$Q = AV = A\frac{1}{n}R^{\frac{2}{3}}S^{\frac{1}{2}} \tag{2.3}$$

Hydrodynamic models typically depict flow with equations representing unsteady flow because the assumptions for these stable flow equations are frequently too simple due to the intricacy of nature.

2.2.2.2 *Unsteady flow in open channels*

Natural system flows are naturally unstable because the flow conditions change over time and are inconsistent in space due to variations in depth and velocity. The shallow water equations use continuity (mass conservation) and momentum to characterize the movement in unsteady flows (conservation of energy). The shallow water equations can be condensed into what is referred to as the Saint-Venant equations by making several assumptions, such as setting channel limits. The 1D Saint Venant equations, or a

simplified version of them, must be solved in order to depict movement in hydrodynamic models spatially in the most accessible possible manner (Horritt and Bates, 2002; Hunter *et al.,* 2008) (Equations 2.4–2.5).

$$\text{Continuity} = \frac{\delta A}{\delta x} + \frac{\delta Q}{\delta x} = 0 \tag{2.4}$$

$$\text{Momentum} = \frac{\delta Q}{\delta t} + \frac{\delta}{\delta x}\left[\frac{Q^2}{A}\right] + \frac{gA\delta(h+z)}{\delta x} + \frac{gn^2 Q^2}{R^{\frac{4}{3}}A} = 0 \tag{2.5}$$

where A is the cross-sectional area of the channel, x is the distance in the x Cartesian direction, and Q is the discharge. In the momentum equation, the additional terms are z (bed elevation), R (hydraulic radius), g (acceleration due to gravity), and n (Manning's coefficient of Friction). Also, $\frac{\delta Q}{\delta t}$ is acceleration; $\frac{\delta}{\delta x}\left[\frac{Q^2}{A}\right]$ is the advention; $\frac{gA\delta(h+z)}{\delta x}$ is the water slope and $\frac{gn^2 Q^2}{R^{\frac{4}{3}}A}$ is the frictional slope.

The four (4) categories of degrees of complexity are Kinematic, Diffusive, Inertial, and Fully Dynamic. The friction slope term is the single component of kinematic models, which are the most basic. The friction slope and water slope are two components of diffusive models. The local acceleration term, the water slope, and the friction slope are all present in inertial models. Ultimately, every term is present in a completely dynamic model. The Saint-Venant has an additional dimension in its 2D formulation, which makes it more computationally expensive to solve. Though this is frequently regarded as unduly complex, flows can be handled in three dimensions (Bates and De Roo, 2000). However, 3D models can be required in scenarios where spiral flows, vortices, and vertical turbulence are significant (such as levee breaches and dam failures). Although there is no analytical solution to these equations, numerical methods can be used to solve them.

2.2.2.3 *Types of numerical solvers*

Explicit and implicit techniques are used to solve SWEs based on how the equations are discretized in time and space (Popescu, 2012; Ali *et al.,* 2015; Nkwunonwo *et al.,* 2020). For explicit techniques, SWE is solved for every location within the model scope at a specific moment. Every time a time step is made after another, the SWE is again solved using the information from the prior time step.

Water can move through a cell in a time step, but if the time step is too big, instability may develop. On the other hand, if the time step is too tiny, the runtime for the model will be brief. The Courant Friedrichs Lewy equation (Nickolay *et al.,* 2018), which has the following formula Equation (2.6) as an expression, can be used to find an appropriate time step to prevent instabilities:

$$\frac{tc}{x} < 1 \tag{2.6}$$

where x is the spatial resolution, c is the inundation wave's velocity and t is the timestep. Flood researchers generally put the level just below 1, as setting it too close to 1 runs the risk of developing instabilities. The time step is correlated with the geographic precision and scales in the equation. In other words, as the spatial precision decreases, the flood wave can traverse a reduced distance before crossing two grid cells (causing instabilities), so the time step must decrease to ensure this does not happen. Therefore, the time step gets very tiny in hyper- and high-resolution models. Implicit techniques conduct computations using data from both the prior and current time steps. Implicit techniques do not need the equation because they are always steady. However, compared to explicit methods, implicit methods have a much higher calculation time per time step and are more challenging to step up (Popescu, 2012; Nkwunonwo *et al.,* 2020).

SWEs can be solved in time using implicit and explicit methods, but methods are required to define how they can be solved in space. Finite difference or finite volume techniques are two popular ways to explain how these problems are solved in space (Di Baldassarre, 2012a; Nkwunonwo and Whitworth, 2019). The finite volume method expands on this by giving each cell a volume and assigning its associated number to its center. Similar to finite volume difference in that the model area is divided into several elements, finite element has the disadvantage of computationally expensive mathematical techniques to generate solutions (Neelz and Pender, 2013).

2.2.3 Data requirements for hydrodynamic models

Hydrodynamic models explain how water moves through the terrain. Thus, information on the topography of the environment, the amount of water moving into and out of the model, and the Friction obstructing the flow of water are the three main types of data needed for hydrodynamic models. Some hydrodynamic models also need information on the canal shape and other elements, like infiltration. More data is needed for more complicated hydrodynamic models, as shown in Table 2.3 and 2.3a, which also lists the general data needs and model-specific results for each form of hydrodynamic model.

Therefore, a researcher of the flood may be constrained by data accessed even if a more complicated hydrodynamic is available. On the other hand, it might have a ton of data but need more expertise or computing power for modelling. Tables 2.3 and 2.3a show input and output data by type of hydrodynamic model.

Table 2.3: Input and output data by type of hydrodynamic model

Type	Input Data	Output
0D	DEM; Upstream water level; Downstream water level	Inundation extent and water depth
1D	Surveyed cross sections of channel and floodplain; Upstream discharge hydrographs; Downstream stage hydrographs	Water Depth and average velocity at each cross-section; Inundation extent by intersecting predicted water depths with DEM; Downstream outflow hydrograph
1D+	As 1D models	As 1D Models
1D/2D	DEM; Upstream discharge hydrographs; Downstream stage hydrographs	Inundation Extent; Water Depths; Downstream outflow hydrographs
2D	DEM; Upstream discharge hydrographs; Downstream stage hydrographs	Inundation Extent; Water Depths; Downstream outflow hydrographs; Depth averaged velocities at each computational node

(Source: Di Baldassarre, 2012a)

2.2.3.1 Topography

Topography is a crucial factor in estimating flood extent (Horritt and Bates, 2002). Digital Elevation Models (DEM) provide a gridded representation of topography and are frequently used in geoscience models. Previous studies show that the quality of the DEM affects the quality of flood estimates, with higher resolution DEMs typically giving more accurate flood estimates (Fewtrell *et al.,* 2011; Jarihani *et al.,* 2015; Savage *et al.,* 2016a; Savage *et al.,* 2016b). Topography is one of the significant factors influencing expected inundation spread (Bates and De Roo, 2000). Due to the flat topography of floodplains, even small topographic mistakes can have a significant impact on flood forecasts. A DEM, a gridded depiction of elevation, is the usual topographic input into a

hydrodynamic model. A DEM can be produced using remote sensing methods, field observations, or by digitizing paper topographic maps that already exist. Today, remote sensing methods are used to generate DEMs quickly, and Uysal *et al.* (2015) noted the advantages of surveying a large spatial region with fewer people at a reduced expense.

Remotely sensing techniques include photogrammetry (Coveney and Roberts, 2017), airborne and spaceborne interferometric synthetic aperture radar (InSAR), and light detection and ranging (LiDAR). Spaceborne DEMs (e.g., Shuttle Radar Topography Mission (SRTM) Farr *et al.* (2007)) are of intermediate scale, while photogrammetry and LiDAR-derived DEMs are of hyper-scale. Hyper-resolution DEMs are rarely available, with approximately 0.005% of the Earth's land area having free LiDAR data. Therefore, for the vast majority of the world (and assuming little to no funds are available to acquire a hyperscale DEM), the best source of topographic information is global DEMs (Table 2.4).

Table 2.4: Global DEM Products

	Dataset	Coverage	Acquisition Years	Sensor	Wavelength	Resolution (m)	Vertical Accuracy
Free Global DEMs	ALOS AW3D30	82°S - 82°N	2006-2011	Optical	0.52-0.77um	30	4.4m (RMSE)1
	ASTER GDEM	83°S - 83°N	2000-2011	Optical	0.78-0.86	30	17m (95% conf.)2
	GMTED2010	Entire Earth	Completed 2010	Derived from 11 sources of elevation information		250,500,1000	26m (RMSE)3
	SRTM	56°S - 60°N	2000	SAR C Band	5.66cm	30,90	6m (MAE)4
	TanDEM-X 90	Entire Earth	2010-2015	SAR X Band	3.1cm	30, 90	Unknown
Error Reduced Versions of SRTM	EarthEnv	60°S - 83°N	ASTER & SRTM			90	4.15m (RMSE)5
	NASADEM						
	MERIT	Entire Earth	AW3D30, SRTM & Viewfinder Panorama			90	5m (LE90)6
	No Name		Same as SRTM			90	5.9m (RMSE)7
	No Name		Same as SRTM			90	1m reduction in RMSE8
	Viewfinder Panorama	Entire Earth	ASTER, SRTM & Other Sources			90	Not Reported
Commercial Global DEMs	ALOS AW3D	82°S - 82°N	2006-2011	Optical	0.52-0.77um	5	2.7m (RMSE)9
	PlanetDEM 30 Plus	Entire Earth		Same as SRTM		30	Not reported
	NEXTMap World 10	Entire Earth		Not Reported		10	10m (LE95)10
	World 10 WorldDEM	Entire Earth	2010-2015	SAR X Band	3.1cm	12	<1.4m (RMSE)11

(Source: Yamazaki *et al.,* 2017; Wessel *et al.,* 2018; Zhao *et al.,* 2018)

Over the years, past studies have focused on other hydraulic factors, such as Friction, rather than topography's influence on flood forecasts; ambiguity in flood estimates from uncertain topography has largely been ignored (Wechsler, 2007). There are two factors at play here. First, there is a perceived need for more DEM products, which leads flood studies to use a single DEM as the best source of topographic data (even though this argument is losing strength, as shown by the number of DEM products listed in Table 2.4). The practice is widespread in data-scarce areas, where a single DEM, most frequently SRTM, is mandated by a supposed dearth of DEM products (Yan *et al.,* 2015).

As a result, studies rarely alter DEM results, while they occasionally alter other factors (such as Friction). Secondly, because the most significant source of topographic data for most sites is at 90 meters, there is little room to change the model resolution and still get usable results. Doing so would cause significant floodplain topography to be "lost" if the resolution is too low. Studies that do use multiple DEMs either resample DEMs to a low resolution to explore the effect of resampling strategies and scale (Fewtrell *et al.,* 2011; Savage *et al.,* 2016a; Komi *et al.,* 2017; Saksena and Merwade, 2015) or compare flood extents using different DEM products (Li and Wong, 2010; Jarihani *et al.,* 2015; Bhuyian and Kalyanapu, 2018).

For a summary of some studies that have examined the effect of topographic ambiguity on flood forecasts, see Tables 2.5, 2.5a, and 2.5b. The quality of flood forecasts typically improves as DEM resolution increases, but there is frequently a point where the improvement becomes insignificant and is not worth the additional processing power. Savage *et al.* (2016b), for instance, concluded that models with a resolution smaller than 50 m slightly improved the accuracy of flood predictions for a hydrodynamic model of the Imera basin, Sicily. Conversely, the same authors discovered that at resolutions lower

than 100 m, the accuracy of inundation forecasts significantly decreased. When modelling urban settings, higher-resolution DEMs are crucial so that structures can be included (Fewtrell *et al.,* 2011).

Table 2.5 Effect of DEM resolution and product on flood inundation predictions

Location	DEM	Resolutions	Model	Main Finding
River Severn	LiDAR	10,20,50,100,250,500,1000	LISFLOOD-FP	Below 100 m resolution model performance similar. For one model 250 m resolution best.
Tegucigalpa, Honduras	LiDAR	1.5,4.5,7.5,15	SOBEK	Large differences in predicted flood extent. Variations occur with DEM re-sampling techniques.
River Nene, UK	PROFILE Contour DEM, DGPS	30	LISFLOOD-FP	100 versions of DEM were simulated using Sequential Gaussian simulation. Uncertainty in predicted inundation extent greatest where elevation gradients were smallest.
Tadcaster, UK	LiDAR	4,8,16,32	JFLOW (Similar)	Small changes in resolution can have considerable effects. Inundation affected by lack of connectivity in low resolutions which in part can be compensated with by wetting and roughness parameters.
Santa Clara River near Castaic Junction	LiDAR, IfSAR, NED, SRTM	3,10,30,60,90	BreZo (2D)	LiDAR is the best source of terrain data, with its ability to detect bare earth important. NED DEMs flood zones 25% smaller than other DEMs. Little difference predicted in flood predictions between SRTM at 30 m and 90 m
Greenfield, Glasgow	LiDAR	2,4,8,16	LISFLOOD-FP	For urban areas representation of buildings important so finer resolution required. Response of Manning's friction coefficient to model resolution is non-stationary
Kansas River	LiDAR, NED, SRTM	2,10,30	Micro DEM	LiDAR and NED similar. SRTM noticeably different, with flood prediction fragmented. DEM source more important than resolution for flood extent
Alchester, UK	LiDAR (Terrestrial)	0.5,1,2,5	LISFLOOD-FP	Step change in performance between 2m and 5m grid resolution due to degradation of road network and camber representation

Source: (Li and Wong, 2010, Jarihani *et al.,* 2015, Bhuyian and Kalyanapu, 2018)

Table 2.5a Effect of DEM resolution and product on flood inundation predictions

Location	DEM	Resolutions	Model	Main Finding
Tewkesbury, UK	LiDAR	2,10,20,40	LISFLOOD-FP	Greatest loss of accuracy between 10m or 20m. Best accuracy at 2 m. Finest resolutions could simulate inundation dynamics best. Valley filling flow magnitudes similar all resolutions
River Wharfe, UK	LiDAR	4,8,16,32	Flood Map	Using subgrid information in coarse meshes improved model performance but improvement was only relatively small. High resolution features (walls, buildings) are important
Alchester, UK	LiDAR (Airborne & Terrestrial)	0.1,1	LISFLOOD-FP; ISIS-FAST	Bigger difference between DEM source than resolution
South Tibet	ASTER GDEM, SRTM, DEM from aerial photography	90	HEC-RAS	ASTER 2.2% smaller and SRTM 6.8% larger inundation extent compared to high resolution DEM
Alchester, UK	LiDAR (Terrestrial)	0.1,0.5,1	LISFLOOD-FP	Loss of hydraulic connectivity if micro terrain features not included
Thomson River, Australia	ASTER GDEM, SRTM	30,60,90,120,250,500,1000,2000	TUFLOW 2D	Model Performance noticeably worsened after 120-250 m. SRTM better than ASTER GDEM
6 Stream reaches in USA	LiDAR, NED, SRTM	1,3,6,30,90	HEC-RAS	Mean water surface elevation has a strong positive linear relationship with grid size. Predicted flood extent increases with coarser DEM resolutions. DEM source important, as LiDAR derived DEM at 30 m gave better prediction than NED at 30 m.
Kigali, Rwanda	ASTER GDEM, SRTM, DEM from aerial photography	5,10,20,30	SOBEK	DTM essential to represent urban flooding as ASTER and SRTM were found to be inadequate without correction. Models above 15m began to show significant inaccuracies
Imera Basin, Sicily	LiDAR	0,20,50,100,200,250,300,350,400,450,500	LISFLOOD-FP	Model performance deteriorates at resolutions coarser than 50m. Below 50 m little gain in performance. Doubling model resolution lengthens computation rime by order of magnitude

(Source: Li and Wong, 2010, Jarihani *et al.,* 2015, Bhuyian and Kalyanapu, 2018)

Table 2.5b Effect of DEM resolution and product on flood inundation predictions

Location	DEM	Resolutions	Model	Main Finding
Oti River, West Africa	SRTM	30,60,120,240,480,960	LISFLOOD-FP	Best index of fix at 480 m. Worst performance at 30 m. Local scale noise the likely reason for worse performance. Noise smoothed in coarsening DEM.
American River	ASTER, LiDAR, NED, SRTM	3,10,30,90	HEC-RAS	ASTER & SRTM overestimated inundated areas >4x compared to LiDAR and NED. Low hydraulic connectivity in ASTER. 30 m Resolution gave the lowest errors.
Kaoping River Taiwan	LiDAR-derived	1, 2, 5	HEC-RAS	LiDAR-derived DEMs provided higher accuracy compared to satellite-based DEMs.
Yangtze River China	ASTER GDEM, SRTM-DEM, TanDEM-X	30, 90, 12	HEC-RAS	Higher resolution DEMs improved the accuracy of flood inundation prediction.
Han River China	SRTM-DEM, ASTER GDEM	30, 90	HEC-RAS	The choice of DEM had a significant impact on the accuracy of flood inundation prediction.
Xiangxi River China	ALOS World 3D-30m, SRTM-DEM, ASTER GDEM	30, 90	MIKE21	Higher resolution DEMs provided better accuracy in flood inundation prediction and a positive correlation.
River Tachia Taiwan	LiDAR-derived, SRTM-DEM, ASTER GDEM	1, 5, 10	HEC-RAS	LiDAR-derived DEMs provided higher accuracy compared to satellite-based DEMs.
Songhua River China	SRTM-DEM, ALOS World 3D-30m	30, 90	HEC-RAS	Airborne LiDAR provided higher accuracy compared to satellite-based DEMs.

(Source: Li and Wong, 2010, Jarihani *et al.,* 2015, Bhuyian and Kalyanapu, 2018)

2.2.3.2 Boundary conditions

The upstream border condition (typically from a sensor) describes the amount of water entering a model, while the downstream boundary condition describes the amount of water leaving the model. Tidal gauges represent boundary conditions for maritime applications, while point sources (such as a ruptured water main) or direct rain on the grid are used for pluvial applications. Hydrographs characterize upstream boundary conditions in a fluvial environment (Grimaldi *et al.,* 2018). A water stage measurement can calculate the downstream border's water stage, flow, or slope, determining how much water exits the model area. Tarpanelli *et al.* (2013) say that the uncertainty in the downstream boundary conditions for river applications, which this thesis is mostly about, comes from the delay in the flow measurements and the water heights.

A rating curve is frequently used to predict discharge after measuring the water level. Deriving rating curves involves measuring the water level and release at the gauge site several times and then figuring out how they relate. The advantage of this method is that it is simple to determine the discharge by monitoring the water level. The assessment of the water level, the cross-sectional area of the waterway (especially if flow moves out of the bank), and the extension of the rating curve all introduce several errors for big floods (Domeneghetti *et al.,* 2013).

Even if a place is regularly gauged, it might not be in a flood event because extreme events can damage the gauging apparatus. In a thorough literature survey, McMillan *et al.* (2012) presented discharge errors of between 10 and 20% for medium to high flows and about 40% when flow moves out of the bank. Studies have, therefore, varied the upstream and downstream boundary conditions to evaluate the sensitivity of flood forecasts to boundary conditions (Domeneghetti *et al.,* 2013).

2.2.3.3 Friction

The surface-specific Manning's roughness coefficient usually defines the term friction term. A higher Manning's roughness number indicates that there is more resistance to the movement of water. Manning's values rely on the rough surface, changing depending on the land use type and the substance used for the canal bed. Chow (1959) presents examples of Manning's numbers. Channel and floodplain friction are generally described by two distinct factors, with floodplain friction typically having larger values than Manning's (Horritt *et al.,* 2007).

In reality, Manning's varies in time and space (Di Baldassarre, 2012b), so some attempts have been made to parameterize further by splitting channels into sections (Hall *et al.,* 2005), deriving distributed friction values from remote sensing (Wood *et al.,* 2016; Tarpanelli *et al.,* 2013), classifying by floodplain land-use type (Mtamba *et al.,* 2015; Afshari *et al.,* 2018), or floodplain characteristics (Manh *et al.,* 2014). Although Friction has a physical basis and can be measured, its values change over time and place and depend on size (Horritt *et al.,* 2007).

Therefore, friction parameters can be classified as effective parameters during calibration. They can be calibrated to compensate for other errors from boundary conditions, topography, and model structure (Di Baldassarre, 2012b). Some may quaff at such a practice as if the model cannot produce reality with physically plausible values, then it is evidence that the model is wrong (Cunge, 2003).

The friction values stated can accurately reflect the momentum losses, so this statement might be true if all data and model structures are error-free. However, given the intricacy of nature, this is different. A hydrodynamic model for flood forecasting should also be

understood to accurately anticipate water depths and flood spread rather than friction values (Di Baldassarre, 2012b).

Being an effective parameter makes it challenging to estimate the a priori distribution of values, so published values (such as those from Chow (1959)) should only be used as a general indication of the probable range (Horritt *et al.,* 2007). A hydrodynamic model successfully makes flood forecasts once calibrated adequately to a witnessed occurrence (Horritt and Bates, 2002). However, because different model parameter combinations frequently result in comparable degrees of success, there is often some degree of equality (Aronica *et al.,* 2016). Additionally, calibrating a model for a specific flood event may result in the hydrodynamic model being over-conditioned for the specific flood event if model performance is significantly better for a restricted range of parameters (Hunter *et al.,* 2007).

In other words, if a hydrodynamic model is limited to modelling a particular event for a small range of optimal parameter values, the optimal parameter set for a different possibility would be other, resulting in sub-optimal model performance. This situation frequently arises when insufficient empirical or "disinformative" data is used to test a model (Beven and Westerberg, 2011). In these situations, modelers may become overconfident in the model's abilities when, in fact, the model is only matching insufficient, inaccurate data. As a result, the model would be wrong in reality, which could be especially problematic if used to control flooding.

2.2.3.4 Channel geometry

For many rivers, there needs to be more information on channel geometry, as bathymetric surveys are very costly and time-consuming. However, 2D models require information

on river channel bathymetry. Therefore, approximations of channel geometry have to be made. It is expected to assume the channel shape is rectangular (Bates and De Roo (2000). Although this presumption is fair, there is enough variety in nature to show that it is too simplistic. Studies examining how sensitive models were to changing channel shapes concluded that calibrating depth and channel shape might be better than assuming a rectangular shape and adjusting Friction (Bate *et al.,* 2013).

A lack of understanding of river lengths leads to additional doubt. Although river widths can be physically calculated from satellite pictures, this method is time-consuming, labor-intensive, and only worthwhile for a short stretch. Using worldwide datasets like GWD-LR (Yamazaki *et al.,* 2017) or GRWL (Allen and Pavelsky, 2018) or automated tools like RivaMap, one option is to derive river widths automatically based on satellite optical pictures (Landsat or Sentinel) (Isikdogan *et al.,* 2017).

The hydrodynamic model's sensitivity to unknown width values has received little consideration up to this point. Since there is no accessible worldwide collection, channel bathymetry remains a critical uncertainty (Barthelemy *et al.,* 2018). Remote sensing has proven challenging for estimating channel bathymetry because signals from satellite instruments can only travel so far beneath the water's surface. As a result, numerous approaches have been suggested. Several places have used remote sensing measurements of river breadth and water surface height to determine bathymetry (Mersel *et al.,* 2013).

Benefits of the forthcoming Water and Ocean Topography (SWOT) mission, capturing river width and water top height. Additionally, using simulated SWOT results in a data assimilation strategy with hydrodynamic models has been effective (Yoon *et al.,* 2012). As an alternative, optical images and geostatistical methods have been used to determine river bathymetry (Adnan and Atkinson, 2012; Legleiter and Overstreet, 2012). When

accessible, bathymetry has been estimated using hyper-resolution LiDAR (Hilldale and Raff, 2008) or structure-from-motion photogrammetry (Javernick *et al.,* 2014). Recently, Lee *et al.* (2018) used velocity data from 2D SWE to estimate bathymetry using a principal component geostatistical method. Even when bathymetric readings are available, they are typically limited to specific points along a reach. As a result, GIS methods are used, and various river profiles are obtained by choosing an interpolation approach (Merwade *et al.,* 2008; Zhang *et al.,* 2016).

Numerous studies have examined how uncertain channel depth affects flood forecasts (Wong *et al.,* 2015; Grimaldi *et al.,* 2018; Cook and Merwade, 2009; Neal *et al.,* 2012). In essence, the channel geometry is immediately connected to the channel capacity and, consequently, to the bank discharge. "hydraulic geometry" refers to the connections between channel geometry and channel breadth, depth, velocity, and release (Leopold and Maddock, 1953).

2.2.4   0D models

0D models are built on the most basic hydraulic principles and do not consider any physical processes in water inundation (Pender and Neelz, 2007). They can be helpful for a comprehensive evaluation of flood extents and depths because they operate orders of magnitude faster than hydrodynamic models (Teng *et al.,* 2017).

One such example of a 0D model is the so-called "bathtub method," which intersects a DEM with water stage planes to define the region of a flood, with research using this method focusing on coastal flooding (Leon *et al.,* 2014; Van de Sande *et al.,* 2012). Alternatively, flood-prone regions can be found by computing the topographic index from DEMs (Samela *et al.,* 2015; Samela *et al.,* 2018; Manfreda *et al.,* 2014).

2.2.5 Empirical methods

Geologic or historical traces left behind from previous catastrophic floods are frequently examined. For instance, slack-water sediments (sand and silt) quickly build up during major floods as flood waters hold sediment. A sediment layer is left behind when flow speeds decrease and suspended silt is suddenly deposited. Sheffer *et al.* (2003) used geology to demonstrate past inundation in the Ardeche River. Deposits from floodplains can be geochemically analyzed to contribute to the record (Berner *et al.,* 2012).

Alternatively, historical records such as city accounts (Glaser and Stangl, 2001), etchings (Herget and Meurs, 2010), flood marks, legal documents (Kiss, 2009), narratives (Brázdil *et al*., 2006), newspapers (Guzzetti *et al.,* 1994), photographs (Smith *et al.,* 2015), songs (Brazdil *et al.,* 2006), taxation records (Brazdil *et al.,* 2014), and weather recordings (Brazdil *et al.,* 2006) have been used to construct historical flood records. The utility of this information to contemporary managers may be limited, even though it is intriguing, given how much society and river geometry have changed since the historical periods in which these floods were simulated. However, this knowledge helps educate people about the risk of flooding.

2.2.6 The best model

When discussing model selection, the famous quote of statistician George Box is often cited, where he noted, "All models are wrong, but some are useful." While true, models can be considered valid, partially beneficial, or utterly useless for their intended application (Burnham and Anderson, 2002). The key to successful modelling is selecting the model to help accomplish the job. Consequently, a researcher of flood should think of their primary responsibility for a flood model's implementation as offering an accurate forecast of storm inundation.

The principle of parsimony, as depicted by Box and Jenkins (1970), can be used to understand this tradeoff. According to the concept of parsimony, the bias tends to reduce, but the uncertainty rises as model complexity increases. Occam's razor, which proposes that no detail is essential, is another name for this concept. Therefore, the researcher of flood needs to create an appropriate model that trades off bias and ambiguity or, in other words, to create a sparse model. Unparsimonious models can range from models that are not complex enough to represent the dominant process to models that are unnecessarily complex in that by adding additional parameters, a model can fit almost any data, and thus such a model might make poor predictions as the parameterisation will be affected by the relatively high uncertainty (Di Baldassarre, 2012a).

The following are the four major questions that should be considered before selecting a suitable hydrodynamic model:

i.   What are the main processes controlling flood inundation?

ii.   What data is available?

iii.   What are the computational resources available?

iv.   When do the results need to be available?

The first question must evaluate the most probable water inundation processes. For example, a 1D model would be best adapted if requested to model a reach where inundation is regulated by topographic discontinuities (such as artificial embankments). Also, a 2D model is likely to be the most suitable if the area under review is a sizable floodplain where the terrain of the floodplain plays a significant role in controlling the extent of the flood (Di Baldassarre, 2012a).

Secondly, the researchers of flood need to take the facts into account that the quality of models depends on the data used to measure and validate (Beven and Westerberg, 2011).

Thirdly, the flood researchers need to think about the available processing tools. It is inappropriate to select a complicated model that will require an excessive amount of time or will flat-out not function on the computer in question. Equally essential is choosing a model that will be simple enough for the intended user if the project's findings are to be shared and used by those who are not hydrodynamic model specialists. Additionally, picking a model under constant development will allow for the most efficient use of improvements in algorithmic design.

A simpler model that permits numerous simulations is required if the model is meant to generate flood likelihood maps. Savage *et al.* (2016b) found that simulation time rises by an order of magnitude when the model resolution is halved, demonstrating the significant influence that model resolution can have on simulation time. The final factor to take into account is time. It is not advisable to select a model that will take weeks to months to run if the project has a deadline of six months, particularly considering the extra time required to set up the model. The applications' time restrictions should also be taken into account. For instance, quick models are needed for inundation predictions. Overall, no single model variety is the finest. The application, data accessible, computational tools, and time available all influence the model decision. The optimal model, however, will always be the most straightforward one that provides the necessary information while somewhat fitting the data (Bates and De Roo, 2000).

2.3   Considerations for Flood Modelling

Every model's performance is only as good as the data it utilizes for parameterization, calibration, and validation. Although it is evident that models of varying complexity have varied data needs, models should be chosen depending on the features of the current situation. In reality, this may limit the user's options for model selection. According to

Asselman *et al.* (2009), every hydraulic model needs the boundary condition, the beginning condition, topographical data, friction data, and hydraulic data for model validation.

Anuar (2018) stated that flood modelling requires hydraulic boundary determinations, geometric data, discharge data, roughness data, calibration, and validation. However, modelling floodplain flooding requires high-quality input data, including rainfall, a digital terrain model, land use, and calibration. A dense network of rain gauges and the weather radar should ideally provide rainfall data. Both sources are essential; the former is generally considered more accurate, while the latter typically has a higher spatial resolution, enabling advanced applications such as "nowcasting" (quick precipitation forecasting).

Hence, the modelling of floodplain flooding requires an accurate digital elevation model (DEM). It is a foundation for 2D or 3D modelling, developing surface flow routes and ponds, and identifying sub-catchments. On the other hand, the subsections from 2.3.1 to 2.3.2 discussed the function of topography and hydrology in flood modelling.

2.3.1   Hydrology and flood modelling

Rainfall patterns have an impact on flood behavior. Heavy rainfall is one of the most common causes of floods around the globe. Precipitation has previously been the cause of several floods (Shibata *et al.,* 2022). These types of flooding include river floods, flash floods, pluvial floods, and fluvial floods. Flooding has occurred in various areas due to rainfall ranging from severe to extremely heavy.

One of the primary causes of floods has also been infrastructure connected to hydrology. The dam is one of these infrastructures; it is an artificial water catchment system used for

agriculture, fisheries, water supply, or the generation of hydroelectric power (Adie *et al.,* 2012). Over the years, the dam has served its role as a piece of infrastructure, but it has also been a significant contributor to tragedies associated with flooding.

Authorities in Nigeria and neighboring nations like Cameroon frequently open the spillways of the dams and release massive volumes of water into settlements on the dams' floodplains to prevent dam failure during periods of heavy rain. Even with the substantial financial and material expenses that the dam authority incurs when such water releases occur and the dam's floodplain subsequently floods, these costs are occasionally underreported or not reported (Adesina *et al.,* 2021). Future climate change's hydrological effects will undoubtedly require significant revisions to current water management practices, with adjustments to dam operations playing a pivotal role.

2.3.2 Topography and flood modelling

The accuracy of hydraulic modelling and flood inundation mapping is significantly influenced by topography (Cook and Merwade, 2009). In order to use DEMs for hydraulic modelling, cross-sectional elevations, water surface elevations, and flood extents are used to identify the active channel. The key characteristics of a DEM that influence the outcomes of hydraulic and hydrologic modelling are resolution and accuracy (Vaze *et al.,* 2010).

A DEM's spatial resolution is defined as the amount of ground surface area that each cell covers. Hence, a higher-resolution DEM contains more cells per unit area than a low-resolution DEM, which more accurately depicts topography (ESRI, 2014a). The characteristics and qualities produced from DEMs can be impacted by resolution, which can also impact the models linked to them (Haile and Rientjes, 2005). The probability distribution of digital elevation values measured about the real value measures a DEM's

vertical correctness. The degree of linear inaccuracy in elevation is used to quantify it (ESRI, 2014b). The DEM's correctness directly influences the outcomes of the hydraulic modelling (Darnell *et al.,* 2008). Hence, water surface heights and flood extents are significantly influenced by DEM resolution and accuracy.

Topographic datasets are now crucial for flood mapping due to the development of GIS-based methods to derive channel cross-sections. Hydraulic modelling uses the cross-section elevations derived from topographic information to construct water surface elevations. The topography is subtracted from the estimated water surface acquired through hydraulic modelling to determine the flood extent (Sampson *et al.,* 2016). In subsections 2.3.2.1 through 2.3.2.3 that follow, another aspect of topography and flood modelling is presented in more detail.

2.3.2.1 Effects of low-resolution DEMs in flood modelling

Global, freely available DEMs have significant vertical errors made worse by complex topography and cannot resolve micro-topographic changes in relatively flat terrain (Gallien *et al.,* 2011; Chu and Lindenschmidt, 2017). In order to improve accuracy and reduce vegetation biases, several processing techniques and methods have been developed throughout the years (Robinson *et al.,* 2014; O'Loughlin *et al.,* 2016a; Yamazaki *et al.,* 2017). Even though these derived versions are regularly utilized, they frequently have vertical errors significantly higher than what is typically acceptable for many applications.

For example, present-day global DEMs cannot determine the specific topographic characteristics that regulate floods (Schumann *et al.,* 2019). In evaluating the impact of several large-scale DEMs on hydrologic runoff estimates, Kenward *et al.* (2000) emphasized that differing DEMs can result in a variance in runoff projections of over

10%. The US National Elevation Dataset (NED) data was among the online DEMs that Sanders (2007) investigated for their appropriateness for flood modelling.

The study found that DEMs based on InSAR technologies, particularly SRTM, suffer from radar noise and require prior processing, whereas NED DEMs are exceptionally clean and may overestimate inundation regions. Sanders (2007), however, stressed the importance of using SRTM as a worldwide source of topographical data for flood modelling, as demonstrated, for example, by Sampson *et al.* (2015). While utilizing a simplified scenario in their study, Li and Wong (2010) made an additional claim in related research that flooded regions from a flood simulation differed significantly across different DEM data sources.

Mukherjee *et al.* (2013) looked at the vertical accuracy of open-source DEMs (ASTER and SRTM) for hydrologic applications. They found slope and drainage network delineation could be better than their reference DEM. Walker and Willgoose (1999) showed that even very accurate DEMs from aerial photogrammetry can differ significantly from the ground truth. It is especially true for smaller catchments or applications where minor errors in the elevation can hurt small-scale applications.

The fact that the most widely used global DEMs currently need to be updated, such as the SRTM-DEM obtained in February 2000, is another severe constraint. While most national DEM programs that acquire photogrammetric or LiDAR DEMs repeat acquisition on a regular, multi-annual basis, the acquisition is rarely repeated. As a result, global DEMs will not account for any substantial geomorphological changes in topography or any human-made changes to the Earth's surface since data collection. Naturally, this can have profound implications when anticipating, say, flood occurrences in areas where it is known that earlier storms significantly changed the terrain in the area. The fact that there

are more people on the planet today than when SRTM was first obtained is even more astounding since every one of them played a role in changing the surface topography of our planet.

In this regard, James *et al.* (2013) pointed out that significant geomorphological changes can happen across decadal periods and even more quickly after catastrophic events and substantial human landscape transformation (e.g., mining). Even after extensive preprocessing to remove significant biases (due to vegetation and other physical structures) and reduce inherent vertical errors, globally available DEMs still frequently have inaccuracies that are orders of magnitude larger than the length scales of the simulated processes. On most river slopes, the residual vertical error in the SRTM DEM, for instance, is orders of magnitude greater than the size of the flood waves in such rivers (Bates *et al.,* 2013).

As a result, existing low-resolution global DEMs, like the SRTM-DEM, make it exceedingly difficult to represent floods and other intrinsically local phenomena effectively. Localized knowledge is crucial, which calls for more accurate terrain data with better resolution than what is currently offered at extensive coverage.

2.3.2.2 Needs for accurate DEM in modelling floodplain

Climate change has increased the flood hazard to coastal cities, which makes predicting future flood risk more unclear (Deng *et al.,* 2021; Lin *et al.,* 2016; Gu *et al.,* 2019; Fang *et al.,* 2020). Ultimately, the fear of floods in all its variations causes financial losses and human fatalities. Thus, it is essential to identify flood hazards and provide accurate catastrophe forecasts and emergency response by accurately estimating flood inundations in urban regions of coastal cities (Yang *et al.,* 2020; Yin *et al.,* 2020). Flood inundation mapping is crucial for identifying possible impact regions and determining inundation

depths to assess the severity of flood risks and improve understanding. Hydrodynamic models have been widely employed for flood simulations due to improvements in computer performance as well as the simplicity and refinement of the methods (Yu and Lane, 2006). The significant topographic input data, DEMs, are an essential component in regulating hydrodynamic model correctness (Kenward *et al.,* 2000; Cobby *et al.,* 2001).

Flood mapping and modelling have both made extensive use of open-access DEM products (Pedrozo-Acuna *et al.,* 2015). Unfortunately, the capacity to predict flooding regions and pertinent dangers is considerably constrained by the open-access DEMs' generally poor resolution and accuracy (Sampson *et al.,* 2016). It has been shown that poor DEM data quality can cause significant biases in flood prediction (Hawker *et al.,* 2018). The spatial resolution and vertical inaccuracy of DEMs have the most significant impacts on this. Poor spatial resolution impairs the accuracy of the flood simulation and the identification of surface characteristics (Vaze *et al.,* 2010; Saksena and Merwade, 2015). Elevation inaccuracies in the vertical direction may impact the accuracy of the terrain simulation and, consequently, the flooding simulation (Mukherjee *et al.,* 2013; Talchabhadel *et al.,* 2021). Accurate DEMs are essential for exact flood modelling and management (Coveney and Fotheringham, 2011; Adesina *et al.,* 2021).

2.3.2.3 Significance of DEM resolution

The resolution of a digital elevation model (DEM) is one of the key factors influencing the outcomes of hydraulic modelling. Understanding the significance of DEM resolution on flood mapping is crucial for improving the forecast accuracy of DEMs. Several researchers who examined how changing DEM resolution affected hydraulic modelling concluded that DEM resolution was crucial in forecasting hydraulic outputs. Hydraulic controls, such as embankments, have a considerable impact on the accuracy of flood

extents, according to one of the earliest studies by Werner (2001), which examined the impact of grid size on the accuracy of projected flood regions. By utilising a low-resolution DEM, local altitudes around the hydraulic controls averaged out, but using higher-resolution DEMs dramatically lengthened the computation time.

A DEM resolution of 5 m had a considerable rise in the inundation extent and depths. It looked extraordinarily enormous, according to Kurniyaningrum *et al.* (2019) study on the sensitivity of flow depth inundation based on micro-scale topography. Together with the excess in flood extent, the combined effect of flood depth and inundation area grew considerably. They claimed that a LIDAR DEM with a resolution of 1 m to 5 m impacted the propagation of flood waves in a channel and the adjacent floodplain, changing the topography's geometrical characteristics and slowing or accelerating water flow.

Flood modelling and mapping frequently employ DEM (Pedrozo-Acuna *et al.,* 2015). Nevertheless, because of the open-access DEMs' generally poor resolution and accuracy, the ability to anticipate inundation locations and associated threats is severely limited (Sampson *et al.,* 2016). Significant biases in flood prediction have been linked to poor DEM data quality (Hawker *et al.,* 2018; Rahmati *et al.,* 2020). The major influences on this are the vertical accuracy and spatial resolution of DEMs. The precision of the flood simulation and the identification of surface properties need to be improved by low spatial resolution (Vaze *et al.,* 2010; Saksena and Merwade, 2015). Elevation errors in the vertical direction may influence the accuracy of the terrain simulation and, consequently, the flood simulation (Mukherjee *et al.,* 2013; Talchabhadel *et al.,* 2021). It has been established that accurate DEMs are necessary for highly accurate flood modelling and control (Cook and Merwade, 2009; Coveney and Fotheringham, 2011).

This issue cannot be adequately addressed since the low-resolution DEMs make it challenging to determine channel shape, the signal attenuation of water bodies, or radar reflections. As there is just one set of elevation data over a broader region, DEMs with larger grid sizes contain less specific information. Higher resolution DEMs or smaller grid sizes show the heights of smaller regions and are thus more suited to displaying finer topographic features. The DEM's flood regions and depths were found to grow as the grid size was raised. Low-resolution DEMs will always lead to overestimating flood depth and extent, regardless of the kind of flood. The reverse tendency for surface water floods, however, has been demonstrated by other investigations (Mukherjee *et al.,* 2013; Hawker *et al.,* 2018; Ogania *et al.,* 2019; Mohamed and Ali, 2019; Talchabhadel *et al.,* 2021; Kepeng *et al.,* 2021).

2.4   Role of Remote Sensing in Flood Modelling

Remote sensing technologies, such as LiDAR, aerial imagery, and satellite-based sensors, offer valuable data sources for generating Digital Elevation Models (DEMs) used in flood modelling. These technologies provide detailed elevation information with varying resolutions, capturing topographic characteristics for accurate flood simulations (Smith *et al.,* 2019). Remote sensing DEMs provide high-resolution data, crucial for representing fine-scale elevation variations that significantly influence flood modelling, particularly in urban areas (Sanders *et al.,* 2020). These small topographic features have a significant impact on flood propagation. The use of remote sensing data allows for the accurate representation of these variations, improving the reliability of flood models.

Remote sensing data enables large-scale coverage, facilitating flood modelling at regional or national scales and supporting flood risk assessments across diverse landscapes (Smith *et al.,* 2019). This extensive coverage is essential for understanding flood dynamics in

different geographical areas and developing effective flood management strategies. Remote sensing data is easily accessible through various platforms and archives, ensuring seamless DEM integration into flood modelling workflows. This accessibility enhances the efficiency of flood risk assessments by providing researchers and practitioners with readily available data for their analyses (Talchabhadel *et al.,* 2021).

Remote sensing DEMs allow researchers to monitor changes in flood-prone areas over time. By analysing the temporal changes captured by remote sensing data, researchers can observe modifications in channel morphology, urban development, or natural landscape alterations, providing valuable insights for flood modelling and management (Smith *et al.,* 2019). Remote sensing technologies play a crucial role in flood prediction and disaster management. Images extracted from satellite and aerial photographs are analyzed using image processing algorithms to forecast the possibility of flooding in specific locations (Syifa *et al.,* 2019). Flood risk maps can be created using remote sensing data, including tools like interferometry synthetic aperture radar (InSAR) technology, space-based imaging devices, and satellites, which provide high-quality pictures of land and water reservoirs even in poor weather and low-light situations (Anusha and Bharathi, 2019).

Several research studies have demonstrated the effectiveness of remote sensing DEMs in flood modelling. Smith *et al.* (2019) utilized high-resolution LiDAR DEMs to accurately simulate flood extents and depths in a riverine system, improving flood hazard mapping. Tariq *et al.* (2021) compared satellite-based DEMs and aerial imagery-derived DEMs for urban flood modelling, emphasising the importance of high-resolution data in capturing urban drainage networks and flood-prone areas. Li *et al.* (2017) integrated LiDAR-based DEMs and satellite imagery in flood modelling to simulate flash flood events in a

mountainous region, showcasing the ability of remote sensing DEMs to capture complex terrain features and rapid elevation changes.

Remote sensing DEMs have revolutionised flood modelling by providing accurate and high-resolution elevation data. Integrating remote sensing technologies, such as LiDAR, aerial imagery, and satellite sensors, has significantly improved our ability to generate precise flood models, assess flood risk, and develop effective flood management strategies. The advancements in remote sensing technology, along with the accessibility of spatial data archives, continue to enhance our understanding of flood dynamics and improve flood risk assessment worldwide.

2.5   Open Source DEMs

Spaceborne global DEMs are the finest topographic data source for most of the Earth because freely accessible, high-accuracy aerial hyper-scale DEMs (10 m horizontal resolution) are only available for a tiny part of the Earth's land area (0.005%). There are several publicly and privately accessible global DEM goods. The Shuttle Radar Topography Mission (SRTM) continues to be the most commonly used worldwide DEM product.

In late 2015, one arc-second (about 30 m) release followed the initial release of a three arc-second (about 90 m) near-global DEM. There are numerous SRTM variants, including the initial SRTM V1 that was not void-filled, the SRTM V2 and V3 that were void-filled, and the CGIAR-CSI version (Jarvis *et al.,* 2008).

A reprocessed version of the initial SRTM dataset called NASADEM (Crippen *et al.,* 2016) is scheduled for publication soon. Other freely available global DEMs include the Advanced Spaceborne Thermal Emission Radiometer (ASTER) (Abrams, 2000) with the

global product at 90 m and spanning to 83°S and 83°N, the Advanced Land Observing Satellite (ALOS AW3D30) (Tadono *et al.,* 2016) at 30 m, and the Global Multi-resolution Terrain Elevation Data 2010 at 250 m resolution (Danielson and Gesch, 2011).

Similar to publicly available DEMs, privately available DEMs (like Nextmap World10TM, World30TM, and Airbus WorldDEMTM) are also accessible but constrained by their limited use, prohibitive prices, and the absence of independent validation studies comparing them to other DEMs and ground observations. With all these considered, the SRTM dataset is generally still preferred, mainly the CGIAR-CSI Version 4 (Jarvis *et al.,* 2008), due to ease of access, more excellent feature resolution, a reduced number of artifacts, lower noise, and better vertical accuracy than other global DEM products and older versions of SRTM (Jing *et al.,* 2014; Rexer and Hirt, 2014; Jarihani *et al.,* 2015; Sampson *et al.,* 2016; Hu *et al.,* 2017).

So, the SRTM and its offshoots are still an essential source of topographic data for many hazard and risk assessment models. These happen in places with little data, and high-resolution topographic data like LIDAR (light detection and ranging) is unavailable or cannot be obtained. SRTM remains the best choice for elevation data for a large portion of the Earth right now and for the foreseeable future, despite demands for a coordinated effort to create a free, accurate global DEM (Schumann *et al.,* 2019).

An extensive global study by Rodriguez *et al.* (2006) provided the most thorough characterization of errors in the SRTM dataset. Using nearly 9.4 million Kinematic Global Positioning System (KGPS) samples gathered along roads in six countries, Rodriguez *et al.* (2006) discovered that 90% of the errors were less than 5 m, well within the mission's precision standards of an absolute height error of 16 m (Rabus *et al.,* 2003). SRTM absolute errors have also been evaluated in other, more confined investigations

with a predominant vertical error emphasis. Although reporting vertical accuracy as a singular quantity, such as root mean square error (RMSE), has its benefits in terms of speed of calculation and ease of reporting, it does not accurately depict the heterogeneity of the error. It may initially give the impression that the error across the DEM is consistent.

2.6   Topographic Accuracy of DEMs and Applications

DEMs are essential geospatial datasets used in various applications, such as topographic analysis, hydrological modelling, and landform characterization. The availability of open-source data and tools has led to an increase in the number of open-source DEMs accessible for different regions worldwide. This literature review aims to examine the topographic accuracy of open-source DEMs and explore their applications, emphasising their strengths, limitations, and potential for geospatial analysis.

Open-source global DEMs, like SRTM and ASTER, suffer from vertical errors, particularly in complex topography and flat terrain (Gallien *et al.,* 2011; Chu and Lindenschmidt, 2017). These errors can be significant and might affect their utility in specific applications. Various processing algorithms and merging approaches with other elevation datasets have been proposed to improve accuracy and address vegetation biases (Robinson *et al.,* 2014; O'Loughlin *et al.,* 2016b; Yamazaki *et al.,* 2017; Yue *et al.,* 2017). However, despite these efforts, certain limitations persist, especially in areas with complex terrain or dense vegetation. Different ways have been used to check the topographic accuracy of open source DEMs, such as field surveys, comparisons with reference datasets like LiDAR, statistical metrics (like root mean square error and vertical accuracy), and visual inspection. Quality assessment tools, such as the National Elevation Dataset Validation Tool (NEDVT), have also been used to evaluate DEM accuracy.

Mukherjee *et al.* (2013) assessed the vertical accuracy of open-source DEMs, including ASTER, SRTM, and GTOPO30, using the Root Mean Square Error (RMSE). They found that topographic accuracy was violated regarding slope and drainage network delineation. Dawod and Ascoura (2021) validated four open-source Global Digital Elevation Models (GDEMs) using various topographic profiles. The study reported accuracy values for different regions, highlighting limitations and suitability for specific map scales and contour intervals.

Open-source DEMs have found wide applications in various geospatial analysis and modelling tasks, such as hydrological modelling, flood mapping, slope stability analysis, land cover classification, and terrain visualization. The accessibility of open-source DEMs has facilitated research and decision-making processes related to land management, environmental assessment, and disaster risk reduction. Despite their advantages, open-source DEMs face limitations related to data quality, resolution, and horizontal accuracy, affecting the reliability of derived analyses and interpretations. Additionally, data gaps, inconsistencies, and limited coverage in certain regions may restrict their applicability for critical applications. Continued research and development efforts are necessary to improve the topographic accuracy of open-source DEMs. This includes advancements in data collection techniques and algorithms for data processing and interpolation. Collaborative approaches involving public-private partnerships have been proposed to develop high-accuracy global DEMs to support water management and disaster assessment.

Open-source DEMs offer valuable resources for geospatial analysis, and their accuracy varies based on several factors. Understanding their strengths and limitations allows researchers and practitioners to effectively leverage these datasets in diverse applications,

supporting sustainable land management, environmental assessment, and natural hazard mitigation. As technology and data availability advance, open-source DEMs will play an increasingly important role in geospatial analysis.

2.7   Generation of DEMs from UAV Data

The benefit of using UAVs over conventional data collection techniques is their speedy delivery of high-resolution pictures for a temporal event (the degree of flooding at a particular flood stage) (Popescu *et al.,* 2017). UAVs are adaptable and can be flown with various sensors that can be set up to detect a range of possible data requirements, particularly for locations with complicated urban landscapes and inaccessible areas owing to dangerous surroundings.

For a localized photogrammetry project, UAVs may also be operated cheaper than human aircraft. They can even be used to return to the exact location repeatedly to track changes over time, such as those caused by flooding. UAVs are, therefore, quickly deployed and offer on-demand flood mapping photogrammetry platforms that are cost-effective. Such maps' dependability and correctness depend on the quality of the topographic data and digital elevation model (DEM) (Kulkarni *et al.,* 2014; Leitao *et al.,* 2016).

Flood-risk analysis for hazard and vulnerability models depends on accurate topographic data and DEM. According to research by Zazo *et al.* (2015), even a small DEM error, particularly in a flood-prone area, can significantly alter the flood-risk map for that region.

2.8   Applications of UAV-Based DEMs

Several researchers have developed and evaluated the effectiveness of UAV-based DEM for various applications (Uysal *et al.,* 2015; Krsak *et al.,* 2016; Koci *et al.,* 2017). UAV photogrammetry was examined for applications in 3D mapping and topographic monitoring of coastal regions (Goncalves and Henriques, 2015; Kung *et al.,* 2011).

Serban *et al.* (2016) looked at how UAV technology and Leica Multi-Station GNSS surveying could be used together to make a high-quality DEM of the significant and minor riverbeds in the Somesul Mic basin and collect specific hydraulic parameters to study ways to manage flood risk.

A DEM with a vertical RMSE of 11.9 cm in submerged regions and 8.8 cm in dry areas was created, along with a 5 cm orthomosaic. The DEM's precision allowed for the initialization and operation of the River2D two-dimensional hydrodynamic model. In terms of weighted useable area, the model results, such as the depth and speed distributions, were combined with the mapped physical habitat characteristics to determine how much habitat is available.

Ajayi *et al.* (2017) investigated the accuracy of GNSS receivers installed on a UAV platform for DEM synthesis to estimate flooding risk, create complete relief measures right away after flooding, and provide damage assessment in both geographical and temporal dimensions. Accurate monitoring and mapping of the DEM and flood extent are essential.

Esmaeel *et al.* (2022) investigated the effect of unmanned aerial vehicle (UAV) DEM resolutions on flood characteristics, including the inundation area, mean flow depth, and mean flow velocity. Results showed that when UAV DEM resolution decreased from 1 m to 30 m, inundation area and mean flow depth increased by 17.0% and 10.2%, respectively, while mean flow velocity decreased by 16.8% ($R^2 = 0.94$). Validation of the hydraulic modelling using the modified normalized difference water index showed that the HEC-RAS 2D model, in conjunction with the UAV DEM, simulates the flood with 92% accuracy. The results could be a guideline for selecting global DEMs for hydraulic simulations.

UAVs have already proven to be highly effective for mapping applications, in addition to having a significant potential for producing rapid and precise on-demand DEMs in flood-assessment applications. The creation of the DEM using UAV data from a flood-prone section of the Shiroro Dam floodplain was investigated in this study. Leitao and de Sousa (2018) used a drone-based DEM for urban surface fog modelling to be potentially connected to a drainage model of a Swiss town; Erban and Gorelick (2016) investigated the use of UAV technology coupled with Leica MultiStation to generate a high-quality DEM of the flood-prone area of the Somessul Mic Basin, Transylvania.

Hashemi-Beni *et al.* (2018) looked into the quality of UAV-based DEM for spatial flood assessment mapping and figuring out how big a flood event was in Princeville, North Carolina. They did this to show how difficult it can be to make DEMs on demand during a flood. Schumann *et al.* (2019) demonstrated that mapping terrain using a UAV has a trivial error compared to a LiDAR-generated terrain model and can thus extract cross-sections with high accuracy.

Lee *et al.* (2019) used UAVs over the river floodplain to extract detailed topography, combining virtual Natural Hazards reference stations with total station survey equipment to reduce a DEM to an accurate DTM. These researchers have shown promising results for an extensive application of UAV photogrammetry in hydraulic modelling, confirming the advantages of drone-based remote sensing with a drastic cut in risks, costs, and execution time while delivering products of satisfactory quality for the intended use.

2.9   Accuracy Assessment of Flood Modelling

Flood modelling is crucial in assessing and managing flood risks in various regions worldwide. Accurate flood modelling is essential for effective decision-making, emergency response planning, and infrastructure development. A literature review explored and evaluated the accuracy assessment methods employed in flood modelling studies, highlighting the importance of reliable models for enhancing flood prediction and management.

Various accuracy assessment methods have been employed to evaluate the performance of flood models. These methods include statistical metrics such as root mean square error (RMSE) (Hladik and Alber, 2012), mean absolute error (MAE) (Hawker *et al.,* 2019), root mean square error (RMSE), and correlation coefficient. Jakovljevic *et al.* (2019) used spatial analysis techniques like overlay analysis and validation against observed flood events. Additionally, remote sensing data and geographic information systems (GIS) have been used to validate flood extents and compare them with modeled results. For example, Hladik and Alber (2012) conducted an accuracy assessment of a LIDAR-derived salt marsh digital elevation model (DEM) by comparing it with GPS data collected using the Real-Time Kinematic (RTK) mode. The study found that the vertical error of the DEM ranged from 0.25 m to 0.3 mm when compared to the RTK results. They also developed a correction factor model to reduce the mean DEM error and the root mean square error.

Similarly, Hawker *et al.* (2019) assessed the accuracy of the TanDEM-X 90 Digital Elevation Model for a selected floodplain site. They compared the accuracy of TanDEM-X with the widely used Shuttle Radar Topography Mission (SRTM) and a modified version of SRTM called Multi-Error-Removed-Improved-Terrain (MERIT). The study found that TanDEM-X and MERIT showed improved vertical accuracy compared to

SRTM, with TanDEM-X being more accurate in all land cover categories and MERIT demonstrating more accuracy in tree-covered areas.

The study suggests that the combination of TanDEM-X and MERIT has the potential for floodplain assessment. Jakovljevic *et al.* (2019) performed an accuracy assessment of deep learning-based classification of LIDAR and UAV point cloud data for Digital Terrain Model (DTM) creation and flood risk mapping. The study used pixel-by-pixel accuracy assessment and visual inspection to examine the accuracy of the DEM generated by LIDAR and UAV.

Several factors influence the accuracy of flood modelling, including data quality, model complexity, topographic characteristics, and calibration and validation techniques. The availability and accuracy of input data, such as digital elevation models (DEMs), rainfall data, and hydraulic parameters, significantly impact the reliability of flood models. Furthermore, selecting appropriate modelling techniques, parameter calibration, and validation against observed data are critical for achieving accurate flood predictions.

In salt marshes, Hladik and Alber (2012) noted that poor laser penetration in dense vegetation, sensor resolution, and instrument errors all limit accuracy. Hawker *et al.* (2019) also highlighted the influence of terrain characteristics on DEM accuracy, with MERIT exhibiting more accuracy in tree-covered regions and TanDEM-X being useful in nearly all land cover types. Jakovljevic *et al.* (2019) wrote about how LIDAR and UAV can be used to make DEMs based on the characteristics of the study area. LIDAR is good for areas with water, and UAV is suitable for hills.

Despite advancements in flood modelling techniques, several challenges and limitations persist. Inaccurate or incomplete input data, uncertainty in modelling assumptions, and

limitations in computational resources can affect model accuracy. Hladik and Alber (2012) emphasized the need for unique data acquisition methods based on the nature of the terrain, as observed in their study of a salt marsh. Additionally, the dynamic nature of floods, such as rapid changes in flood patterns and extreme events, poses challenges in accurately capturing their behavior and magnitude. Improving the accuracy of assessment methods and addressing the identified limitations can enhance the reliability of flood models. Integrating real-time data, advanced remote sensing techniques and ensemble modelling approaches can lead to more accurate flood predictions. Additionally, incorporating uncertainties and sensitivity analysis into flood models can provide valuable insights into the reliability of predictions.

In conclusion, the accurate assessment of flood modelling is vital for reliable flood prediction, risk assessment, and effective decision-making. This literature review highlighted the various methods used to assess the accuracy of flood models, the factors influencing accuracy, and the challenges associated with flood modelling. Continued research and advancements in data collection, modelling techniques, and accuracy assessment methods will contribute to improved flood modelling capabilities and enhance flood risk management strategies.

2.10   Findings from the Literature Review

This section presents a summary of the findings of the literature review:

i.   Many studies modelled flooding as a function of topographic height, ignoring hydrological and hydraulic factors as key parameters (Mayomi *et al.,* 2014; Usman and Ifabiyi, 2012; Olukanmi and Salami, 2012).

ii.   Many studies have used low-resolution DEMs that led to the loss of important floodplain topography (Savage *et al.,* 2016a; Ogania *et al.,* 2019).

iii.   Most researchers used hydrodynamic models subject to substantial uncertainties due to a lack of high-resolution data and hydrologic measurements (Schumann *et al.,* 2019; Nkwunonwo *et al.,* 2020).

iv.   Most researchers have used global DEMs, such as the National Elevation Dataset and SRTM DEMs, that overestimate or underestimate flood models (Sanders *et al.,* 2020).

v.   Most researchers used historical records to construct flood records, but their usefulness to modern planners needs to be improved as society and river geometry change (Corringham and Cayan, 2019).

vi.   The low-resolution DEMs led to an over-prediction of flood depth and extent, regardless of the kind of flood (Saksena and Merwade, 2015).

Hence, most researchers who have worked on flood modelling have only used low-spatial-resolution DEMs as their input parameters. It has resulted in inaccurate flood models that often need to depict the extent of flood damage in the event of flood mishaps due to the inappropriate spatial resolution of the input DEM. Thus, the study aims to close this gap by demonstrating how DEMs with a specific spatial resolution from different data sources affect flood simulation.

CHAPTER THREE

3.0   MATERIALS AND METHODS

3.1   Materials

Materials in this study refer to the various data types used to achieve the research's goal. The instruments, software, and hardware used to gather and process the collected data. Although, some of the data used in the study were obtained directly in the field (primary data) and from secondary sources. An analysis validates the authenticity of all secondary data before use in this study. The details of the materials and data used are in Table 3.1, and the materials are in Section 3.3. Figure 3.1 shows a workflow view of the research methods adopted in this study.

Table 3.1: Details of the materials and data used for the study

Primary Data	Source	Instrument	Processing software	Spatial resolution	Data acquisition date	Accuracy
UAV-Derived DEM	Field mission	UAV Trimble UX5	Trimble Business Center Photogrammetry Module application (version 3.30)	1 m	2019	0.1 m
River channel bathymetry	Field mission	Dual-frequency GPS receiver and Hi-Target DH Light Echo Sounder	ArcGIS	-	2019	-

Secondary data	Source	Instrument	Processing software	Spatial resolution	Date of data acquisition	Accuracy
InSAR 10 m DEM	https://scihub.copernicus.eu/dhus/#/home.	N/A	SeNtinel Applications Platform (SNAP) version 8.0	10 m	2021	1 m
SRTM 30 m DEM	http://earthexplorer.usgs.gov	N/A	ArcGIS	30 m	2000	3 - 4 m
Settlements flooded	NSEMA	N/A	N/A	-	2021	-
Settlements data for the study area	Niger State Geographical Information System (NIGIS)	N/A	N/A	-	2021	-
Water level, rainfall, inflow, temperature and outflow	Shiroro Dam Authorities (hydrological data)	N/A	N/A	- / -	2021 / 2020	- / -

PHASE 1	PHASE 2	PHASE 3	PHASE 4

| Acquisition of hydrological data (such as rainfall, inflow, reservoir water level, temperature and outflow) | Generation of high-resolution 1 m UAV DEM | Generation of high-resolution 10 m InSAR DEM | Download low-resolution 30 m SRTM DEM |

| Preparation of hydrological data | Assess the quality of floods modelled using UAV data | Assess the quality of flood modelled using InSAR data | Assess the quality of flood modelled using SRTM data |

| Correlation of hydrological data | Shallow Water Equation (Simulation of flood events and river flows) | Shallow Water Equation (Simulation of flood events and river flows) | Shallow Water Equation (Simulation of flood events and river flows) |

| Inputting outflow data |

| PHASE 5 |

| Discharge | Discharge | Discharge |

| Flow velocity | Flow velocity | Flow velocity |

| Flow potential | Flow potential | Flow potential |

| PHASE 6 | VALIDATION |

Figure 3.1: The workflow view of the research procedure

3.2   Conceptual Framework (Choice of Data and Hydrodynamic Models)

A hydraulic model must meet the following requirements to satisfy the standards of good practice (Beven *et al.,* 2018).

i.   Computationally efficient enough to run multiple simulations at a regional scale at a high resolution

ii.   Few data requirements (i.e., suitable for a data-sparse location)

iii.   Ability to represent flood inundation over a large floodplain

The Shiroro Dam floodplain in Niger State, Nigeria, is a very sizable area. A trade-off is needed between model complexity and resolution so the model can capture the correct processes but can, in turn, be run multiple times. A 2D model is best suited to replicate flow over the complicated topography of the floodplain as storm inundation expands over topography. A 1D model is unsuitable because it is inadequate to capture the intricate terrain of the floodplain.

In order to study the impacts of DEM resolution, a hydrodynamic model needs to be able to operate at various levels. As a result, this study chose to use ArcScene in ArcGIS 10.4 to carry out the hydrodynamic model simulation. Three DEM resolutions were examined to determine the effect of DEM resolution on the resulting flood models. The investigated DEMs are UAV-derived 1 m DEM, InSAR 10 m DEM, and SRTM 30 m DEM.

Arc GIS 10.4 software was used to perform the 2D storm inundation simulation. Waterway and surface flooding are brought on by rain using ArcScene in ArcGIS 10.4. Before running a flood simulation in ArcScene, the river outflow and flow rate were calculated in MATLAB using the standard shallow water equation (SWE) in Equation (3.1). The preference for SWE

is because of its capacity to model unsteady flow, unlike the other flow modelling equations, which are better suited for modelling steady flow. However, the reality of surface runoff and flood modelling is that they could be more stable flows. Equations 3.1–3.5 (Vila *et al.,* 2017; Adesina *et al.,* 2021) present a mathematical description of the conceptual framework for flood modelling in light of the variable spatial resolution of the input topographic data. SWE is of the form (Vila *et al.,* 2017):

$$\frac{\delta Q}{\delta t} + \frac{\partial}{\partial x}\left(\frac{Q^2}{A}\right) = -gAS_f + gAS_0 - gA\frac{\partial h_o}{\partial x} \tag{3.1}$$

where

Q = discharge

A = cross-sectional area

$\frac{\delta Q}{\delta t}$ = rate of discharge with respect to time

$\frac{\partial}{\partial x}\left(\frac{Q^2}{A}\right)$ = rate of discharge with respect to cross-sectional area

g = acceleration due to gravity

S_f = frictional slope

S_o = reference slope

h_0 = is a typical length characteristic of the height of the flow

$\frac{\partial h_o}{\partial x}$ = channel bed-topography

Q can be computed as:

$$Q = \frac{A}{n} * R^{\frac{2}{3}} * S^{\frac{1}{2}} \tag{3.2}$$

where

R = Hydraulic radius

n = Manning coefficient of roughness

A = Cross-sectional area

S = Channel slope in the direction of flow,

$\frac{\partial h_o}{\partial x}$ is obtained from the bathymetric observation

A is measured from satellite imagery (width) and some points validated on the ground

S_f and S_o are deduced from the digital elevation model, and

Q is computed using Equation (3.2)

Thus, the simultaneous substitution of the computed value of Q from Equation (3.2) into Equation (3.2) allows the calculation of the actual flow rate $\frac{\delta Q}{\delta t}$ in Equation (3.1).

Again, Equation (3.3) is used to compute the stream flow rate:

$$F_r\left(\frac{\partial h_0}{\partial x}\right) = \frac{A \times L \times C}{T} \tag{3.3}$$

where

F_r = flow rate

A = cross-sectional area

L = length of reach

C = coefficient or correction factor to accommodate for the drag due to sediments and channel disturbance.

T = Time in seconds

Combining the water channel discharge capacity (Q) with the discharge rate ($\frac{\delta Q}{\delta t}$) and stream flow rate, the flooding potentials of the water channel was simulated using Equations (3.4), (3.5a) and (3.5b).

Water flux equation is expressed as:

$$W_f = \frac{\delta Q}{\delta t} \times F_r \tag{3.4}$$

where

W_f = water flux

$\frac{\delta Q}{\delta t}$ = discharge rate

$If\ W_f > Q$ River section is potentially flood prone $\tag{3.5a}$

$W_f \leq Q$ River section is not potentially flood prone $\tag{3.5b}$

3.3   Phase One: Acquisition, Preparation, and Correlation of Hydrological Data

The hydrological and weather-related parameters associated with the Shiroro dam were collected from Shiroro dam authorities for 20 years (i.e., 2001–2020) (Shiroro Dam Authority, 2020), prepared and correlated. The hydrological data comprises rainfall, temperature, inflow, water level, and outflow (water discharge). Appendices A1- A10 presents the hydrological data and the correlation of the hydrological data used for the study.

3.3.1   Bathymetry data

The river channel bathymetry of the Shiroro downstream was carried out in 2021 at random intervals. Nine hundred and fifty-five (955) data points were observed, and the data statistics are shown in Appendices A11. Calibrating the echo sounder is as essential as testing any land survey equipment for inherent errors and precision. It is done to keep the depth ping consistent. As the acoustic wave travels through the water medium, it is affected by the speed, salinity, temperature, and pressure of the water (Ojinnaka, 2007). It either slows the wave or increases it from the transducer to the seabed and its return signal. The echo sounder was calibrated by the bar-check method.

It was accomplished by lowering a flat plate beneath the echo sounder transducer to various known depths beneath the surface and comparing the measured depth to the actual depth. As the bar is moved down, the sound velocity in the echo sounder is adjusted until the measured depth matches the actual depth. Figure 3.2 shows the echo sounder calibration by the bar-check method.
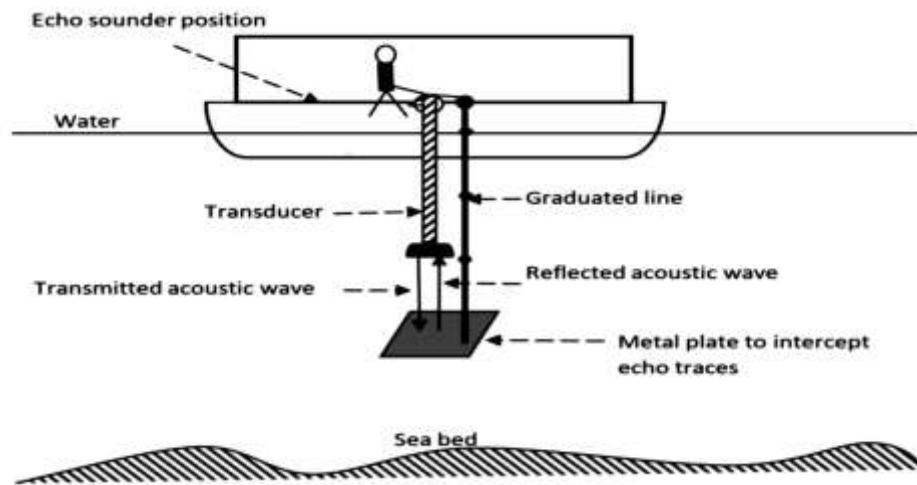
Figure 3.2: Echo sounder calibration by the bar-check method (Ojinnaka, 2007)

A Hi-Target DH Light Echo Sounder carried out the sounding operation. The Echo sounder was set up inside the vessel while its transducer was fixed to its side. The draught of the transducer was read and keyed into the system as 0.1 m. All ellipsoidal, time/date, frequency, velocity, and zone parameters were keyed into the system.

The horizontal datum employed for this work was the World Geodetic System (WGS 84). The Hi-Target DH Light Echo Sounder is configured with a dual-frequency GPS receiver just for the instrument. This receiver cable is connected to the Echo Sounder. Once the connection is established, the coordinates and speed of the vessel are displayed, as the speed

is a function of the vessel's position at any given time and is computed from the coordinates obtained.

3.3.2   Niger State Emergency Agency (NSEMA) damaged assessment data

The Niger State Emergency Management Agency (NSEMA) carried out a damaged assessment of the flooded area in Shiroro downstream, Shiroro local government area, Niger State, after the flood in 2021 using Global Position System (GPS) to access the communities affected by the flood, weighing the severity of the flood and the impact on the settlements and categorizing them as low and high through the physical inspection. Appendice A12 presented the NSEMA data used to validate the study. However, this information confirmed which of the three DEMs performs optimally in modelling floods in the study area.

3.4   Phase Two: Unmanned Aerial Vehicle DEM Generation

In this study, a fixed-wing unmanned aerial vehicle (UAV) equipped with a calibrated small-format digital camera, a GPS sensor tracking system, and an inertial navigation system (INS) form the data acquisition system. The establishment of ground control points helped in improving the aero-triangulation quality, and the processing of the data to obtain an orthophoto and a Digital Elevation Model (DEM) was generated by processing the acquired image pairs using Trimble's photogrammetric workstation. The Trimble UX5 was chosen because it is a fast and safe aerial data collection system with a robust design, simplified workflow, reversed thrust, and automatic failsafe procedures. It offers a safer method than traditional surveying methods and is fully automated, requiring no piloting skills (Lawali and Dauda, 2014; Olagoke *et al.,* 2017).

3.4.1 Mission and flight planning

Onboard the UX5 rover was a sensor (a calibrated camera) with a focal length of 24 mm and forward and side overlaps of 70% and 65%, flown at 200 m above the ground. Mission and flight planning was done with a software package called Trimble Access Aerial Imaging. Flight plans were edited both in the graphical and tabular sections of the screen. The mission was planned on Trimble Access Aerial Imaging software, UAS- Flight Operations Manual (UAS-FOM, 2017).

3.4.2 Initial flight planning

The initial flight planning entailed using Google Earth (GE) to execute an initial review and demarcation of the project area, which was then saved in Kemler file format. It was also essential to do initial flight planning as the GE imagery does not show dangerous obstructions such as cell towers, power lines, or other objects that could impede the flight plan. Part of the reconnaissance includes identifying an open, reasonably central location that can be used as the take-off and landing area, as well as obstructions like utility poles, trees, and buildings.

3.4.3 Establishment of ground control points (GCPs)

Ground controls can be avoided if the UAV has a dual-frequency GNSS sensor on board so that precise camera station coordinates are determined for each photograph, but in this case, the GNSS onboard the UAV is of a single frequency; hence, the GCPs were pre-marked across the project area before the flight (Karamuz *et al.,* 2020). The GCPs were surveyed using Trimble R8 GNSS receivers (Ahmad, 2014). Trimble Navigation's recommended default ground signal was used. Conspicuous existing natural or artificial features on the ground were used as checkpoints (ChP), considering the clarity of the aerial photographs

(Hughes *et al.,* 2005). The precise coordinates of all the GCPs were determined in a defined spatial reference frame (Azmi *et al.,* 2014).

Trimble R8 differential GNSS receivers were used to establish the ground control points (GCPs) and checkpoints (ChPs) in rapid static survey mode. With about 45 minutes of occupation time, 106 GCPs were established to considerably enhance the georectification quality, though it is insufficient for rough terrain. The WGS 84 reference ellipsoid in UTM Zone 32N projected coordinates was used as the spatial reference system, UAS-Flight Operations Manual (UAS-FOM, 2017). The coordinates obtained are presented in the appendix.

3.4.4   Image acquisition

The selection of flights was perfectly carried out, which covered the study area to alleviate the stress of processing the images due to the processing system configuration. Wind direction, take-off, and landing locations were defined on the UAV Ground Control Station (GCS) before the flight, UAS-Flight Operations Manual (UAS-FOM, 2017).

In preparation for the flight, the UAV, the Radio Connection (RC) transmitter, and the Ground Control System (GCS) were connected, and the flight mission plan was uploaded to the UAV Autopilot fixed in the eBay section. The UAV was launched after being fully armed for capture, and it hovered for about 15 minutes for each flight mission before landing. The flight ended on the GCS, after which the log data and captured images were downloaded. Each flight covers about 80 hectares and produces 200 images, according to the UAV Flight Operations Manual (UAV-FOM, 2017).

Details of the flight parameters for the UAV mission are provided in Table 3.3. The processing software (Trimble Business Center Photogrammetry Module, Version 3.30) was also used to extract the height of the buildings from the digital surface model to achieve the digital elevation model for the study area, which is the primary concern of this research.

Table 3.3: Flight planning parameters for the UAV mission

S/N	Parameter	Value
1	Flying height	200 m
2	Flight speed	12-15 m/s
3	Forward lap	70%
4	Side lap	65%
5	Camera focal length	24 mm
6	Flight time is approximately (Per flight)	15 minutes
7	Battery capacity	5350 mAH
8	Capacity of each image	6 megabytes
9	Number of GCPs	106 points
10	Number of GCPs used for georeferenced	60 points
11	Number of GCPs used for the adjustment of Tie points	46 points

3.4.5   Image processing

The flight was designed with generous overlaps of 70% (forward) and 65% (side), which produced 6-8 overlapping image frames, amounting to a large set of image data of about 6 megabytes per image frame. Consequently, the processing part of the UAV methodology is the most time-consuming. It involves performing a procedure referred to as "photo alignment," "tie point adjustment," "digital elevation model" (DEM) creation, and "orthophoto" production. The processing was done on the Trimble Business Center Photogrammetry Module application (version 3.30) installed on an HP laptop with the following configuration properties: 128 GB of RAM, an Intel® CoreTM i7 CPU 11th

Generation @ 2.80 GHz processor, a 64-bit operating system, and a 1 TB hard drive disk. The data was post-processed in a UTM 32N projected coordinate system referenced to the WGS 84 global ellipsoid. The 46 GCPs were used to adjust tie points (aero-triangulation), followed by the production of the digital elevation model, UAV-Flight Operations Manual (UAV-FOM, 2017).

3.5   Phase Three: Generation of InSAR 10 m DEM

This section provided the InSAR operational steps and processing chain for DEM creation from single-look complex (SLC) Synthetic Aperture Radar (SAR) data. The three operations are data structure, processing, and product validation. Data pre-processing, co-registration, interferogram creation, phase unwrapping, and geocoding are the additional processes that make up the data processing stage. The Sentinel Applications Platform (SNAP) version 8.0 processing software has to test the data processes utilizing SRTM data. The results of the stated processing procedures on actual data sets are in subsections 3.4.1 to 3.4.5.

3.5.1   Data search

The data search step entails looking for pertinent data that will guarantee sufficient data quality and produce the best outcomes possible for the InSAR processing. Typically, agencies in charge of providing SAR data are sought out. The Canadian Space Agency (CSA) and the European Space Agency (ESA) are the two organizations now in charge of running SAR satellites in the civilian sector. Since 1996, the CSA has had one SAR satellite in orbit, RADARSAT-1. In 2002, ESA launched ENVISAT, their third SAR satellite. The ERS1 and ERS2 satellites, their forerunners, gathered SAR imagery from 1992 to 2000 and from 1995 to the present, respectively.

In addition, a SAR satellite was run by the National Space Development Agency of Japan (NASDA) from 1993 to 1998. This satellite's SAR pictures collection is also accessible. Future satellite radar missions are in the works. These include the German TerraSAR (X-Band), the Japanese ALOS, and the Canadian RADARSAT 2 (C-Band).

3.5.2   Data processing

Data pre-processing, coregistration, resampling, computation of the interferogram, phase unwrapping, and geocoding are the five independent procedures that comprise the data processing stage (Figure 3.3). Sentinel Applications Platform (SNAP) version 8.0 is used in this work for data processing (Kampes, 2005; Kampes *et al.,* 2003). SNAP was selected since it is free interferometric processing software that is fully functional. SNAP adheres to the traditional UNIX tenet that each tool should have a single, clearly defined function, and a pipeline of simple tools should be used to build complex functions.

SNAP comprises several software applications (or modules) that carry out various interferometric operations. In order to carry out specific tasks that these programs can handle well, SNAP makes use of additional public-domain applications. These include GMT for general plotting and gridding (GMT, 2005), SNAPHU for phase unwrapping (SNAPHU, 2005), Getorb for acquiring precise orbital data records for the ERS satellites (Getorb, 2005; Scharroo and Visser, 1998), and PROJ.4 for coordinate transformations (USGS, 2005).

3.5.2.1 Step 1: Data input, data cropping, and oversampling

The input of the master and slave data sets for InSAR processing is the initial data processing stage. All processed data are single-look complex (SLC) data. It does not include radar and orbital raw data pre-processing. This step additionally reads orbit data acquired from the

getorb Web site to compute precise orbit. The SLC leader, volume, and header data files, as well as pertinent parameters, were then retrieved from the input files by SNAP. At this stage, data oversampling and amplitude calibration are also carried out.

```
┌─────────────────────────────────┐
│       Data Pre-Processing        │
└─────────────────────────────────┘
                  │
                  ▼
┌─────────────────────────────────┐
│       Co-registration and        │
│           resampling             │
└─────────────────────────────────┘
                  │
                  ▼
┌─────────────────────────────────┐
│ Computation of Interferometric Products │
└─────────────────────────────────┘
                  │
                  ▼
┌─────────────────────────────────┐
│        Phase unwrapping          │
└─────────────────────────────────┘
                  │
                  ▼
┌─────────────────────────────────┐
│           Geocoding              │
└─────────────────────────────────┘
```
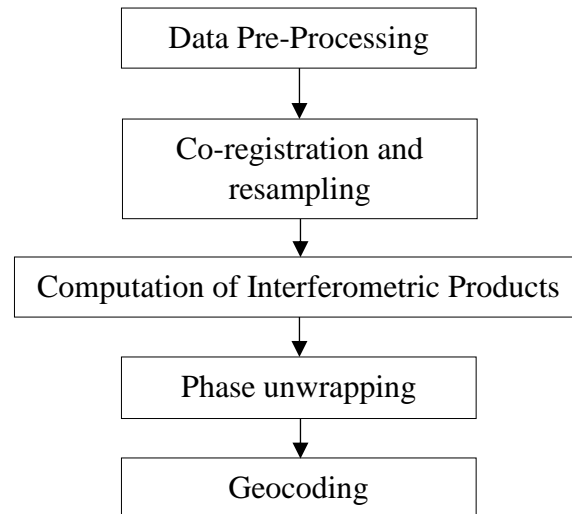
Figure 3.3: Data processing stage for InSAR DEM

(Source: Okeke, 2006)

3.5.2.2 Step 2: *Co-registration and resampling*

The co-registration polynomial, which was later used to resample the slave image to the master grid and define the transformation of the slave picture to the master image, is determined at this stage. In SNAP, this is accomplished in four steps. First, a single coarse offset on the pixel level between the master and slave images is computed using the orbital data of the master and slave. Then, using a cross-correlation on the intensity data of the master and slave on a select few relatively big patches, the estimate for this offset is enhanced.

The coarse offset previously calculated using the orbits serves as the beginning offset. The offset vectors between the master and slave are calculated at numerous small patches (64 × 64 pixels) in the third phase, the fine co-registration, employing a cross-correlation of the

intensity data. Finally, the slave picture is resampled to the master grid using the estimated polynomial.

3.5.2.3 Step 3: Computation of interferometric products

The interferogram and the coherence image are produced in this step. By default, SNAP computes the interferogram with a multilook factor of 5 for azimuth and 1 for range. A reference body's phase is considered when correcting the interferometric phase. The reference phase can be calculated using the WGS84 ellipsoid or another ellipsoid.

Additionally, SNAP can compute the coherence image that may be used as an input for the unwrapping program's cost function calculations. Different techniques can be used to do phase filtering. The Goldstein filter, 2D convolution kernels, and simple pre-defined spatial averaging kernels are just a few of the techniques used by SNAP to compute coherence images (Baran *et al.,* 2003; Goldstein and Werner, 1998).

3.5.2.4 Step 4: Phase unwrapping

The wrapped phase representation has been used to rebuild the initial phase. The computations for phase unwrapping are performed by SNAP using the SNAPHU phase unwrapping program (SNAPHU, 2005). Curtis and Zebker (2000) describe the SNAPHU phase of unwrapping software. It is a cutting-edge phase unwrapping program that computes the cost functions using the interferometric amplitude and coherence image, as well as data on the anticipated smoothness of the unwrapped phase.

3.5.2.5 Step 5: Geocoding

In this step, the pixel coordinates are geo-referenced, and the unwrapped phase is converted to a height. This stage produces the height of a substantial number of pixels on an asymmetric

grid of longitude and latitude pairings. However, these output matrices are gridded using the GMT tools, and transformation to the required coordinate system is performed using the PROJ.4 program.

3.5.3 Product validation

In this phase, the quality of the InSAR products is evaluated through comparison with a reference model acquired from independent sources. The existing second-order control points in the research area were used to validate that the interferometric phases are eventually transformed to heights (Okeke, 2006).

3.5.4 Generation of InSAR DEM

This section presents the methods used to generate inSAR DEM for the study from subsections 3.5.4.1 to 3.5.4.6.

Given two radar image phases, where the phases of images 1 and 2 are as given in Equations 3.6a and 3.6b,

$$\varphi_1 = \frac{4\pi}{\lambda} \cdot \rho_1 + n_1 \tag{3.6a}$$

$$\varphi_2 = \frac{4\pi}{\lambda} \cdot \rho_2 + n_2 \tag{3.6b}$$

where

φ = signal phase

ρ = signal range / distance measured

λ = signal wavelength

n = observation noise

The Equation (3.7) represents the phase difference

$$\Delta\varphi = -\frac{2\pi}{\lambda}\,\delta\rho \qquad\qquad\qquad (3.7)$$

In Equation (3.7), the range differences are obtained from the phase differences. Using the geometry of image data acquisition, point elevations can be determined by the Equation (3.8).

$$z = h - \rho\cos\theta \qquad\qquad\qquad (3.8)$$

where

z = elevation of point

h = height of satellite above ground level

θ = Azimuth

The Sentinel Applications Platform (SNAP) version 8.0 was used in this study to implement Equation (3.8) with the traditional DEM generation approach. The procedure for DEM generation is shown in Figure 3.4 Two single-look complex (SLC) images of the same area are accurately co-registered, and the interferogram is prepared. After that, the interferogram was subjected to flat-earth correction and smoothing using the Goldstein filtering approach. The minimum cost flow algorithm is used to unwrap the phases, and the interferometric phases are finally converted to heights using existing second-order control points in the study area (Okeke, 2006).

Throughout this study, the VH polarisation was selected for the interferogram formation. The SRTM 1-second Digital Elevation Model (DEM) was used as the reference Digital Terrain Model (DTM) for the processing of the flat earth model (Okeke, 2006). The choice of the SRTM 1-second height as a reference DEM for the flat earth model is to maintain consistency with the earlier study by Karabork *et al.* (2021). The use of the DEM (an optional process)

for interferogram generation allows the assignment of a reference cartographic system for the resulting DEM.
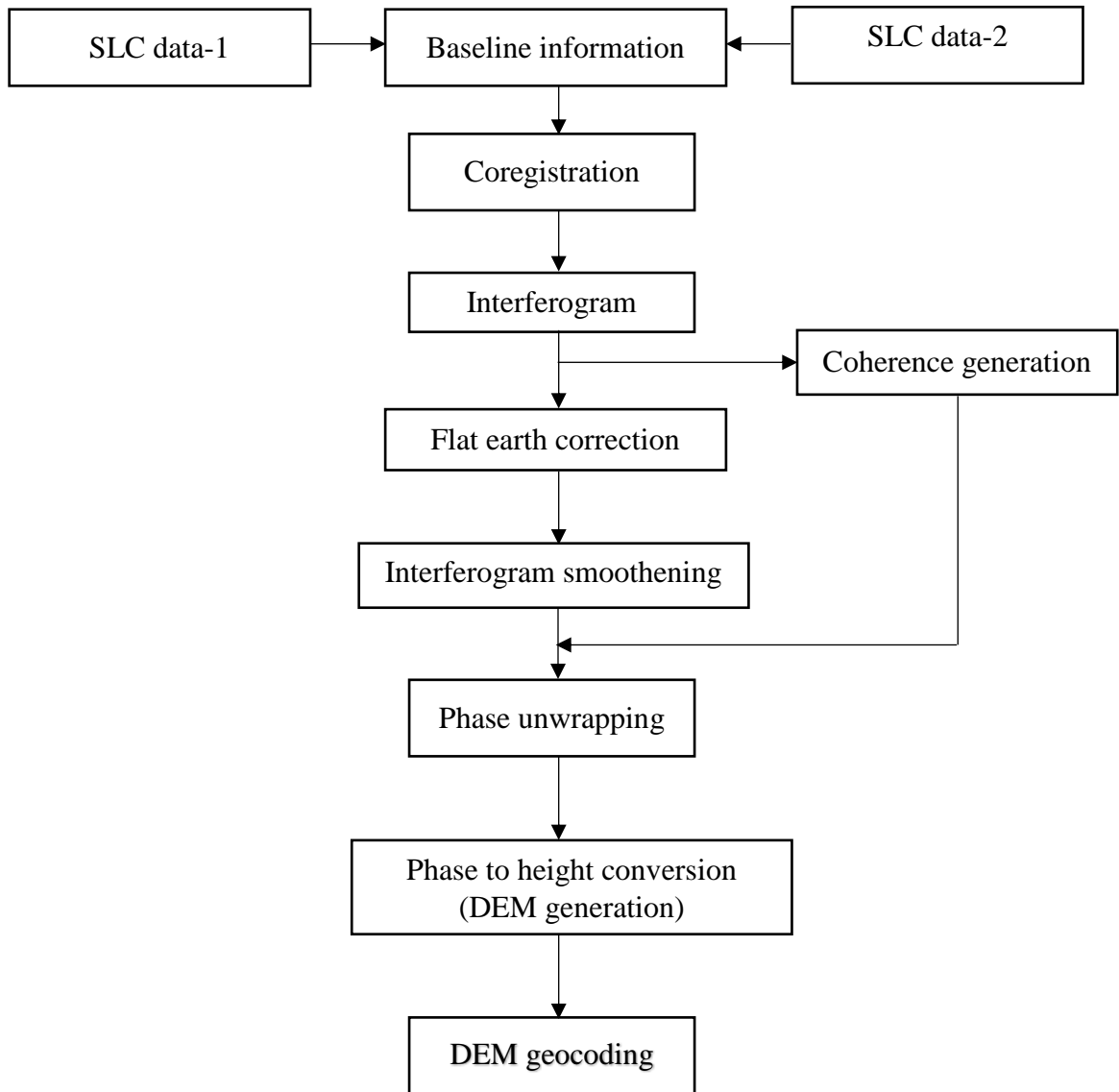
Figure 3.4: Procedure for interferometric analysis and DEM generation

(Source: Okeke, 2006)

3.5.4.1 Co-registration and implementation in SNAP

The SLC Level-1 product of IW with VV polarisation was selected for this process. The IW2 sub-swath with bursts numbered 1 to 9 with VV or VV+VH polarisation was obtained by splitting. The two split Level-1 SLC products, "Master" and "Slave," of the same sub-swath, were coregistered using the orbits of both images acquired at different times. The "slave" image is the one acquired at a later date, while the "master" image is the one acquired earlier. The co-registration also corrects the offsets in master and slave images regarding range direction and azimuth. Precise orbit files for Sentinel images were obtained from the European Space Agency (ESA).

The orbit files contain information about altitude, atomic time, and other real-time orbit data that can improve the baseline estimation and co-registration of these images (Yague-Martinez *et al.,* 2016). The co-registration ensures that a particular ground target will be in the same pixel (range and azimuth) in both the master and slave images. Because the sensor velocity and altitude in Sentinel satellites are relatively stable, the 6-parameter similarity transformation was used to approximate the entire frame of the SAR image pairs in 100 x 100 square kilometers.

3.5.4.2 Interferometry generation implementation in SNAP

Two sets of phases appear in the interferogram, one due to the elevation and the other due to a change in the relative position of the scatters. Removing phase due to elevation or topography is called interferogram flattening, which gives the phase change relative to the reference surface from the master image. The reference image was calculated using a polynomial degree of 5. A total of 501 points were selected for flat-earth estimation, as this is an optimal number for an area of up to 100 square kilometers. Had this process been

skipped, fringes due to the earth's curvature would have appeared in the interferogram. Figure 3.4 shows the interface of the interferogram formation Graphical User Interface (GUI) in SNAP.

3.5.4.3 Coherence estimation implementation in SNAP

The interferogram formation operator in SNAP was used to compute the interferogram and the coherence bands by selecting the stack after back geocoding and using ESD as an input.

3.5.4.4 De-bursting, topographic phase removal and filtering

Debursting is the process of joining and resampling all the bursts from a swath into a single image. VH and VV polarizations were selected for deburring as the data was acquired with these polarizations. The phase produced by the topography needed to be cancelled out so that relative changes could be observed. The complex interferogram was flattened using the 30-m-resolution SRTM DEM (Berti *et al.,* 2013).

The following corrections were further applied to the interferogram:

i.   **Subtract of the flat-earth phase:** The flat-earth phase is the phase present in the interferometric signal due to the curvature of the reference surface. The flat-earth phase is estimated using the orbital metadata information and subtracted from the complex interferogram.

ii.   **Subtract the topographic phase:** Flat terrain should produce a series of regularly spaced, parallel fringes. Topographic variation can be interpreted as any deviation from a parallel fringe pattern. When topographic phase removal is applied, the SRTM 1-sec HGT (Auto-Download) is selected during implementation in SNAP.

iii. **Include coherence estimation**: This produces a coherence band in the output calculated based on a window of 10 x 3 pixels in range and azimuth direction.

As topographic phase removal was applied, the interferogram should only contain variations from displacement, atmosphere, and noise. The patterns, also called "fringes," represent a full 2-cycle and appear in an interferogram as cycles of arbitrary colors, with each cycle representing half the sensor's wavelength. Relative ground movement between two points is later derived by counting the fringes and multiplying by half the wavelength. The closer the fringes are together, the greater the strain on the ground. The coherence shows the areas where the phase information is coherent, which means it can be used to measure deformation or topography (without removing the topographic phase). If low-coherence areas are too dominant in the image, the later Unwrapping will fail and produce faulty or random results.

3.5.4.5 Signal filtering

Noise from temporal and geometric decorrelation, volume scattering, and other processing errors can corrupt the interferometric phase. Phase information in decorrelated areas cannot be restored. However, the quality of the fringes existing in the interferogram can be increased by applying specialised phase filters, such as the Goldstein filter, which uses a fast Fourier transformation (FFT) to enhance the signal-to-noise ratio of the image. It is required for a proper unwrap in the subsequent step. Goldstein phase filtering is another residue-reducing method that enables better phase Unwrapping in the later stages. A non-linear adaptive algorithm proposed by Goldstein and Werner (1998) was used. The value of the filter component ranged from 0 to 1, with higher values resulting in more robust filtering. Therefore, the value of 1 was selected. Selecting a coherence threshold means that the areas with a coherence of less than 0.4 will be neglected as the areas have a higher degree of noise.

3.5.4.6 Phase unwrapping

The observed phase has a modulus of two (2), which means that a sine function describes the phase of the wave. It is an ambiguous measurement of phase. However, the phase is only measurable in wavelength, which is 0.5 cm in the case of Sentinel-1A. These wavelengths need to be converted to general linear units to be summed. Phase unwrapping identifies the sum of cycles that need to be added to the wrapped phase such that the explicit phase can be known for each pixel, and this is defined by the Equation (3.9) given by Ferretti *et al.* (2007):

$$\psi = \emptyset + 2\pi . n \qquad (3.9)$$

The phase unwrapping uses the statistically low-cost Network-flow Algorithm for Phase Unwrapping (SNAPHU), which makes the interferometric phase and coherence bands compatible by creating the band details, metadata, and processing parameters in a configuration file (snafu. conf). A minimum cost flow was before exporting the data. This iterative process is a network flow technique. This algorithm uses maximum a posteriori probability (MAP) estimation by maximising the conditional probability given wrapped phase, coherence, and intensity (Chen and Zebker, 2001). The results of SNAPHU processing are imported into the SNAP for further processing so that the metadata and bands of the unwrapped data can be together with the SNAPHU-processed data, which makes the data compatible with InSAR processing.

3.6   Phase Four: SRTM 30 m DEM Download

The 30 m SRTM data used in this study was from the US Geological Survey website, http://earthexplorer.usgs.gov. The Shuttle Radar Topography Mission (SRTM) was a collaborative mission between the National Aeronautics and Space Administration (NASA) and the National Imagery and Mapping Agency (NIMA), which is now known as the

National Geospatial-Intelligence Agency (NGA) (Nwilo *et al.,* 2012). The aim is to produce more refined elevation data, Digital Terrain Elevation Data (DTED). The system uses Spaceborne Imaging Radar-C (SIR-C) technology to acquire elevation data. The generated digital elevation model uses radio detection and ranging (RADAR) interferometry and the principle of stereoscopy (Tom and Mike, 2000). The region of coverage is between 60^0N and 56^0S, and its resolution varies from 1 arc second (30 meters) within the USA to 3 arc seconds (90 meters) outside the USA (Farr *et al.,* 2007; Slater *et al.,* 2006).

Masood and Takeuchi (2011) noted that SRTM data is advantageous for flood modelling because SRTM vertical accuracy is partially fair on relatively flat terrain such as floodplains in the absence and cost of high-resolution DEM (Farr *et al.,* 2007; Slater *et al.,* 2006) elevation range in the study area ranges from as low as 2 meters in the south to as high as 47 meters in the far north. Because of two issues with SRTM data, as identified by Li *et al.* (2021), SRTM has many invalid areas, i.e., areas where the quality of SRTM data is poor, and SRTM in some areas represents a Digital Surface Model rather than a DEM (Farr *et al.,* 2007; Slater *et al.,* 2006). This study thus adopts the methodology shown in Figure 3.5. The regions were detected, analyzed, and filled using the adopted by Li *et al.* (2020).
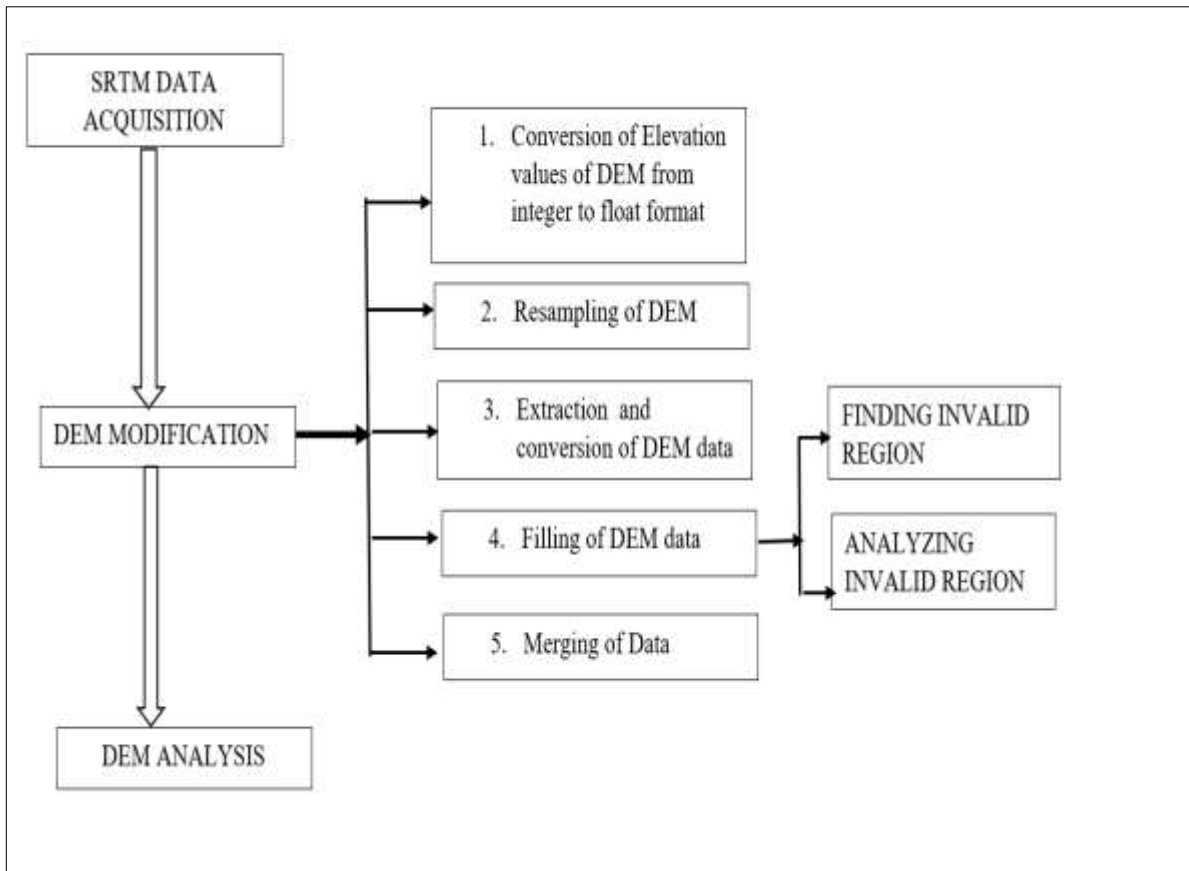
Figure 3.5: Methodology for processing SRTM data

(Source: Ugbelase *et al.,* 2021)

3.7:   Phase Five: Methods

The research aims achieved by the hydraulic analysis through the combination of hydraulic
and topographic modelling data in this study. Numerical data relating to river flow dynamics,
surface topography, and climatic conditions around the Shiroro floodplain were collected and
analysed using shallow water equations.

3.7.1 The flood modelling approach used

Generally, river floods spill over into the floodplains by continuous water flows whose magnitude and flux exceed the carrying capacity of the water channel. The flow of water is by the channel geometry, hydrodynamic, and topographical factors in the study area.

Due to the recurrence of floods worldwide, equations are used to study the phenomenon of floods. Considering that water flows directly under gravity, the discharge rate of the water using the conventional 2D shallow water equation by Vila *et al.* (2017). The Shallow Water Equation (SWE) describes many physical phenomena based on physical laws, mass, and momentum conservation. The solution of the Shallow Water Equation (SWE) gives the variation of discharge (and depth) with time along the length of the water body (river, stream, or channel), which is for flood forecasting. The equations referred to in Section 3.2.

A flood model requires a 3D simulation of flood hazard assessment from river cross-sections of river route areas in DEMs from different platforms, like aerial photography, optical stereo imagery, or SAR interferometry. To achieve the research objectives, the following methods, as discussed in sections 3.2 to 3.5, were utilised:

3.7.2 Flood simulation approach

ArcScene for ArcGIS 10.4 software was used to model floods in the study area. ArcScene simulates surface flooding caused by rainfall and river flooding. Before flood simulation in ArcScene, the river discharge and flow velocity were computed in MATLAB software using the conventional shallow water equation in Equations (3.1), Section 3.2. Similarly, to compute the flood levels, equations (3.4), (3.5a), and (3.5b) in Section 3.2 were implemented in MATLAB using the river bathymetry data and the different DEMs.

Thus, using the start and end nodes as major identification points along the water channels (catchment areas) for the stream, the river discharge of each identified node provided a basis for determining levels that can be obtained from the stream given an initial discharge. The initial discharge value used for simulation corresponds to the dam discharge when the spillway is opened.

3.8 Statistical Analysis Used for the Study

The following statistical analyses were performed on the obtained data. The study made use of the subheading statistical tools from 3.8.1 to 3.8.4.

3.8.1 Standard deviation

The variability or dispersion of data points within the research study was measured in this study using the standard deviation. The standard deviation offers essential insights into the distribution of data around the mean, enabling one to evaluate the consistency or variability of measurements and eventually assisting in the interpretation and analysis of the findings. The square root of the variance was used to convert from variance to standard deviation. Equation 3.10 provides the standard deviation's mathematical expression.

$$S = \left(\frac{\sqrt{((N-1)*\Sigma(X-\bar{X})^2)}}{N} \right) \tag{3.10}$$

Where S represents the standard deviation, N denotes the sample size, x represents individual data points, and $\bar{x}$ represents the mean of the data (Adebanji, 2014).

3.8.2   Analysis of variance (ANOVA)

The statistical technique known as ANOVA examines the mean differences between two or more variables. Checking for statistically significant variations between the means of two or more variables is done using this method. The F-statistic, which the ANOVA test generates, is used to assess if there are any statistically significant differences between the means of the variables under comparison. The variance between the variables is divided by the variance within the variables to determine the F-statistic. There is evidence to imply substantial differences between the means of the groups being compared if the F-statistic is higher than the critical value. In this work, the DEM sources were subjected to an ANOVA analysis.

The best resolution was determined in the study by comparing the means of flood modelling results at various resolutions using ANOVA. It made it possible to locate the DEM with the geographic resolution that yields the most precise or ideal flood modelling outcomes. The ANOVA was conducted in Microsoft Excel to examine the variation in flood modelling results among the various resolution groups after the null and alternative hypotheses were set up. To ascertain significant differences in the group, the F-statistic and P-value were determined. Based on the findings, a choice was made on the best resolution for the flood model.

3.8.3   Root mean square error (RMSE)

A statistical technique called RMSE is used to assess the precision of a predictive model. It calculates the discrepancy between the expected values and the actual values and gives a single number as a measure of the model's overall accuracy. RMSE is frequently used in data implementation to analyze the efficacy of predictive models. It indicates how well a model fits a given set of data and can be used to assess model modifications or to compare several

models (Zhang *et al.*, 2022). The RMSE was employed to rate the accuracy of the digital elevation models utilized for hydrological studies.

$$\text{RMSE} = Sqrt \left[\frac{(\Sigma(P_i - Q_i^2))}{n} \right] \qquad (3.11)$$

where,

P_i=denotes the predicted values

Q_i=represents the observed values, and

n= is the total number of observations or data points

3.8.4 Correlation analysis

Correlation analysis was used in this study to compare DEM data (UAV, InSAR, and SRTM). The correlation coefficient, which measures how closely elevation values from different datasets relate to one another, was determined using the elevation data of the datasets. A low or nearly negative correlation coefficient denotes disparities or a lack of agreement, while a high positive correlation coefficient denotes similarity between the elevation datasets from the two datasets.

$$(-1 \leq r \geq +1) \qquad (3.12)$$

3.9   DEM Implications on the Hydrological Analysis of the Study Area

Since flooding is generally a response of free-flowing water to anthropogenic, hydrological, and hydraulic characteristics within the study area, the hydrological analysis of the study area is consequent upon the chosen or adopted DEM in this section. The three DEMs (UAV, InSAR, and SRTM) for the study were subjected to hydrological analysis, and the parameters deduced were as follows: (1) The flow direction map (2). Flow accumulation map: a stream

connectivity map showing the surface runoff paths. The study used a strahler layer size of 5-7. Watersheds within the catchment area.

3.10   DEM Implications on the Hydraulic Modelling of the Study Area

Hydraulic analysis on UAV-1 m, InSAR-10 m, and SRTM-30 m DEMs was carried out using the two parameters determined from the hydraulic modelling using the Shallow Water Equation (MATLAB), river discharge and flow velocity for the two flood levels (low and high) determined for the study area comparison was done.

3.11   Phase Six: Model Validation

The validation method used in this study is the ground truthing or field verification method. In this case, simulation results were validated, with known realities established and compared, and the closer the simulation to reality, the better the simulation model. The results from the study by the situation assessment report acquired from the Niger State Emergency Management Agency were validated (NSEMA, 2021). A comparison of the simulation results with those in this report revealed that UAV-derived 1 m resolution DEMs provide high accuracy in flood simulation when compared to global DEMs. These all show convergence with the conclusions derived from this study by Unger *et al.* (2014), Leitao and de Sousa (2018), and Esmaeel *et al.* (2022). Due to security challenges within the study location, the study could not use direct field checks of the simulation results. Hence, the model validation relies strictly on the damage assessment carried out by NSEMA.

CHAPTER FOUR

4.0   RESULTS AND DISCUSSION

4.1   Results

The results obtained in this study are presented in line with the research objectives but in phases similar to the methodology for easy understanding. Except where otherwise stated in the methodology or result section, all numerical computations used a given mathematical formula expressed in a MATLAB environment.

4.2   Hydrological Data Results Presentation

This section presented the hydrological data preparation results.

Figure 4.1 shows the average monthly inflow data. Figure 4.2 shows the average monthly temperature data; Figure 4.3 presents the average monthly temperature data; Figure 4.4 displays the average monthly water level data; and Figure 4.5 shows the average monthly outflow data obtained from the hydrological processed data.
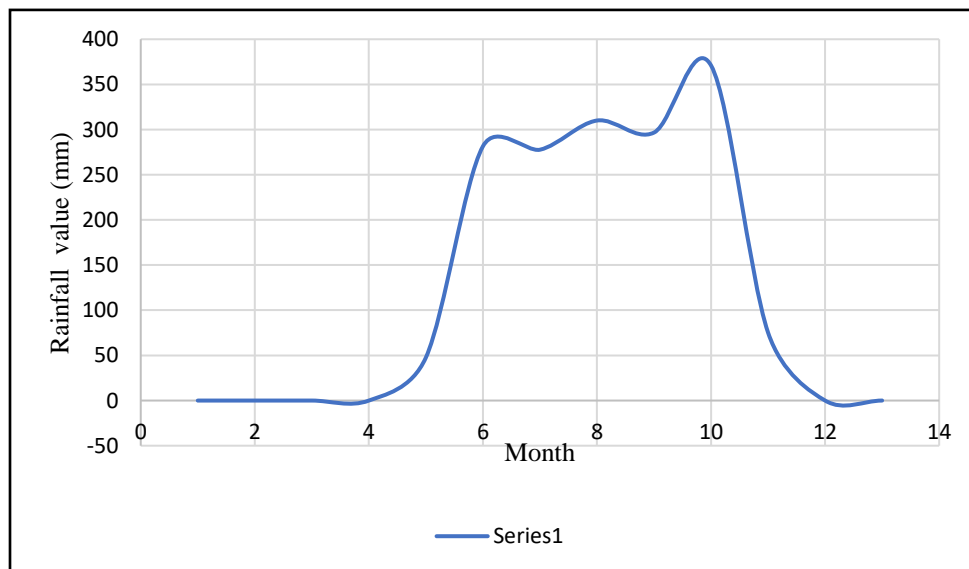
Figure 4.1: Average monthly rainfall data
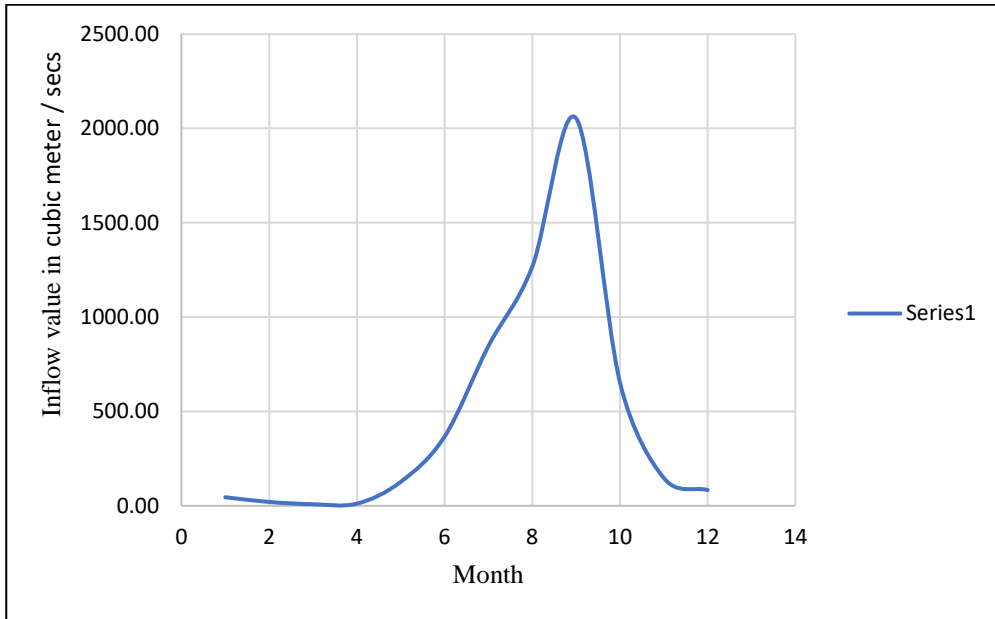
Figure 4.2: Average monthly inflow data
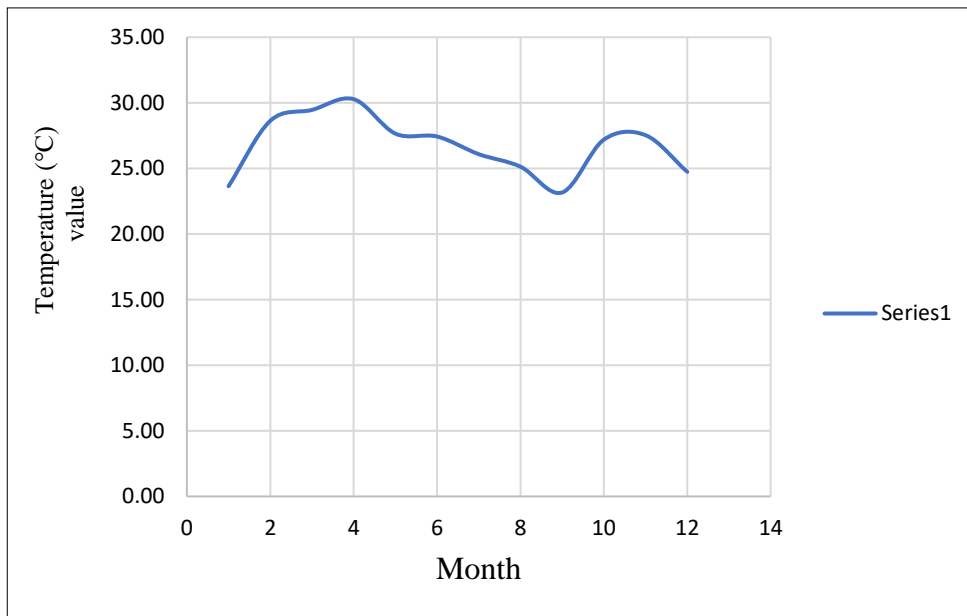
Figure 4.3: Average monthly temperature data
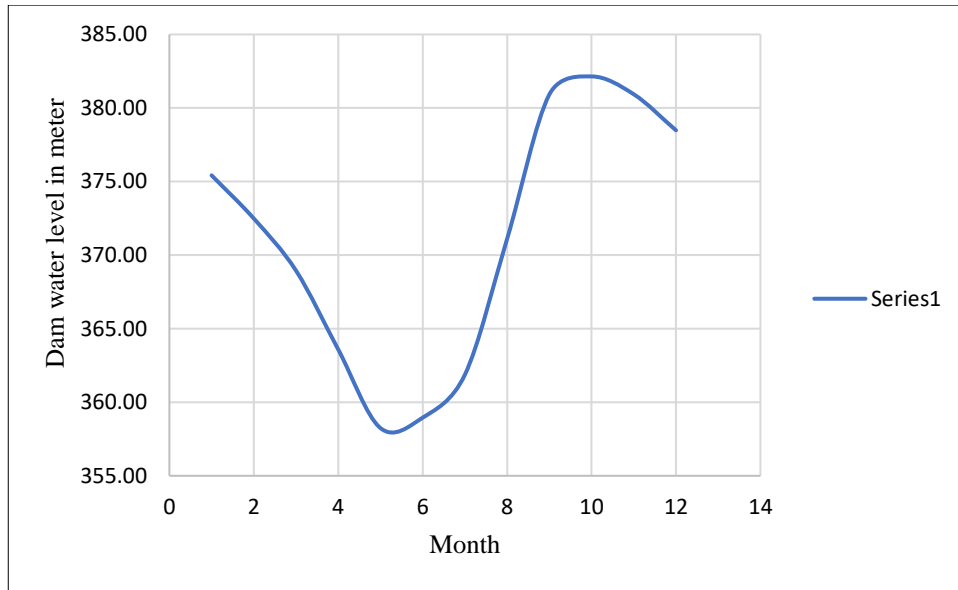
Figure 4.4: Average monthly water level data.
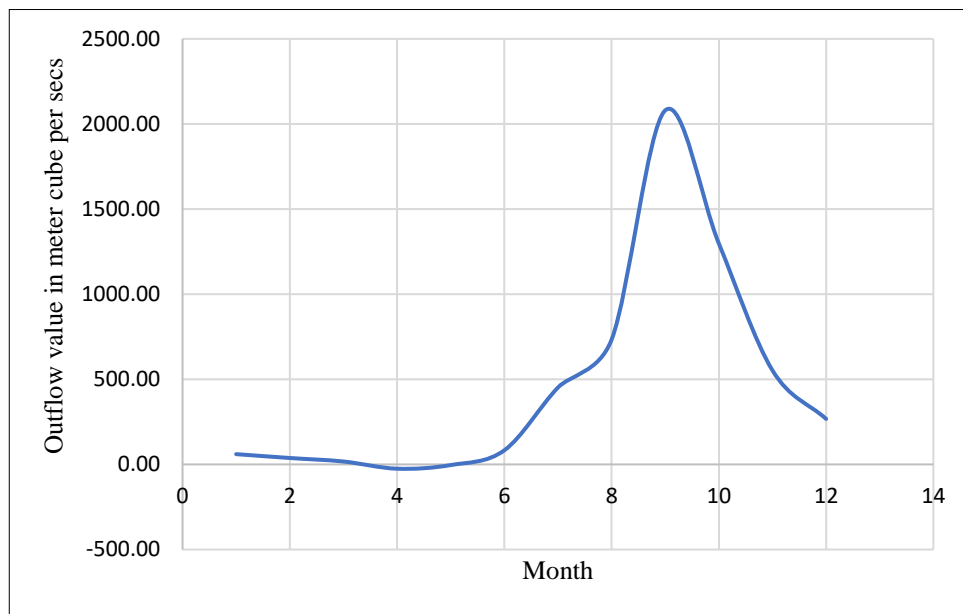
Figure 4.5: Average monthly outflow data

4.3   Hydrological Data Results Correlation

This section presented the hydrological data correlation results.

Figure 4.6 shows the correlation between rainfall and water level data, Figure 4.7 shows the correlation between Inflow and rainfall data, Figure 4.8 displays the correlation between the

correlation between water level and inflow data, Figure 4.9 presents the correlation between Inflow and outflow correlated data, and Figure 4.10 shown the correlation between water level and temperature correlated result.
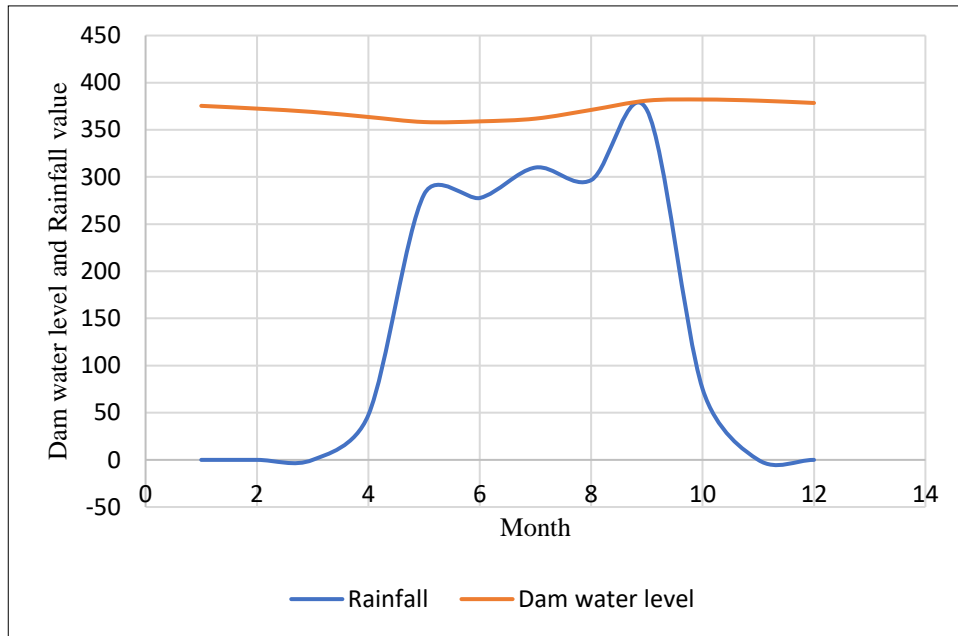
Figure 4.6: Rainfall and water level data
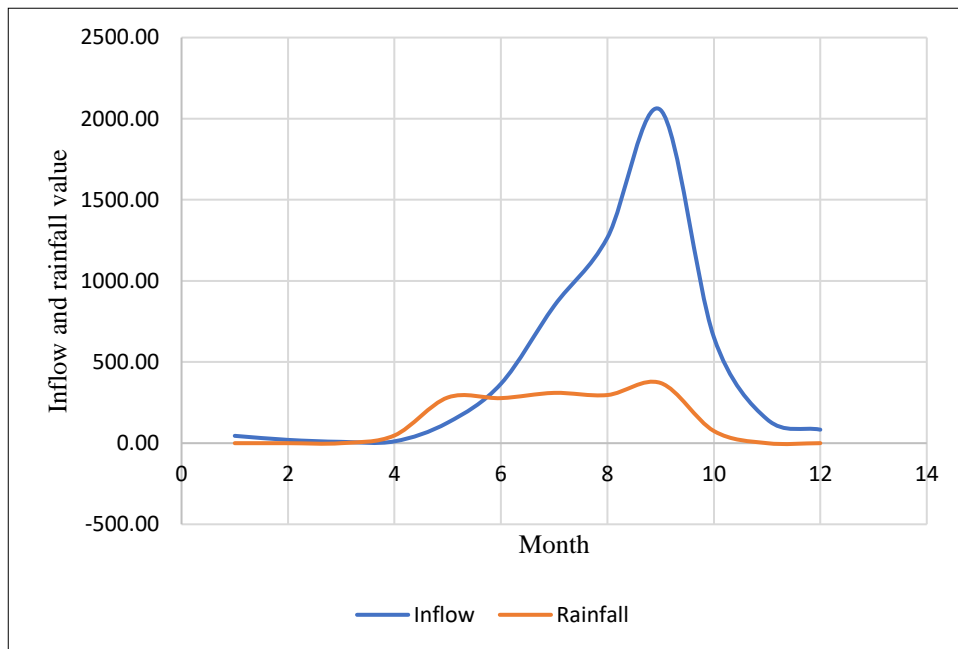
Figure 4.7: Inflow and rainfall data
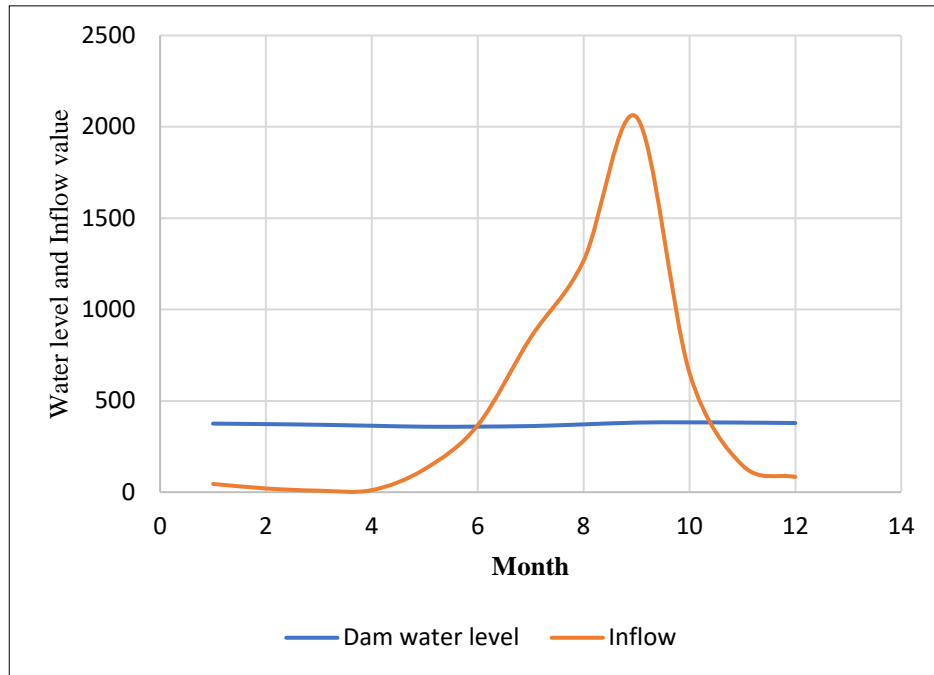
Figure 4.8: Water level and inflow data
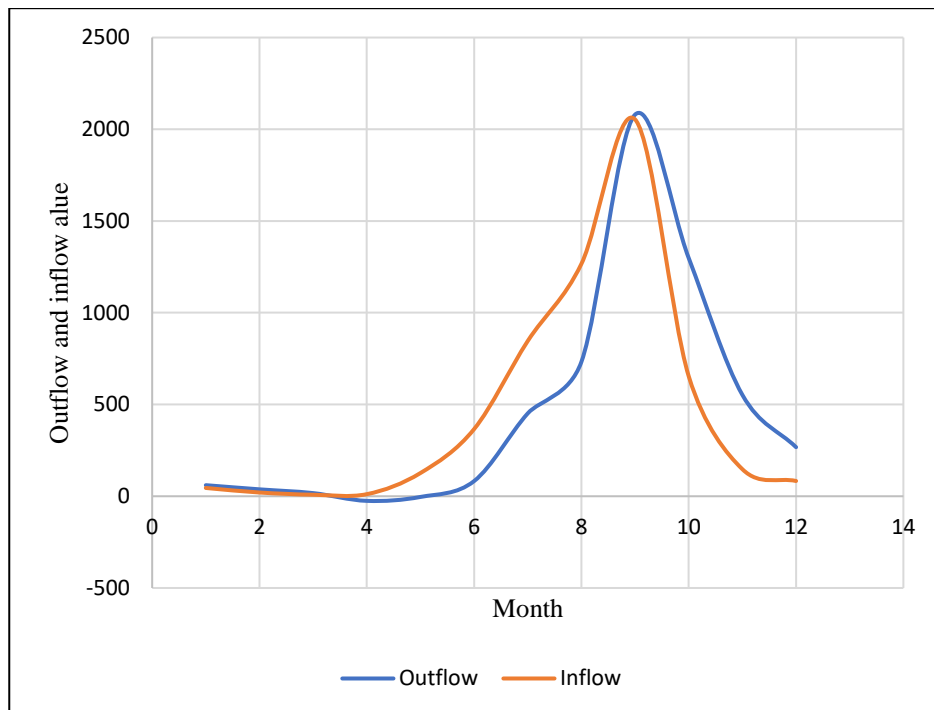
Figure 4.9: Inflow and outflow data
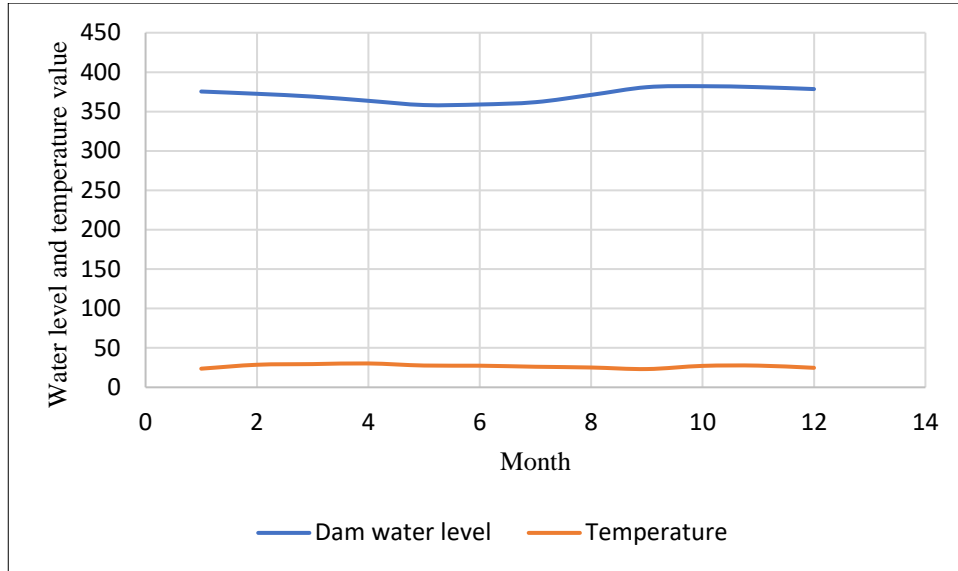
Figure 4.10: Water level and temperature

4.4 Bathymetry Data Results Presentation

This section presented the river channel bathymetry of the Shiroro downstream carried out at random intervals. Nine hundred and fifty-five (955) data points were observed, and the data statistics are shown in Table 4.1.

Table 4.1: Summary of bathymetric information for the study area

SN	Parameter	Value (m)
i	Minimum depth	0.95
ii	Maximum depth	2.15
iii	Average depth	1.20
iv	Total number of points	955

4.5   NSEMA Damaged Assessment Results Presentation

Appendices A12 presented the NSEMA data as low and high settlements used to validate the study. This information confirmed which of the three DEMs performs optimally in modelling floods in the study area.

4.6   Digital Elevation Models (DEMs)

This section presented the results of the three DEM sources used for the study.

4.6.1   UAV DEM

Figure 4.11 shows the DEM obtained from the UAV survey.
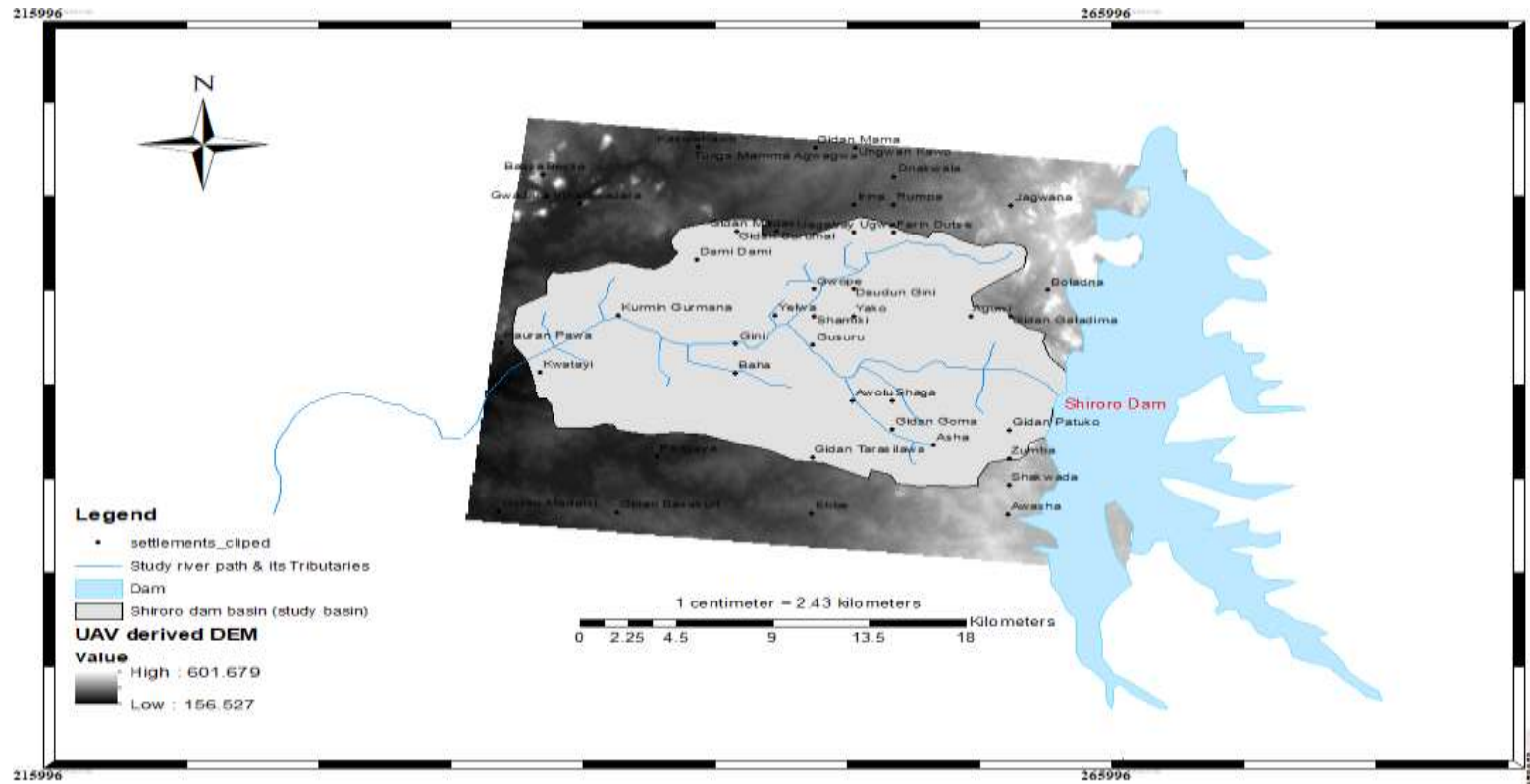
Figure 4.11: UAV 1 m DEM generated

4.6.2 InSAR DEM

The coherence, interferogram, and DEM maps of the study area generated by the SentiNel Application Processing (SNAP) software are in Figures 4.12 a, b, and c. The resulting DEM, as shown in Figure 4.12 (c), is further subjected to analysis as presented in later sections. However, Figure 4.13 shows the 10-m final DEM generated from InSAR.

(a) Coherence process
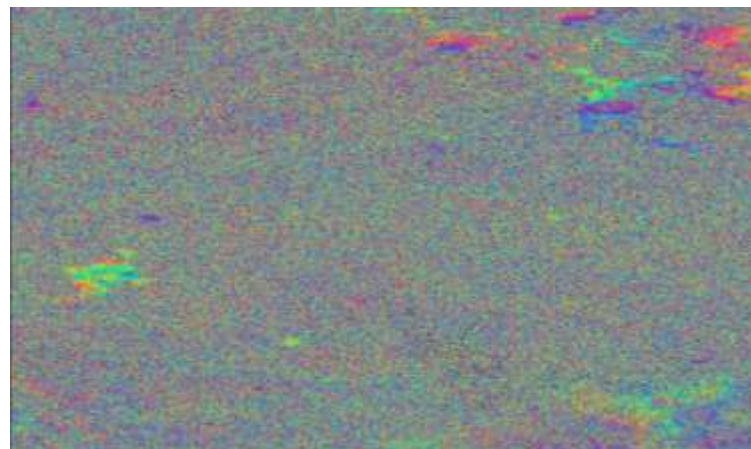
(b) Interferogram process
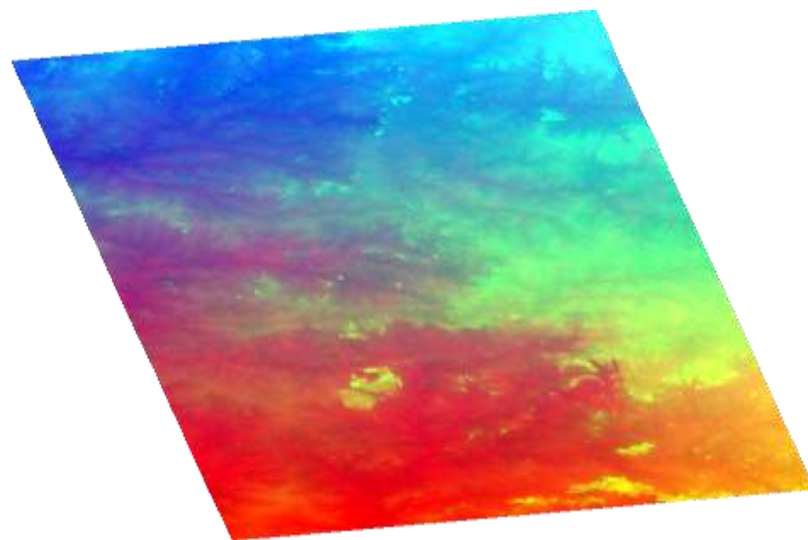
(c) DEM

Figure 4.12 a, b, c: Extraction of data results from InSAR DEM processing

105

Figure 4.13: InSAR 10 m DEM generated

4.6.3 SRTM DEM

Data from the SRTM was extracted using ArcGIS 10.4 software, and the resulting DEM generated is in Figure 4.14.
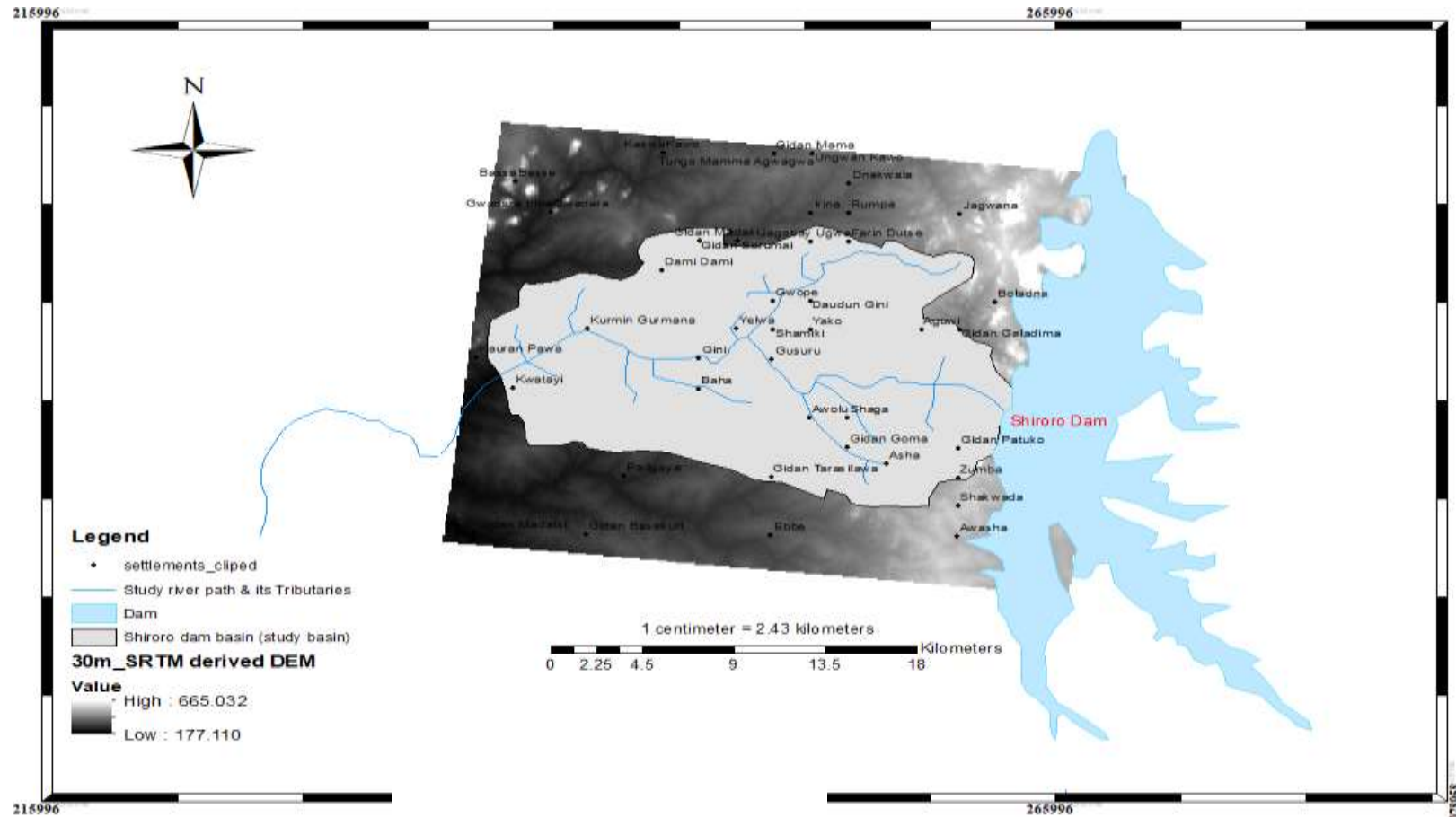
Figure 4.14: SRTM 10 m DEM generated

4.6.4 Comparative assessment of the DEM sources

For ease of comparison, all three DEMs are shown in Figures 4.15 (a, b, and c).

(a) UAV 1 m DEM

(b) InSAR 10 m DEM
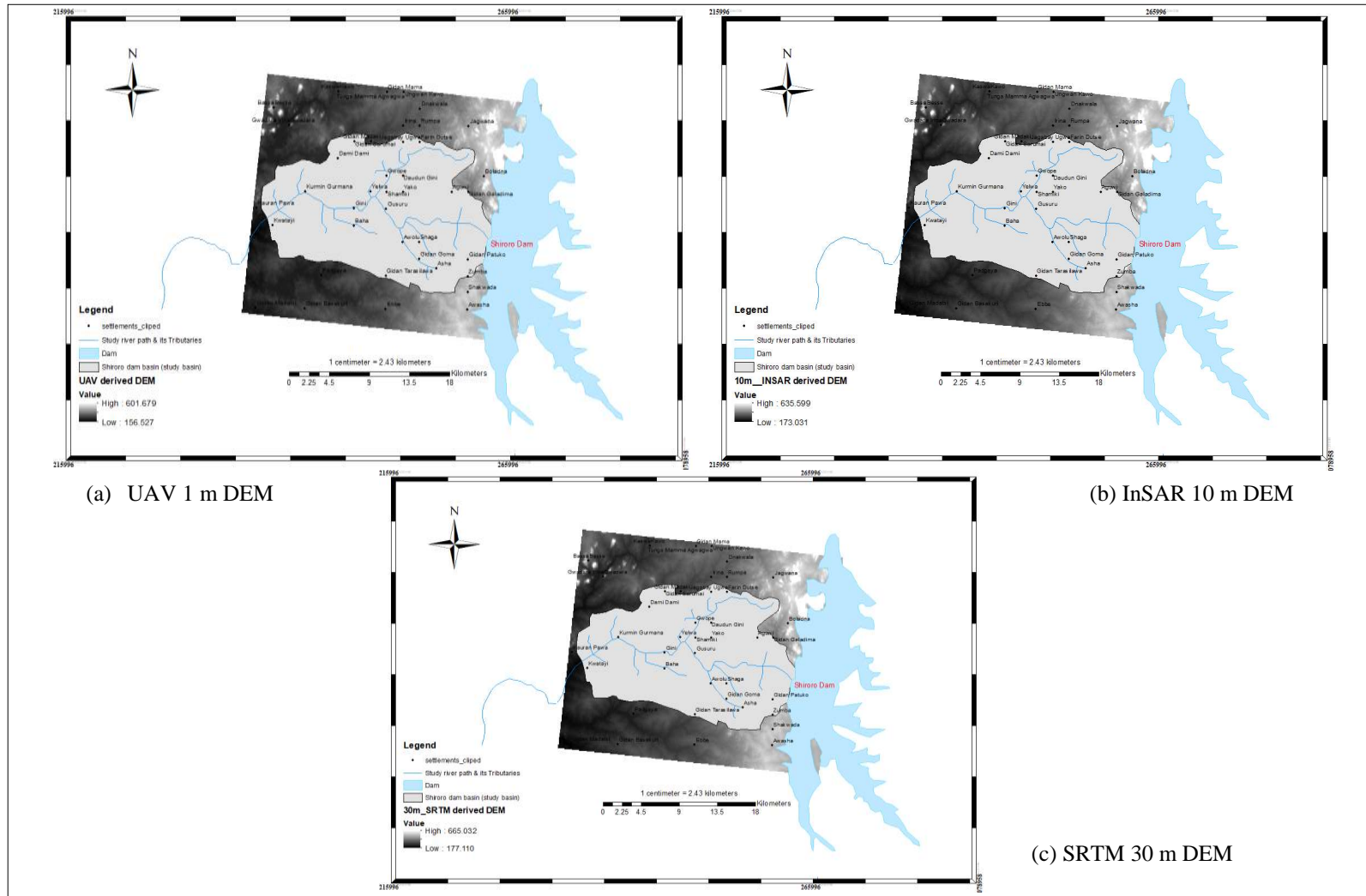
(c) SRTM 30 m DEM

Figure 4.15: Comparative assessment of the three DEMs (a) UAV 1 m DEM (b) InSAR 10 m DEM (c) SRTM 30 m DEM

Table 4.2 shows the descriptive statistics of the three generated DEMs. Figure 4.16 displays the descriptive difference statistics for UAV-derived 1 m, InSAR 10 m, and SRTM 30 m DEMs.

Table 4.2: Descriptive statistics of the DEM sources

Parameter	UAV (m)	InSAR (m)	SRTM (m)
Min	156.527	173.031	177.110
Max	601.679	635.599	665.032
Range	445.152	458.489	492.000
Average	323.903	348.594	357.991
Std dev	84.707	87.290	93.622
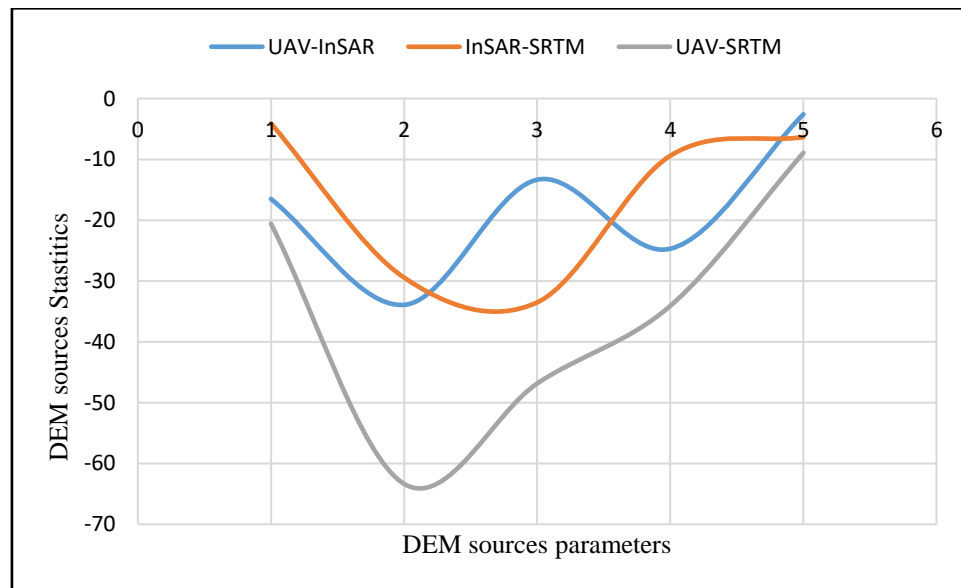
Figure 4.16: Descriptive difference statistics for UAV, InSAR, and SRTM DEMs

Analysis of the variances (ANOVA) between UAV, InSAR, and SRTM data using a single-factor analysis was carried out (Tables 4.3 and 4.3a). While Table 4.4 presents the correlation analysis between the three DEMs.

Table 4.3: ANOVA test (single factor) summary table

Groups	Count	Sum	Average	Variance
UAV	10000	3239034	323.903	7175.299
INSAR	10000	3485940	348.594	7619.554
SRTM	10000	3579913	357.991	8765.043

Table 4.3a: ANOVA test (single factor) result table

Source of Variation	SS	DF	MS	F	P-VALUE	F-CRIT
Between Group	6199743.4	2	3999872	394.722	6.184 E-170	2.996
Within Group	235575409	29997	7853.299			
Total	241775152	29999				

Table 4.4: Correlation analysis of the DEMs

DEM	InSAR	SRTM	UAV
InSAR	1		
SRTM	0.999639	1	
UAV	0.999639	0.999524	1

4.7   Implications of the DEM on Hydrological Analysis of the Study Area

This section presented the hydrological analysis results on DEMs sources for the study area.

Figures 4.17-4.19 show the flow direction map, while Figure 4.20 shows flow accumulation and surface runoff generated from all three DEMs. The river watersheds derived from the selected DEMs are presented in Figures 4.21– 4.23, while the significant morphometric characteristics of the river basins are shown in Table 4.5.
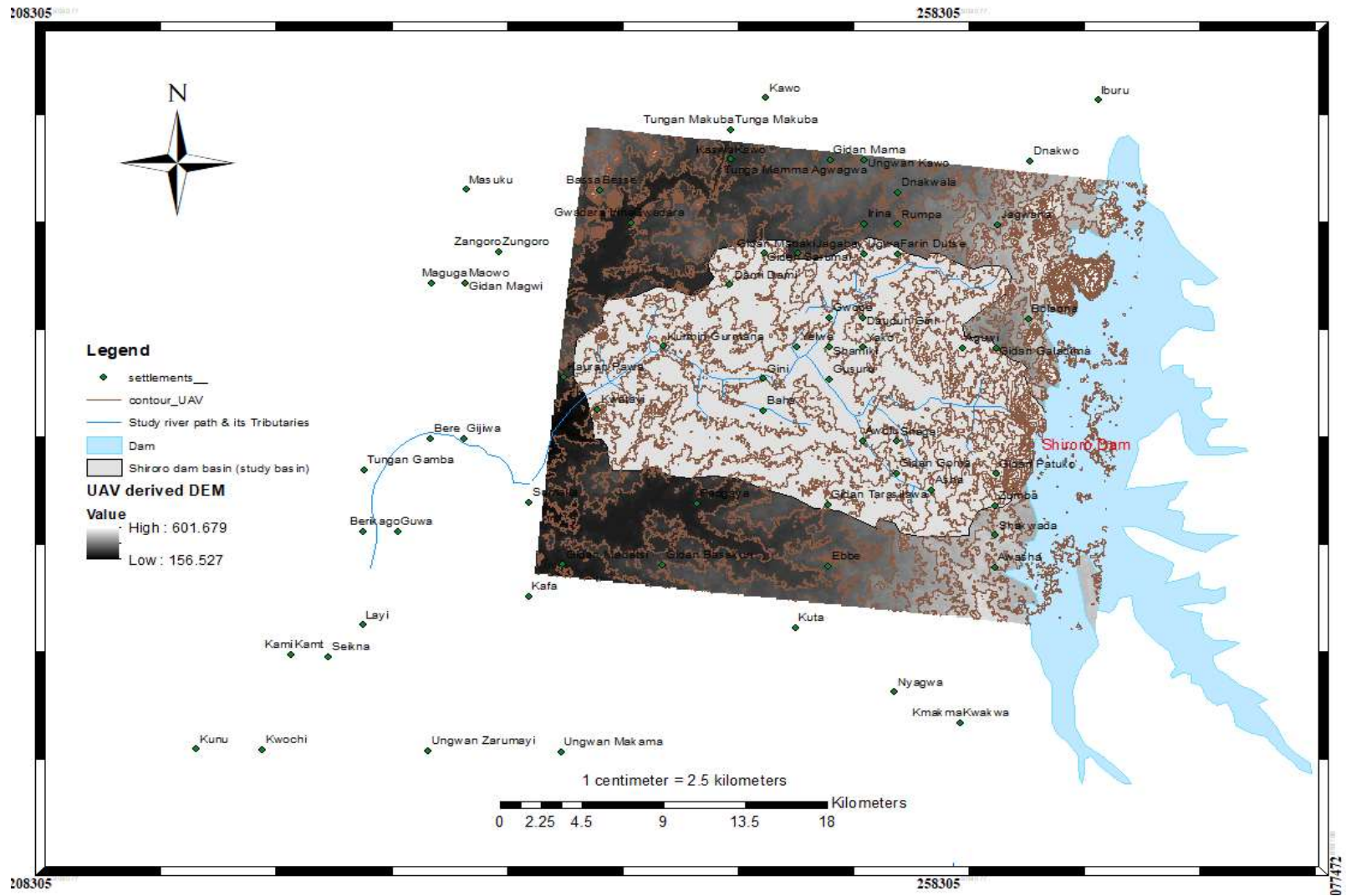
Figure 4.17: Flow direction from UAV 1 m DEM
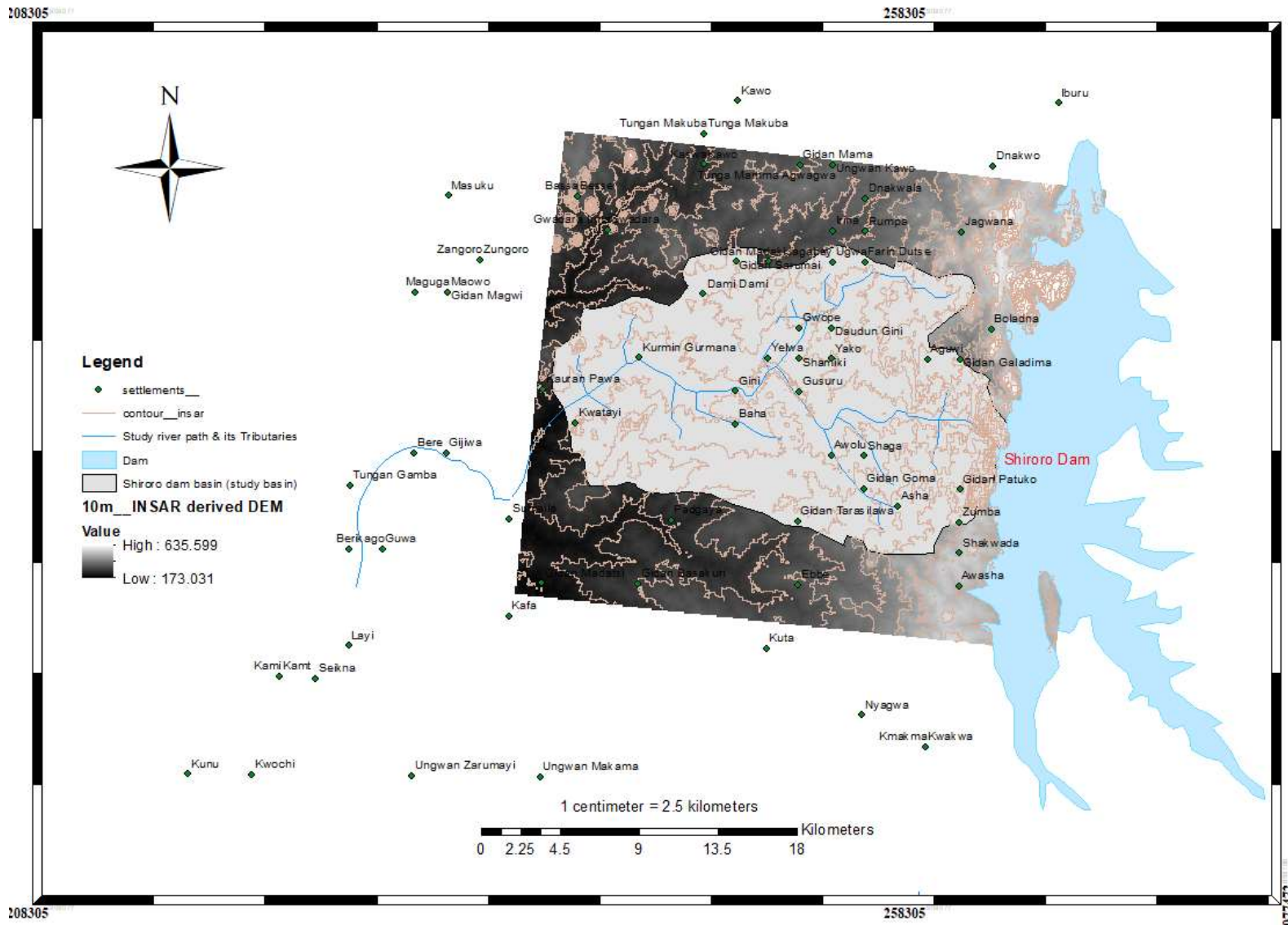
Figure 4.18: Flow direction generated from InSAR 10 m DEM
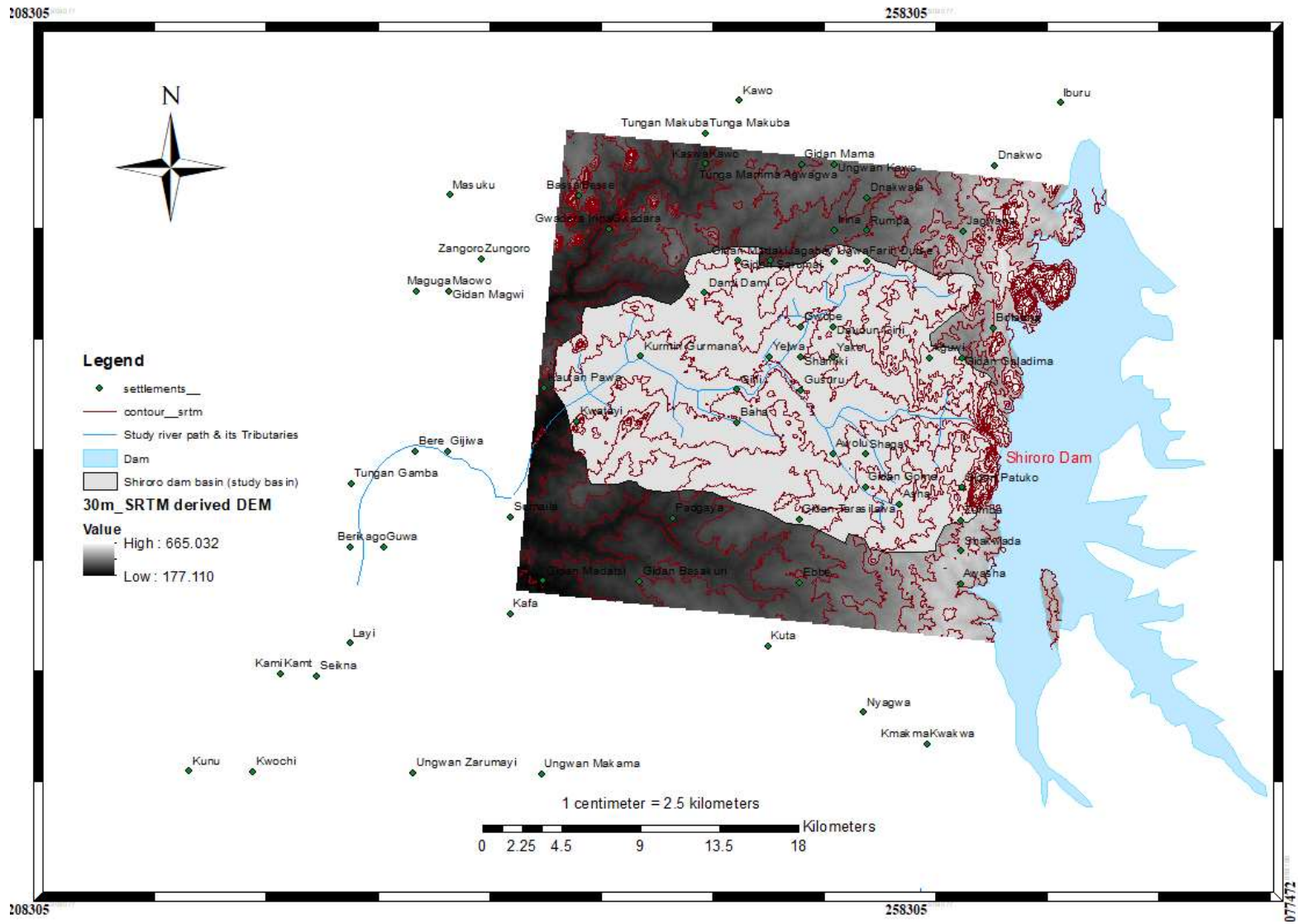
Figure 4.19: Flow direction from SRTM 30 m DEM
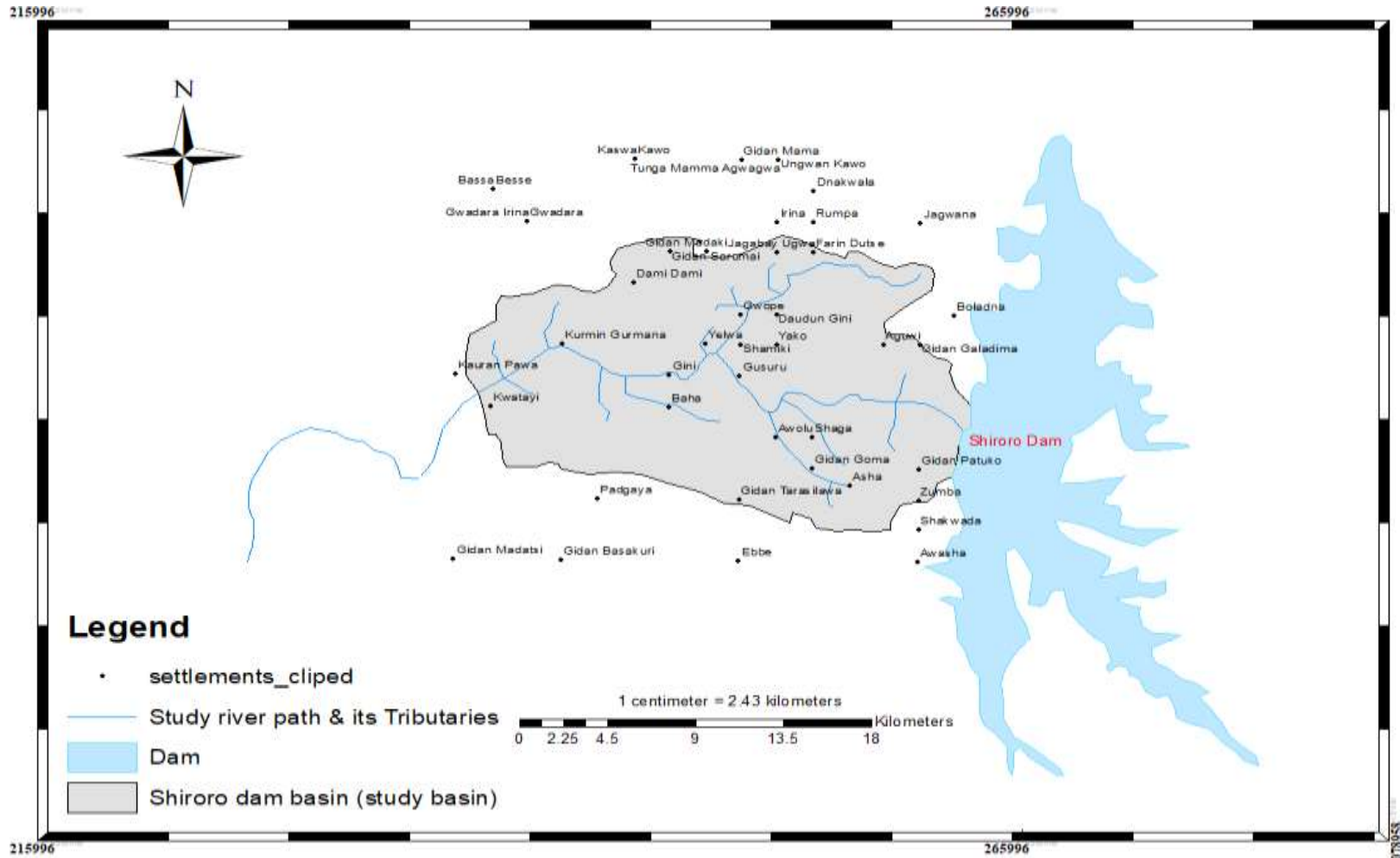
Figure 4.20: Flow accumulation generated from the DEMs source
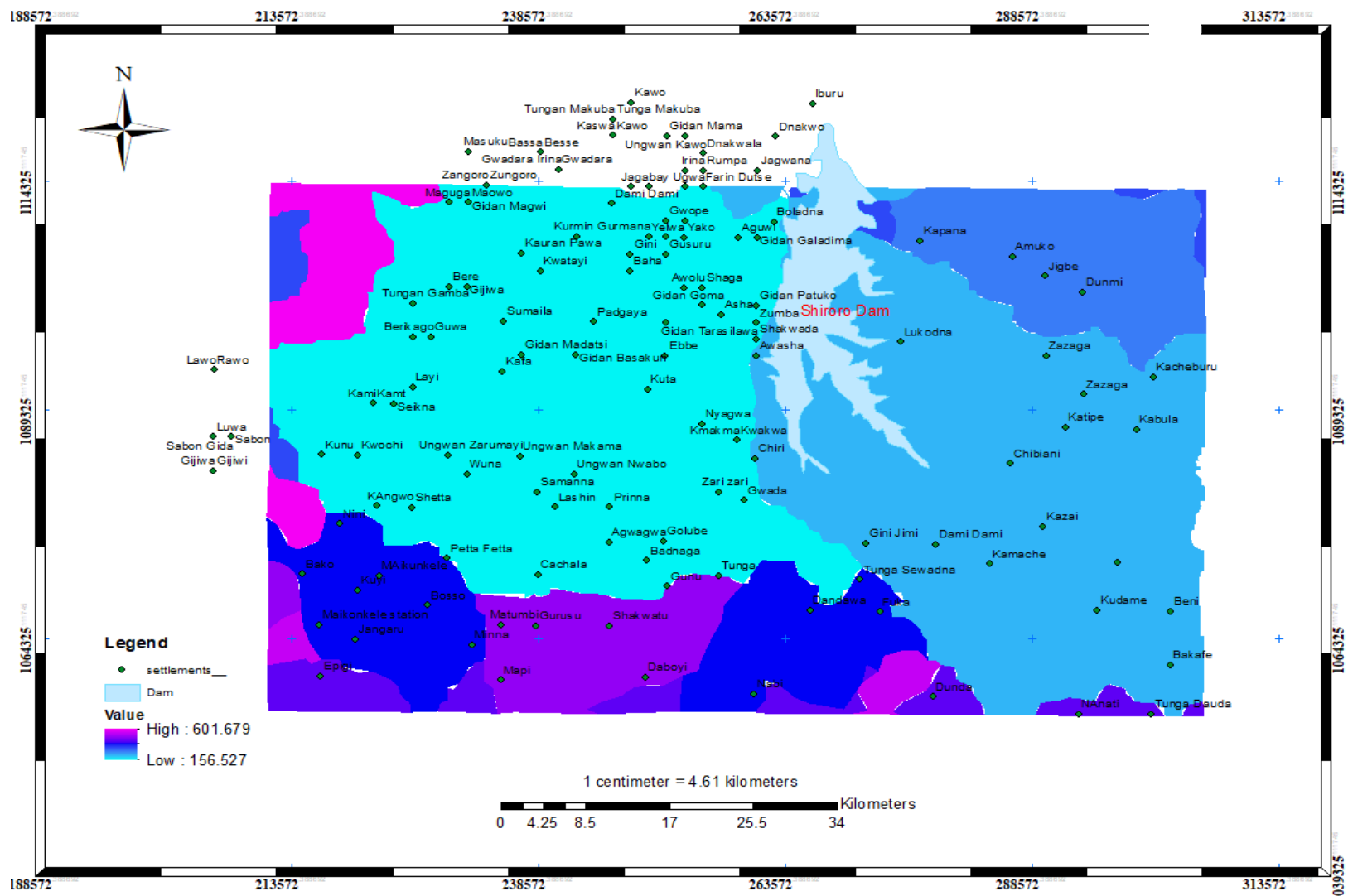
Figure 4.21: Watershed generated from UAV DEM
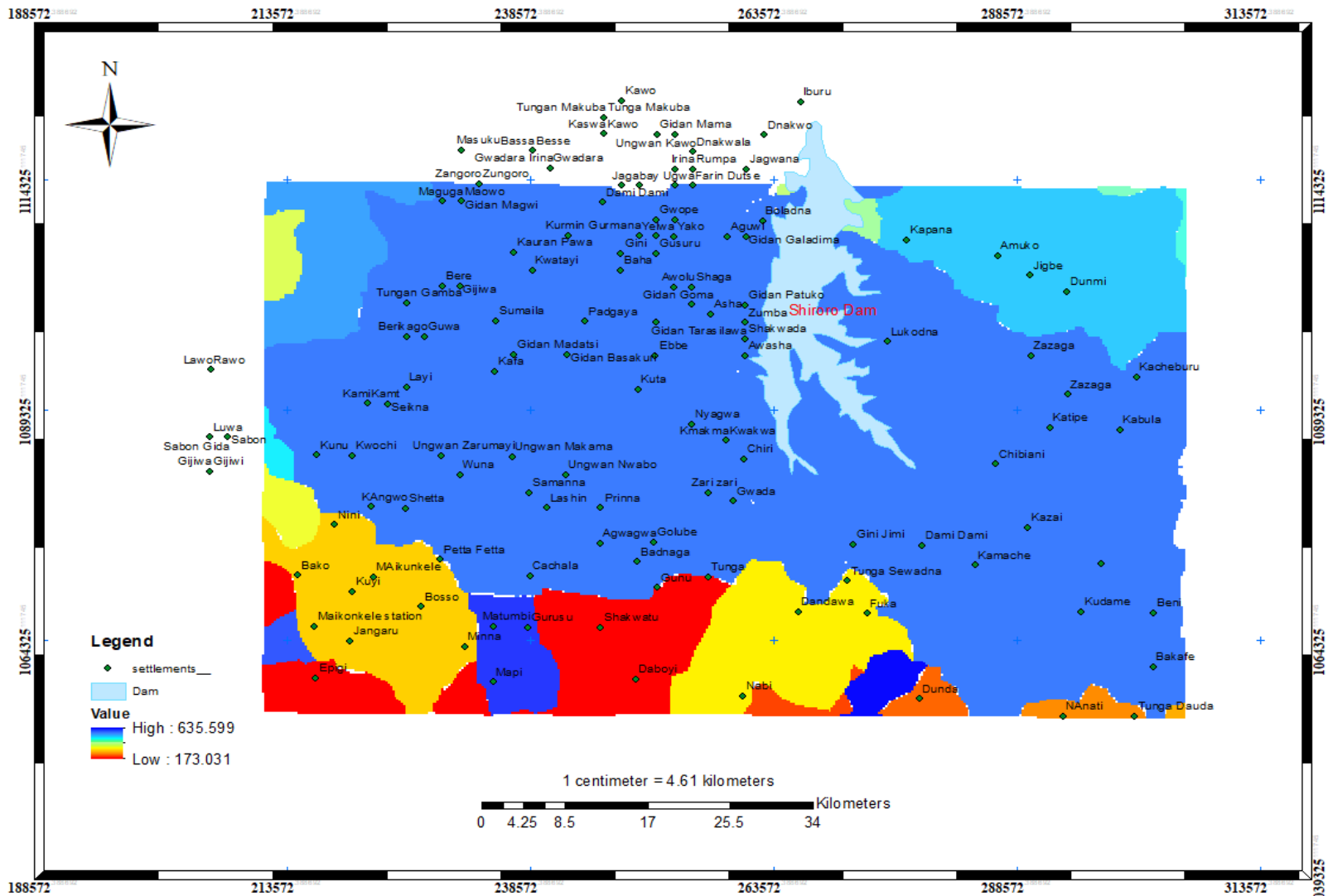
Figure 4.22: Watershed generated from InSAR DEM

Figure 4.23: Watershed generated from SRTM DEM

Table 4.5: Summary of the study area's hydrological characteristics

SN	Hydrological Parameter	UAV 1 m DEM	InSAR 10 m DEM	SRTM 30 m DEM
i	Total no of basins	14	10	13
ii	No of major basins	6	6	8
iii	Size of largest basin	(43.5 by 30.2) km	(42.8 by 30.8) km	(34.7 by 30) km
iv	Size of smallest basin	(6.6 by 12.4) km	(6.1 by 3.9) km	(4.7 by 3.98) km
v	No runoff streams/tributaries	Same network	Same network	Same network

4.8 Implications of the DEM on Hydraulic Analysis of the Study Area

Figures 4.24 (a,b, and c) show the graphical representation of the discharge rate, flow velocity, and elevation for UAV-1 m, InSAR-10 m, and SRTM-30 m DEMs, while the graphical differences in parameters between the discharge rate, flow velocity, and elevation for the UAV-1 m, InSAR-10 m, and SRTM-30 m DEMs are in Figures 4.25 (a, b, and c). Appendices B1, B3, and B5 summarise the discharge rate, flow velocity, and elevation for the DEM sources. At the same time, the differences in parameters between the discharge rate, flow velocity, and elevation for the DEM sources are presented in Appendices B2, B4, and B6, respectively.
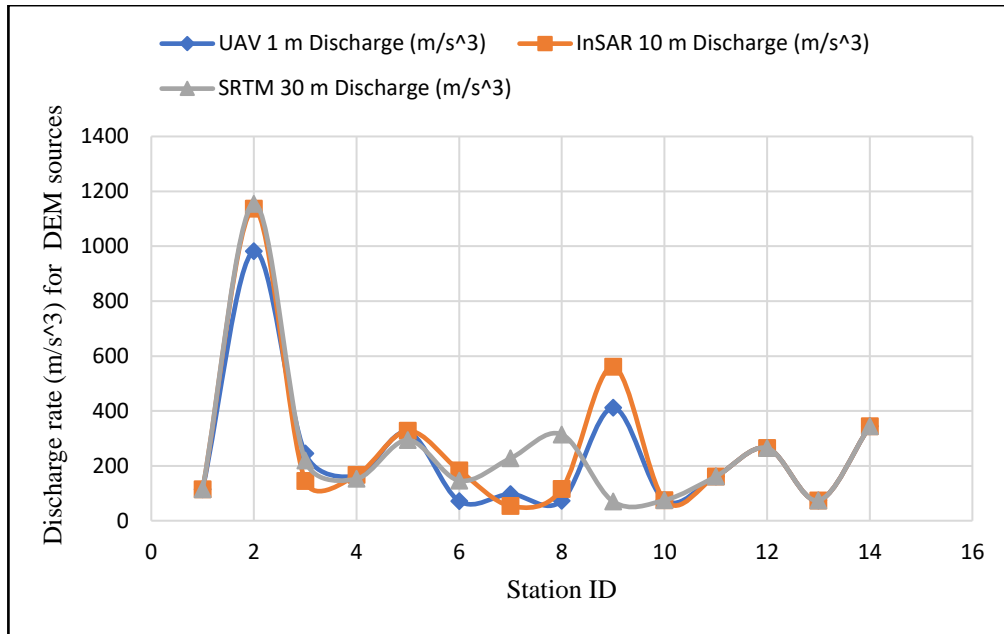
Figure 4.24a: Discharge rate for selected nodes from DEM sources
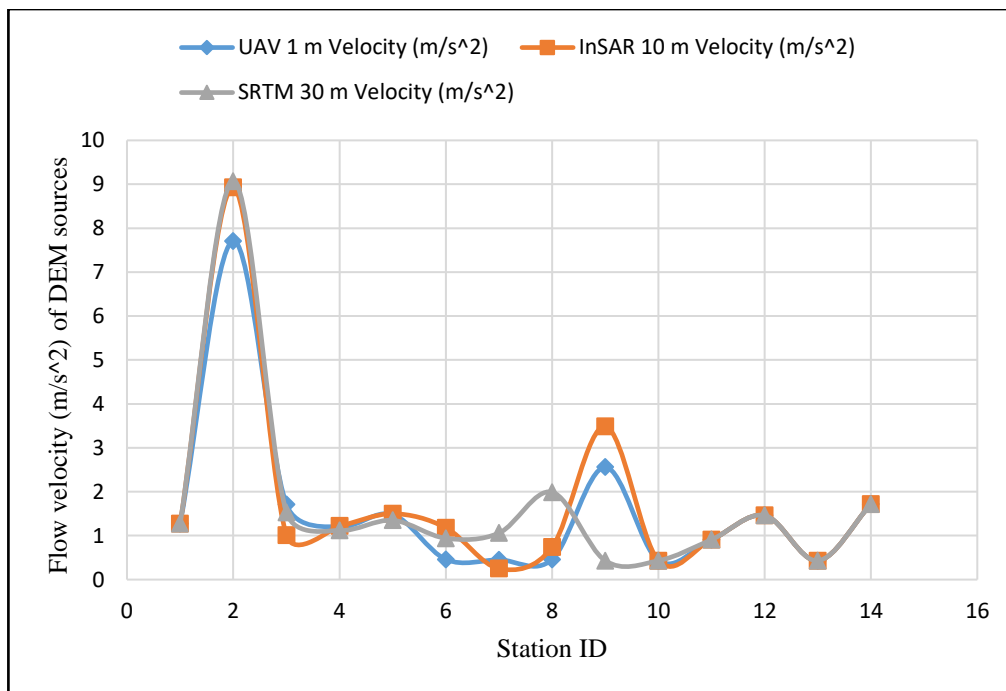
Figure 4.24b: Flow velocity for selected nodes from the DEM sources
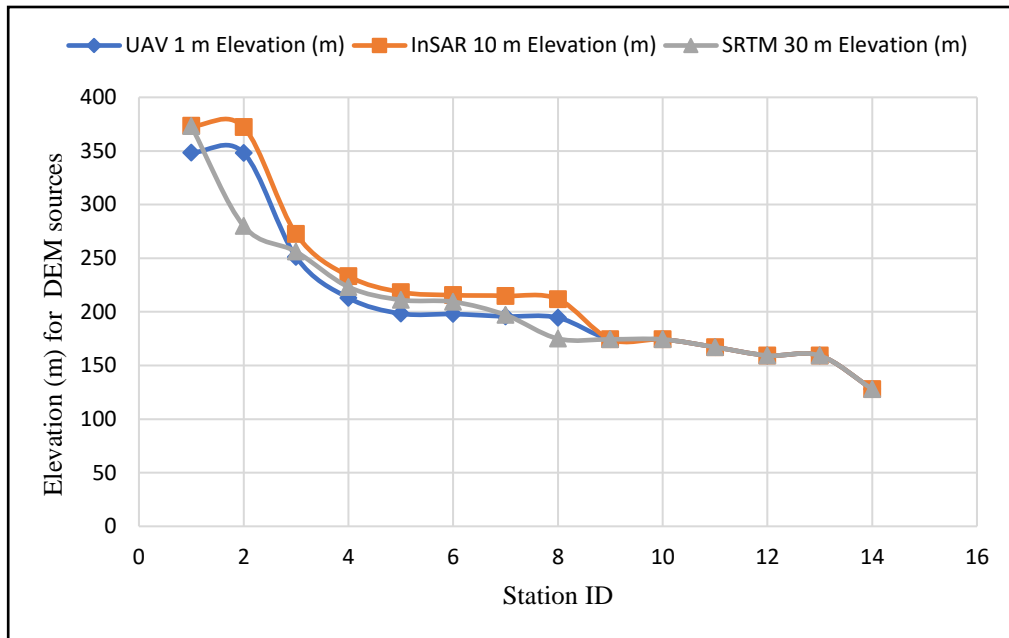
Figure 4.24c: Elevation of the selected nodes for the DEM sources
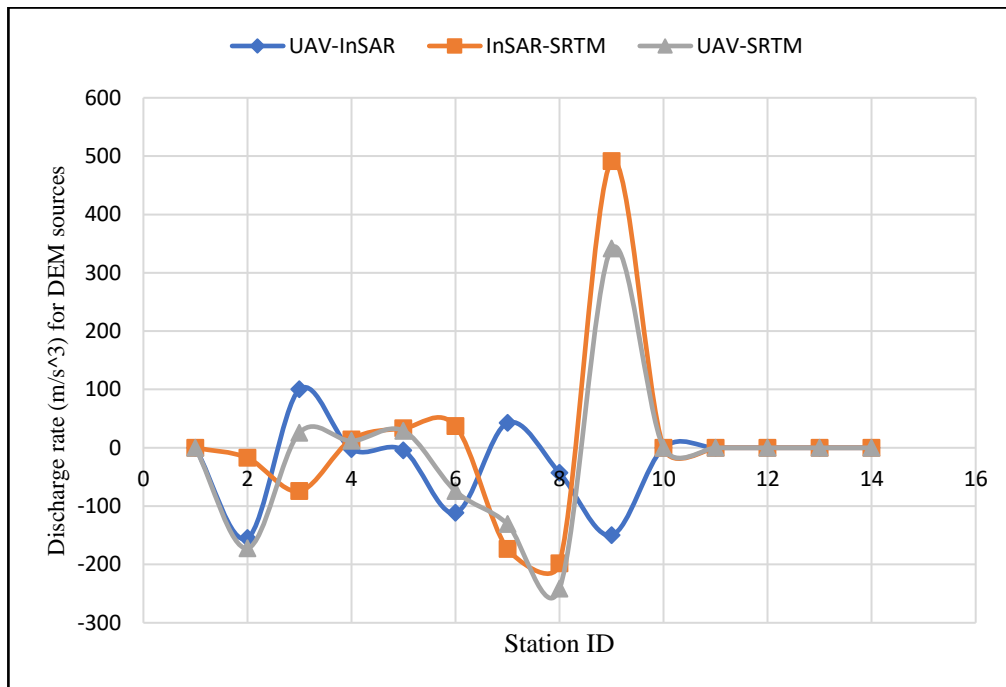
Figure 4.25a: Discharge rate difference between UAV, InSAR, and SRTM DEM
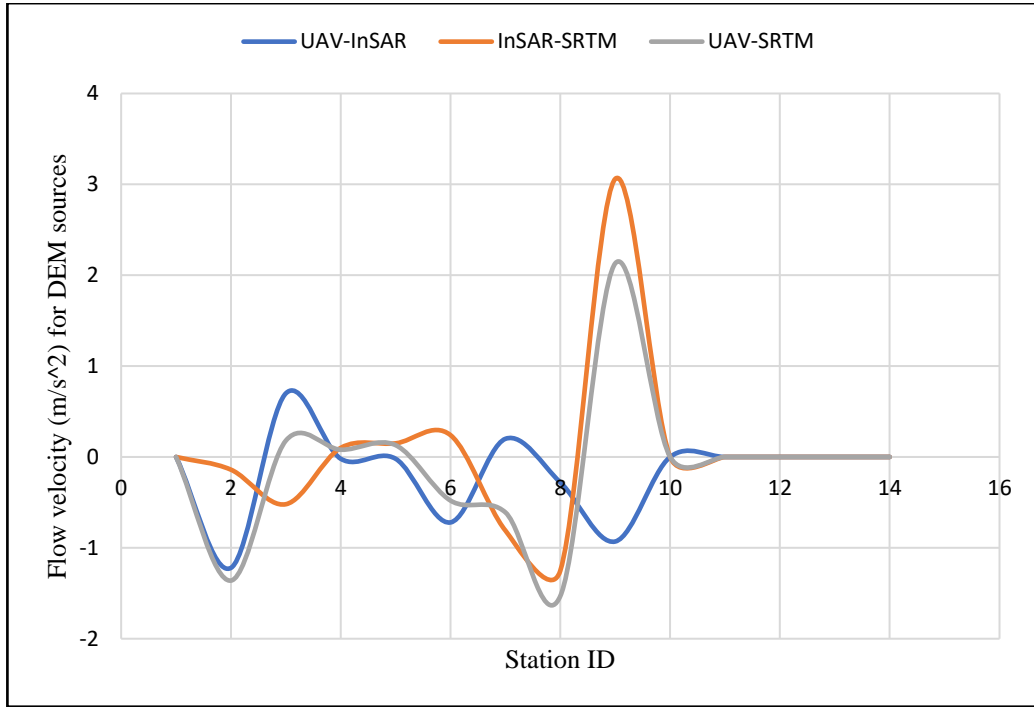
Figure 4.25b: Flow velocity difference between UAV, InSAR, and SRTM DEMs
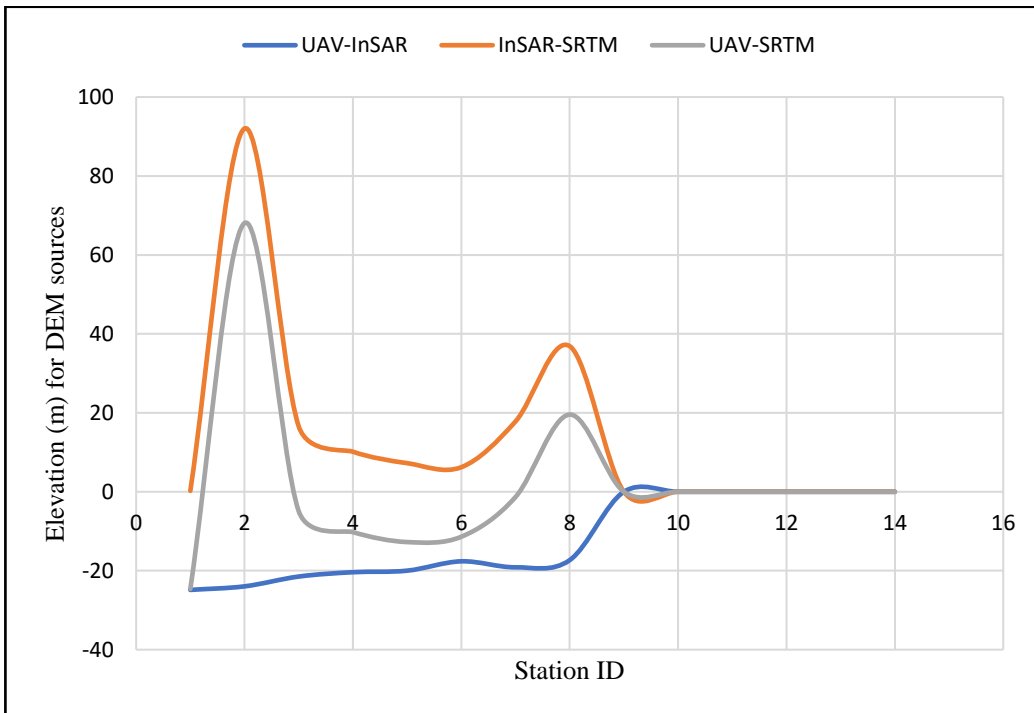
Figure 4.25c: Elevation difference between UAV, InSAR, and SRTM DEMs

4.9   Derived Flood-levels of the Study Area

Figure 4.26 shows the delineated catchment area and drainage basin from all three spatial resolution DEMs for the determination of the flood levels capable of inundating the studied floodplains (UAV–derived 1 m, InSAR 10 m, and 3SRTM 0 m). Tables 4.6-4.6a show the computed discharge and flow velocity at each node.

Figure 4.26: Delineated catchment area from different DEM sources

Table 4.6: Discharge rate and flow velocity using different DEMs source

Sta_ID	Settlement Name	UAV 1 m DEM			InSAR 10 m DEM			SRTM 30 m DEM		
		Elevation (m)	Discharge (m/s^3)	Velocity (m/s^2)	Elevation (m)	Discharge (m/s^3)	Velociy (m/s^2)	Elevation (m)	Discharge (m/s^3)	Velociy (m/s^2)
A01	Gidan Patuko	348.46	114.38	1.27	373.32	114.38	1.27	373.07	114.38	1.27
A02	Gidan Patuko	348.16	982.14	7.71	372.12	1137.03	8.93	280.09	1154.42	9.07
A03	Awolu Saga	251.16	244.82	1.71	272.64	144.72	1.01	256.09	219.00	1.53
A04	Sumaila	212.97	164.32	1.20	233.35	166.67	1.22	223.20	152.48	1.12
A05	Bere	198.36	322.99	1.48	218.35	327.25	1.50	211.10	293.92	1.35
A06	Tungan Gamba	197.93	71.75	0.46	215.55	183.46	1.18	209.33	146.16	0.94

Table 4.6a: Discharge rate and flow velocity using different DEMs source

Sta_ID	Settlements Name	UAV 1 m DEM			InSAR 10 m DEM			SRTM 30 m DEM		
		Elevation (m)	Discharge (m/s^3)	Velocity (m/s^2)	Elevation (m)	Discharge (m/s^3)	Velocity (m/s^2)	Elevation (m)	Discharge (m/s^3)	Velocity (m/s^2)
A07	Layi	195.72	96.68	0.45	214.86	53.80	0.25	197.05	227.45	1.06
A08	Nill	194.53	72.83	0.46	211.86	115.79	0.74	174.97	314.13	1.99
A09	Nill	174.39	411.48	2.56	174.39	561.24	3.49	174.39	69.90	0.43
A010	Nill	174.30	73.83	0.43	175.32	74.63	0.61	176.23	74.73	0.73
A011	Nill	167.08	161.14	0.91	167.08	161.14	0.91	167.08	161.14	0.91
A012	Nill	159.30	264.57	1.46	159.30	264.57	1.466	159.30	264.57	1.46
A013	Lawo Ravo	159.12	73.96	0.43	159.12	73.96	0.43	159.12	73.96	0.43
A014	Nill	128.00	343.64	1.72	128.00	343.64	1.72	128.00	343.64	1.72

The results presented in Figures 4.27 (a, b, and c) show the flood heights obtained for UAV-derived 1 m DEM, InSAR 10 m DEMs, and SRTM 30 m DEM that are capable of flooding the entire floodplain of Shiroro Dam and its environs. Figures 4.28 (a, b, and c) show the vulnerability map generated for the study through the flood heights simulated in the ArcScene environment to create a flood vulnerability graphical model for the study area.
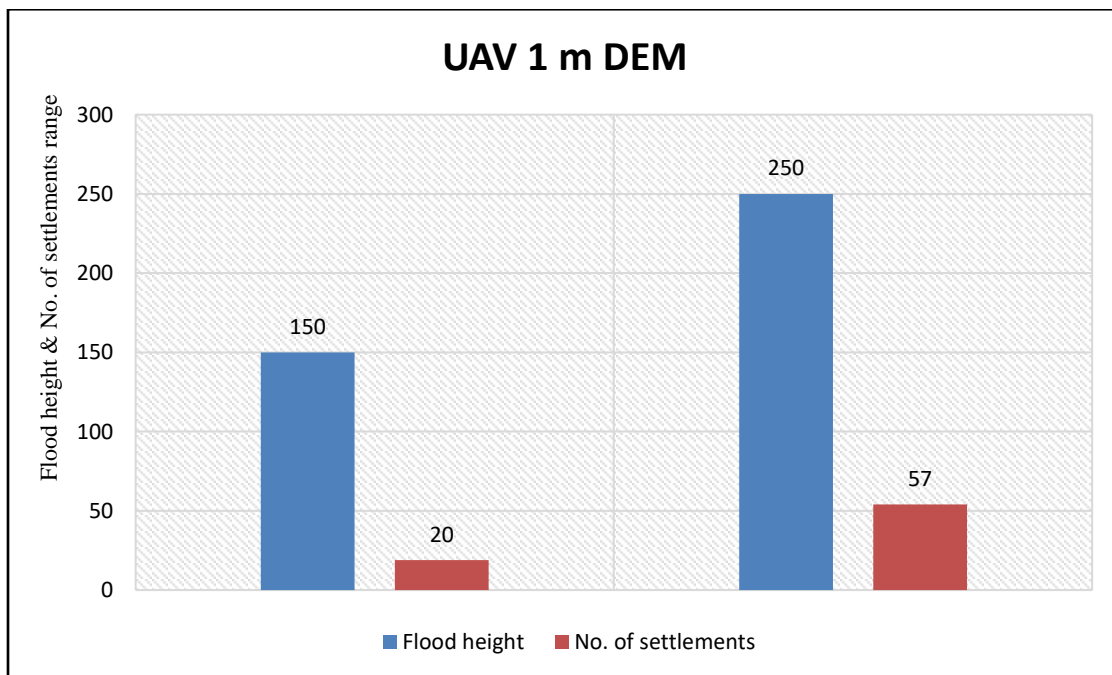
Figure 4.27a: Flood height based on UAV 1 m DEM at 150 m and 250 m
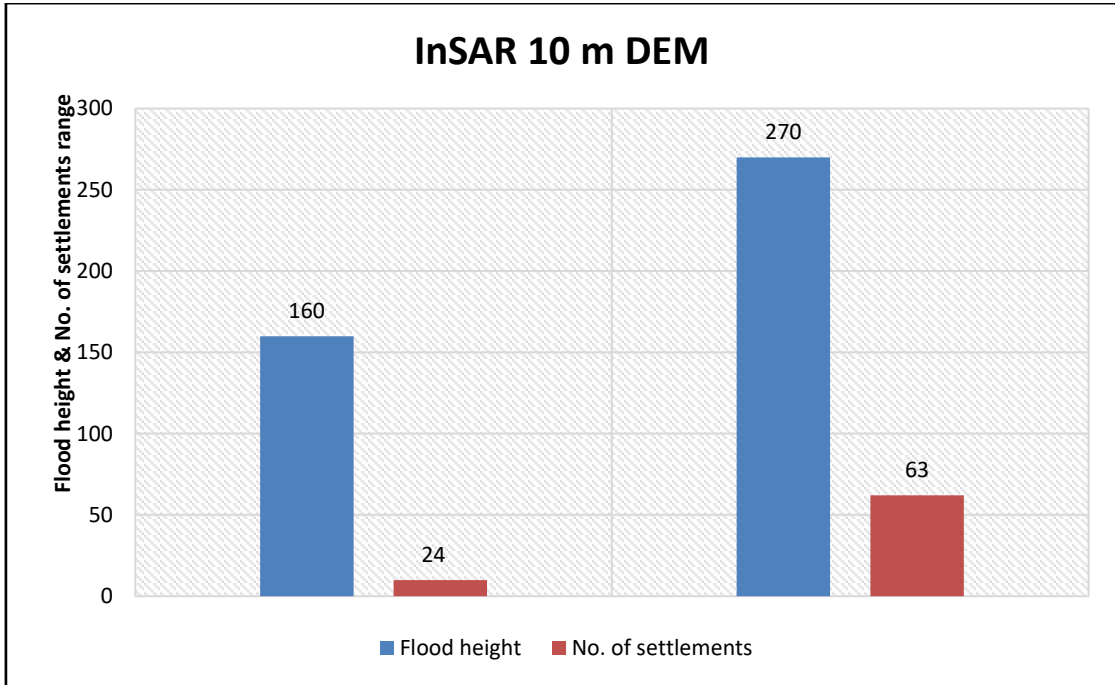
Figure 4.27b: Flood height of InSAR 10 m DEM based on 160 m and 270 m
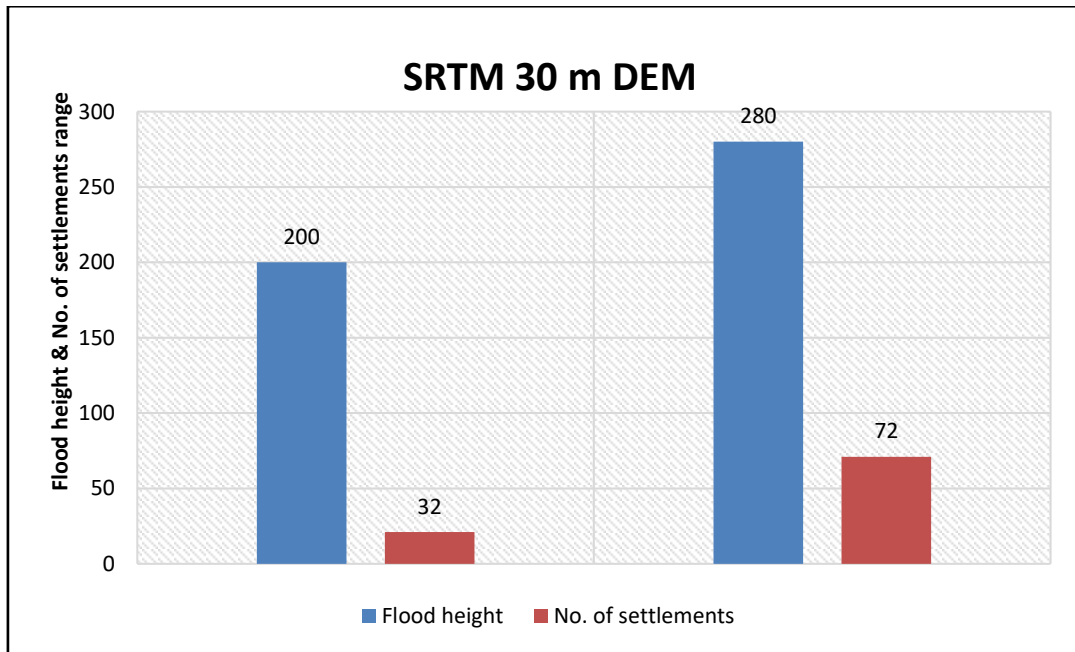
Figure 4.27c: Flood-heights of 30 m based on SRTM DEM at 200 m and 280 m
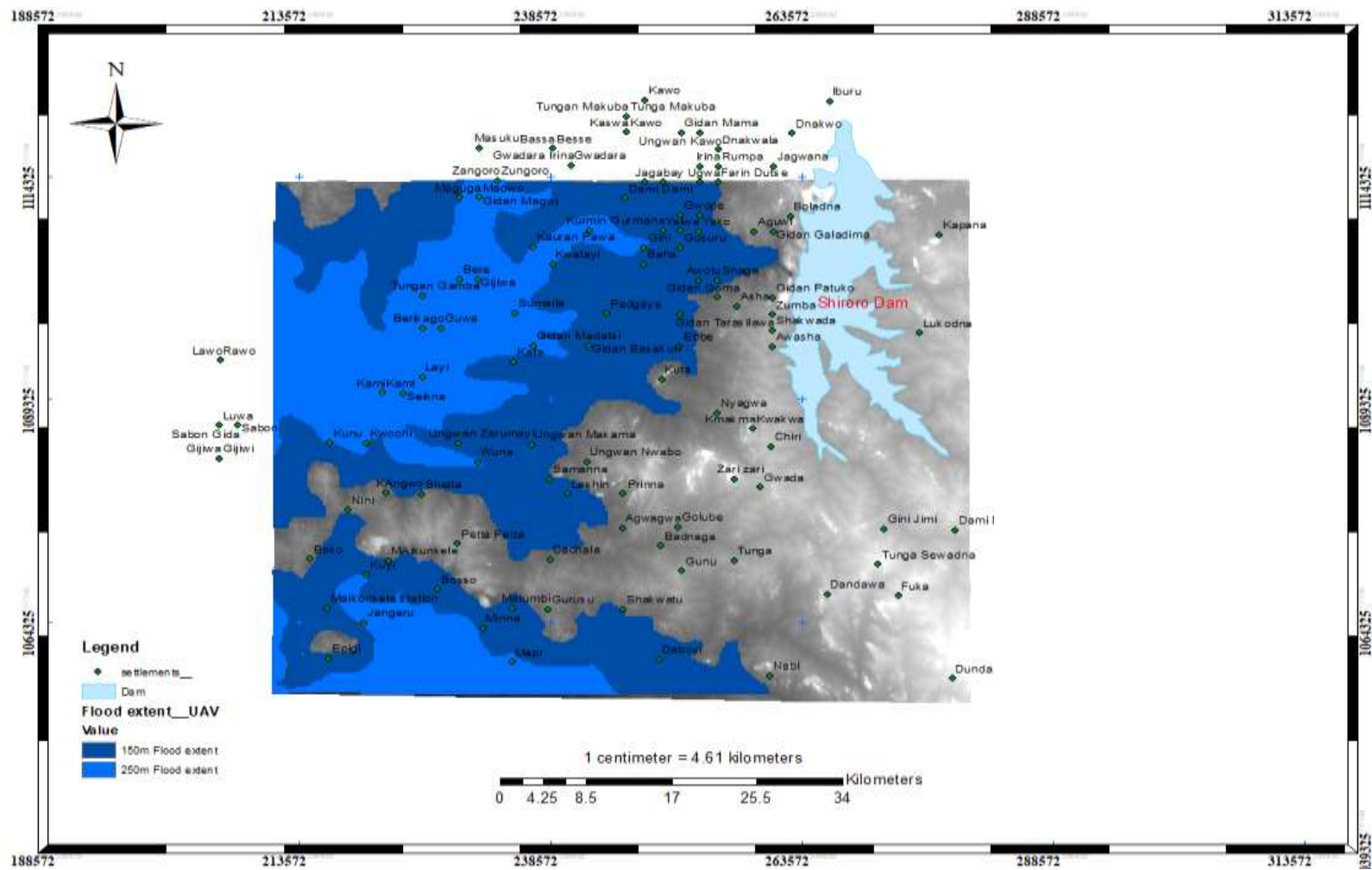
Figure 4.28a: UAV-derived 1 m DEM vulnerability flood extent
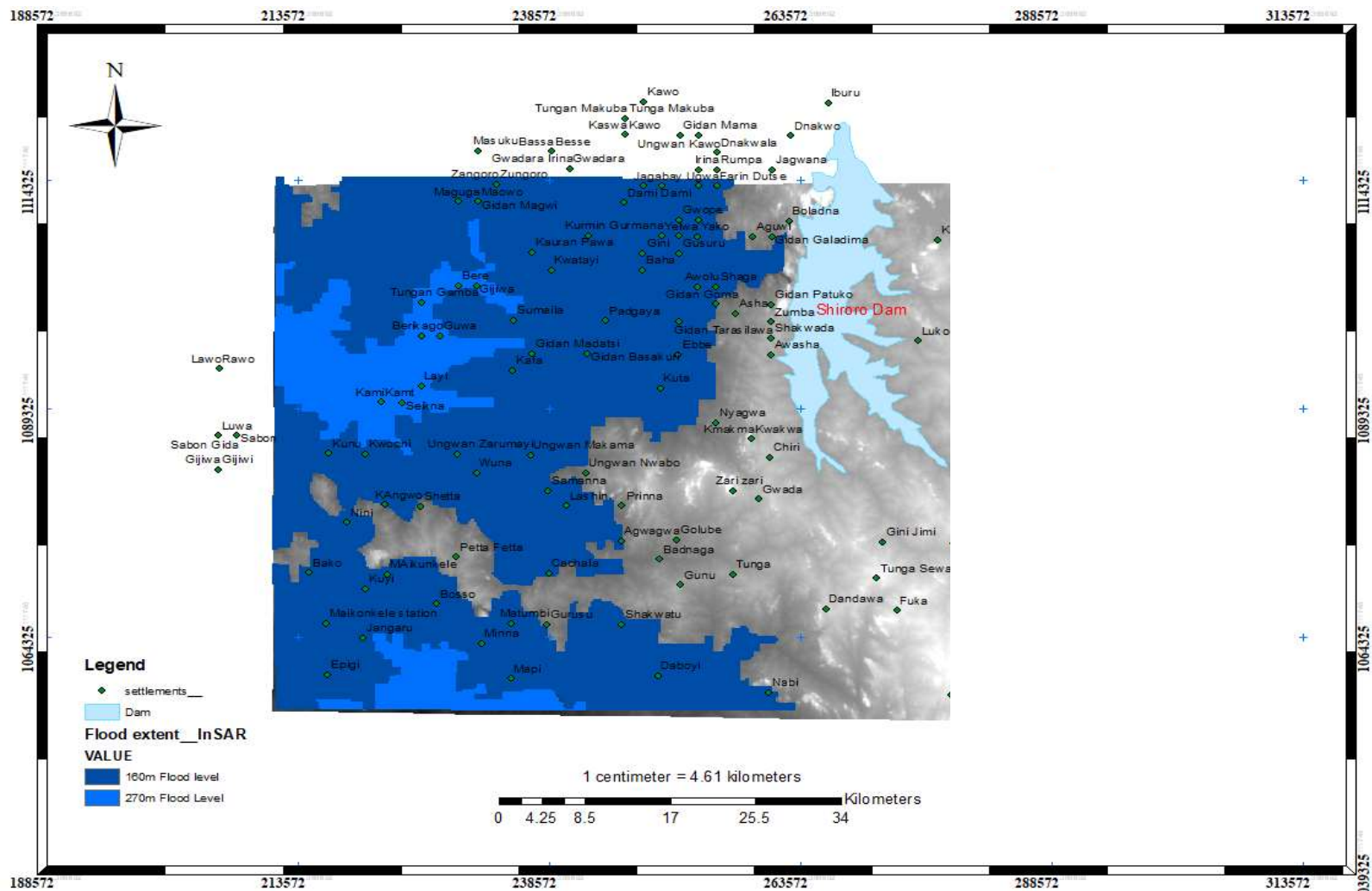
Figure 4.28b: InSAR 10 m DEM vulnerability flood extents
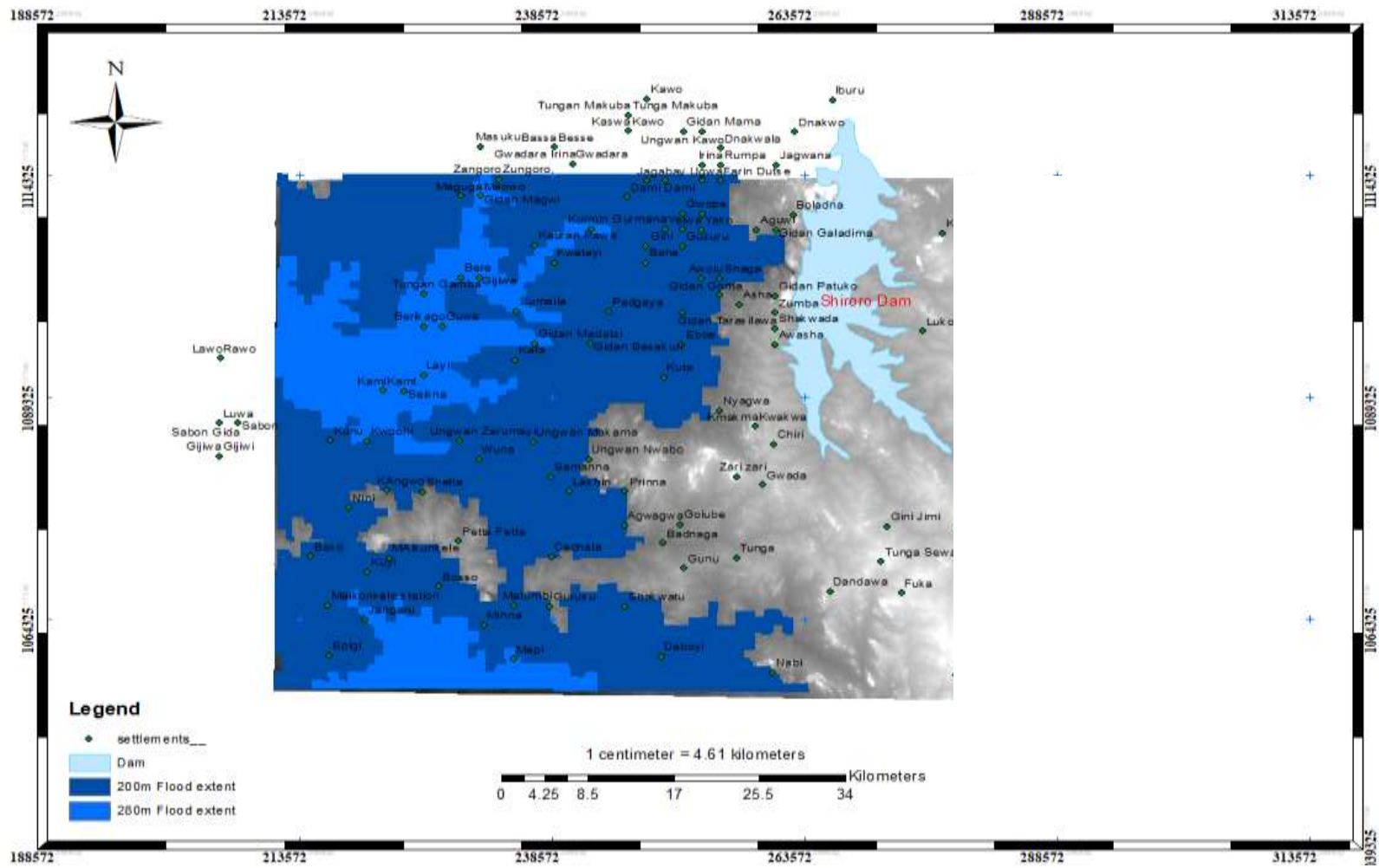
Figure 4.28c: SRTM 30 m DEM vulnerability flood extents

The flood heights and the number of settlements flooded are depicted in Table 4.7 using UAVs (1 m), InSAR (10 m), and SRTM (30 m). Figures 4.29 (a, b, and c) show the weighted overlay of flood-vulnerable areas from DEMs generated for the study area. Tables 4.8–4.8a, 4.9–4.9a, and 4.10–4.10a are the number and names of the settlements affected by the various flood levels, considering the DEMs used for the study.

Table 4.7: Number of flood- prone settlements using different DEMs sources

UAV 1 m DEM		InSAR 10 m DEM		SRTM 30 m DEM	
Flood heights	Vulnerable settlements	Flood heights	Vulnerable settlements	Flood heights	Vulnerable settlements
150 m	20	160 m	24	200 m	32
250 m	57	270 m	63	280 m	72
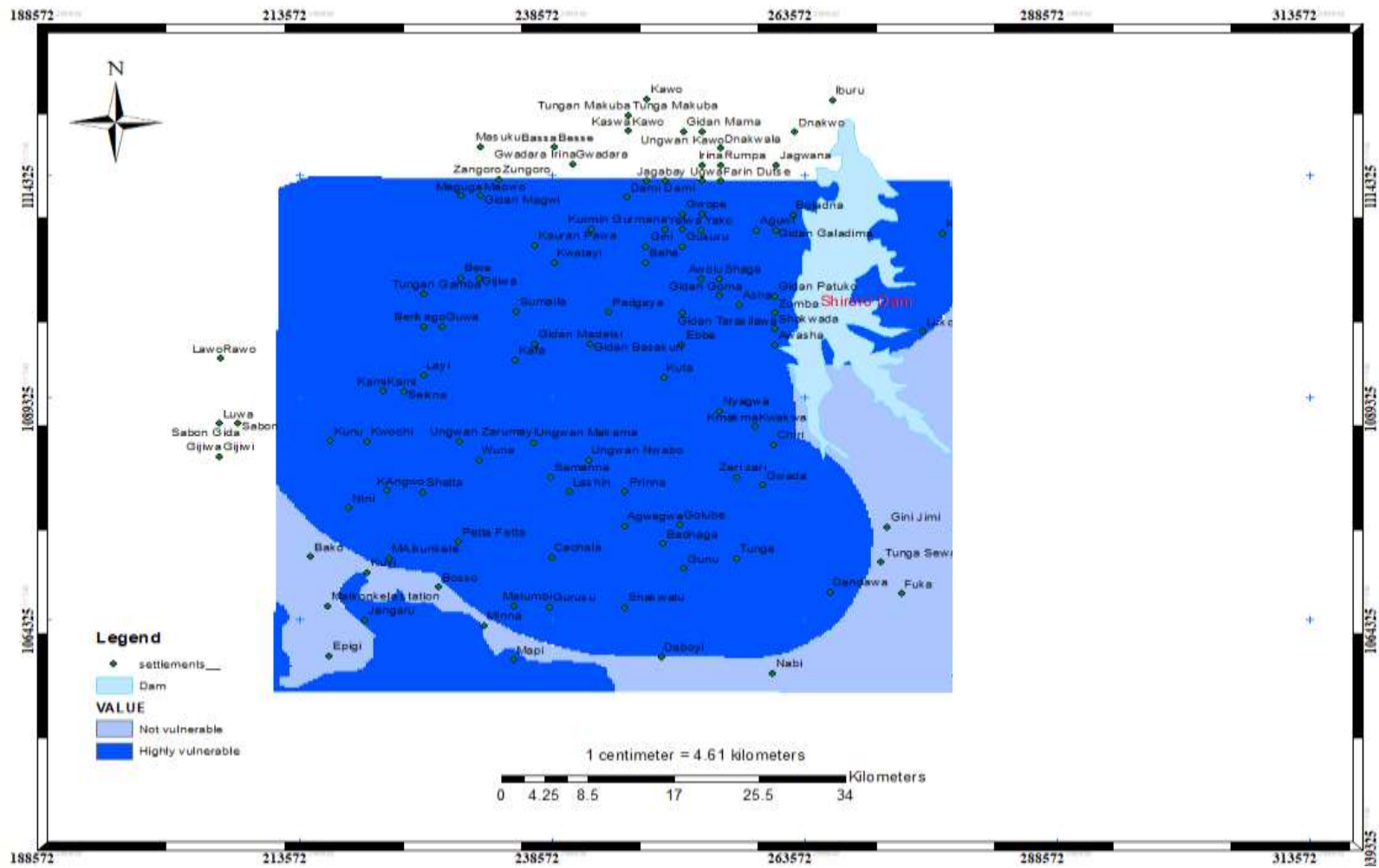
Figure 4.29a: Weighted overlay of flood vulnerable area from UAV DEM
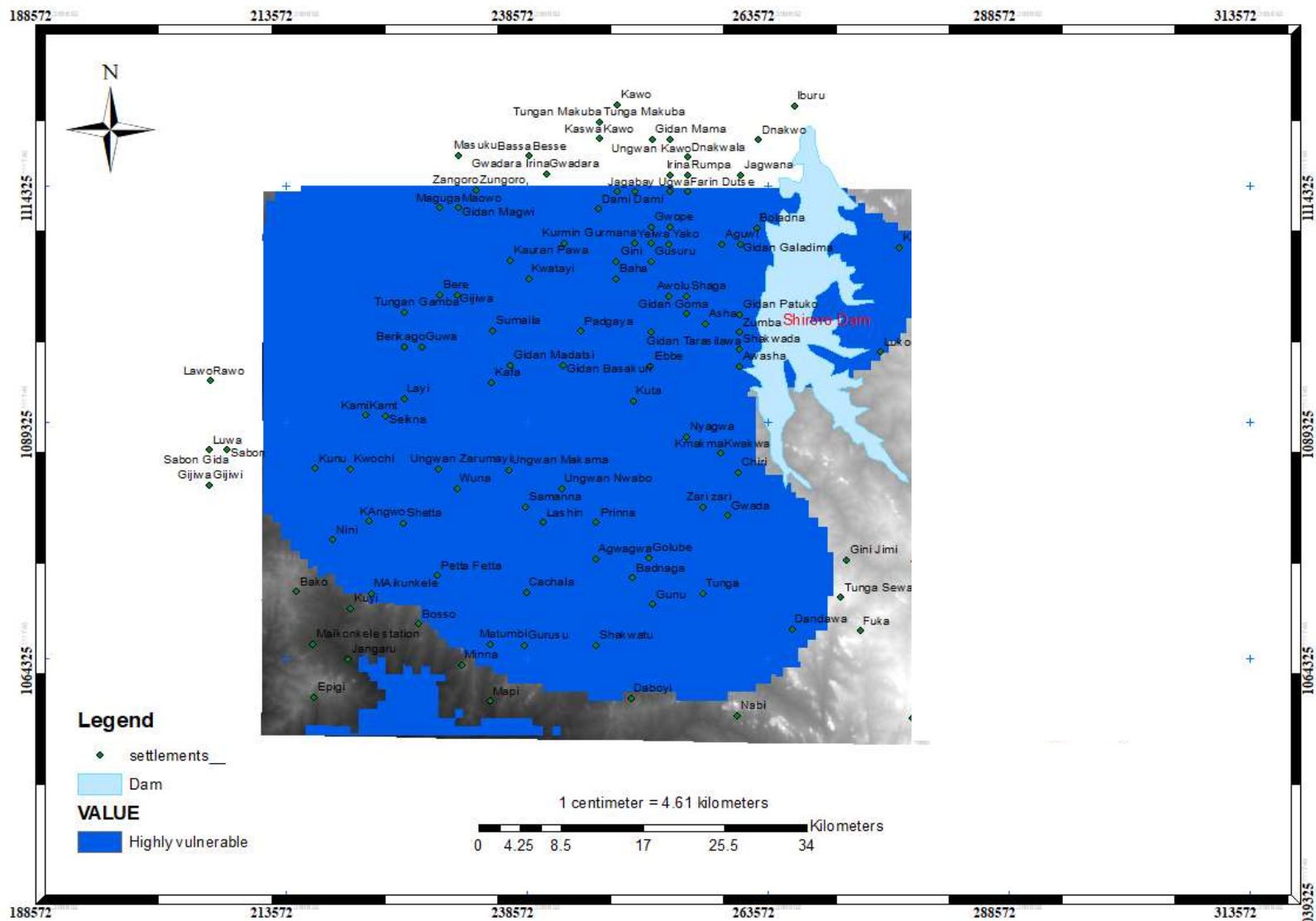
Figure 4.29b: Weighted overlay of flood vulnerable area from InSAR DEM
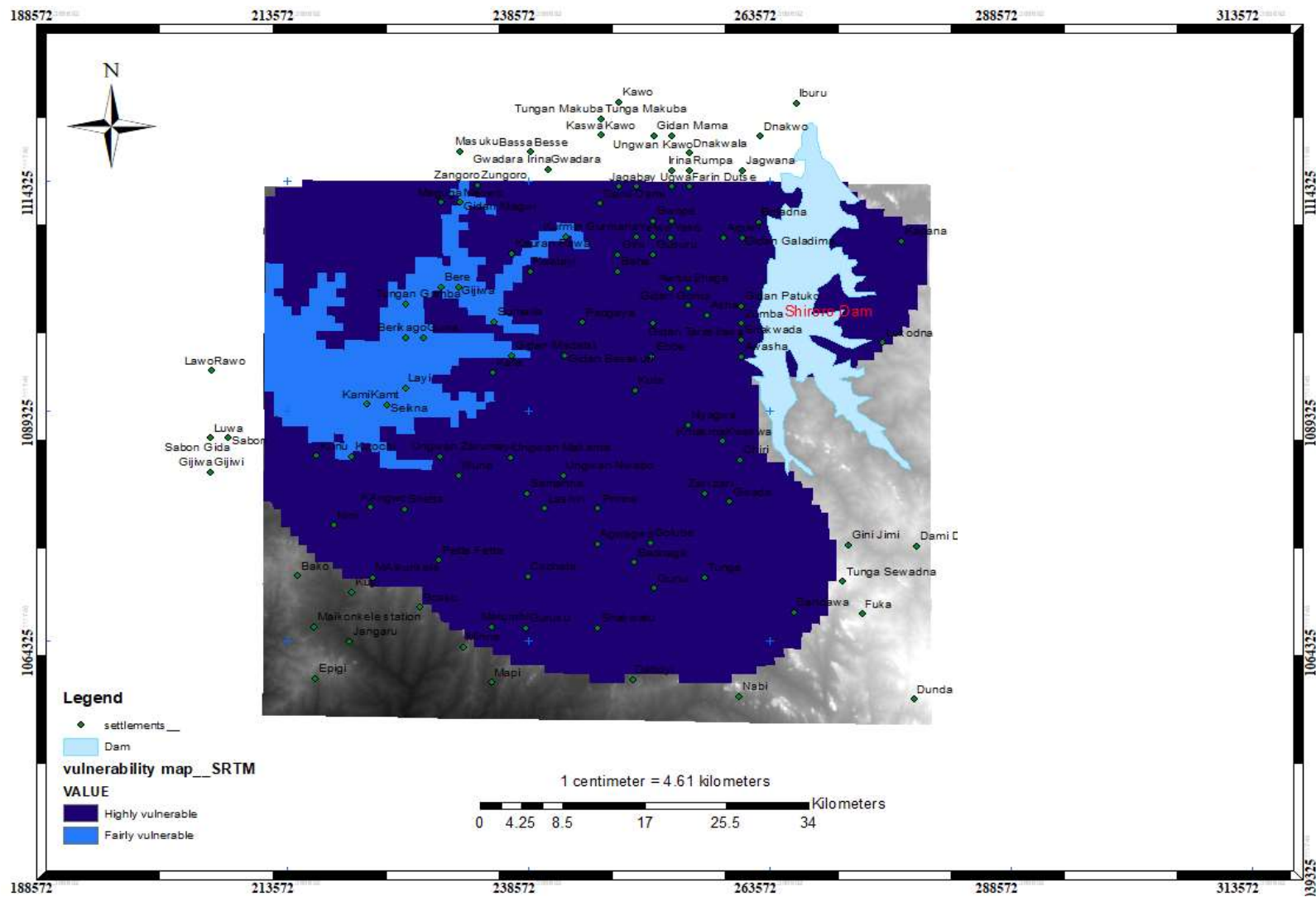
Figure 4.29c: Weighted overlay of flood vulnerable area from SRTM DEM

134

Table 4.8: Settlements vulnerable to inundation by UAV DEM

UAV 1 m DEM			
Flood height_150 m			
Vulnerable settlements			
Bere	Gidan Madatsi	Jangaru	Wuna
Samboro	Seikna	Layi	Baganakwo
Berikago	Jiko	Tungan	Shaluko Shalko
Guwa	Manta	Gijiwa	Mapi
Sumaila	KamiKamt	Kwochi	Numbupi

Table 4.8a: Settlements vulnerable to inundation by UAV DEM

UAV 1 m DEM											
Flood height_250 m											
Vulnerable settlements											
Bere	Gidan Madatsi	Jangaru	Wuna	Kwatayi	Gidan Tarasilawa	Ungwan	Maikunke	Kunu	Sumaila	KamiKamt	Kwochi
Samboro	Seikna	Layi	Baganakwo	Baha	Padgaya	Zarumayi Ungwan	Daboyi	Gijiwa	Gidan Madatsi	Jangaru	Numbupi
Berikago	Jiko	Tungan	shalukoShalko	Kafa	Awolu	Kuyi	Epigi	Samboro	Seikna	Mapi	Baganakwo shalukoShalko
Guwa	Manta	Gijiwa	Mapi	Gidan Basakuri	Shaga	Bosso	Matumbi	Berikago	Jiko	Tungan	
Sumaila	KamiKamt	Kwochi	Numbupi	Ebbe	Lashin	Minna	Samanna	Manta			

Table 4.9: Settlements vulnerable to inundation by InSAR DEM

InSAR 10 m DEM			
Flood height_160 m			
Vulnerable settllements			
Gidan Magwi	Bere	KamiKamt	Wuna
Samboro	Gijiwa	Seikna	Jangaru
Berikago	Sumaila	Gidan Madatsi	Baganakwo
Guwa	Jiko	Kwochi	Shaluko Shalko
Tungan Gamba	Manta	Layi	Numbupi
Mapi	Kurmin	Kakuri	Gini

Table 4.9a: Settlements vulnerable to inundation by InSAR DEM

InSAR 10 m DEM										
Flood height_270 m										
Vulnerable settlements										
Madaka Makuri	Gijiwa	Yako	Gidan Tarasilawa	Kwatayi	Ungwan Makama	Ungwan	Berikago	Bere	KamiKamt	Daboyi
Kakuri	Baha	Gwope	Ebbe	Baha	Lashin	Zarumayi Ungwan	Guwa	Gijiwa	Seikna	Epigi
Maguga	Gusuru	Awolu	Gidan Basakuri	Kafa	Samanna	Kuyi	Tungan Gamba	Sumaila	Gidan Madatsi	Tungan
Dami Dami	Gurmana	Shaga	Kafa	Gidan Basakuri	Bosso	Gidan Magwi	Mapi	Jiko	Kwochi	
Kwatayi	Yelwa	Padgaya	Ungwan Zarumayi	Ebbe	Minna	Samboro	Kurmin	Manta	Layi	
Kakuri	Gini	Wuna	Jangaru	Baganakwo	Shaluko Shalko	Numbupi	KamiKamt	Jangaru	Tungan	

Table 4.10: Settlements vulnerable to inundation by SRTM DEM

SRTM 30 m DEM				
Flood height_200 m				
Settlements name vulnerable				
Samboro	Layi	KamiKamt	Wuna	Madaka Makuri
Bere	Jiko	Seikna	Jangaru	Kakuri
Gijiwa	Manta	Gidan Madatsi	Baganakwo	Maguga
Tungan Gamba	KamiKamt	Kwochi	Shaluko Shalko	Dami Dami
Berikago	Seikna	Layi	Numbupi	Kwatayi
Guwa	Baganakwo	Kakuri	Gini	Kakuri
Gijiwa	Baha			

Table 4.10a: Settlements vulnerable to inundation by SRTM DEM

SRTM 30 m DEM											
Flood height_280 m											
Vulnerable settlements											
Madaka Makuri	Gijiwa	Yako	Gidan Tarasilawa	Kwatayi	Ungwan Makama	Ungwan	Berikago	Bere	KamiKamt	Daboyi	Maikunke
Kakuri	Baha	Gwope	Ebbe	Baha	Lashin	Zarumayi Ungwan	Guwa	Gijiwa	Seikna	Epigi	Samana
Maguga	Gusuru	Awolu	Gidan Basakuri	Kafa	Samanna	Kuyi	Tungan Gamba	Sumaila	Gidan Madatsi	Tungan	Prinna
Dami Dami	Gurmana	Shaga	Kafa	Gidan Basakuri	Bosso	Gidan Magwi	Mapi	Jiko	Kwochi	Berikago	Asha
Kwatayi	Yelwa	Padgaya	Ungwan Zarumayi	Ebbe	Minna	Samboro	Kurmin	Manta	Layi	Guwa	Mukama
Kakuri	Gini	Wuna	Jangaru	Baganakwo	Shaluko Shalko	Numbupi	KamiKamt	Jangaru	Tungan	Kunu	Nabi

4.10   Model Validation Results

Tables 4.11-4.11a, b; Tables 4.12-4.12a, b; and Tables 4.13-4.13a, b show the results of different DEM sources used for this study and the NSEMA (2021) results. Figure 4.30 presents the graphical representation of UAV-derived DEM 1 m conformity with the NESMA data and InSAR 10 m and SRTM 30 m DEMs produced higher estimate of the flood extent in the study area.

Table 4.11: Model validation results between UAV 1 m DEM and NSEMA data

UAV 1 m DEM				NSEMA 2021			
Flood height_150 m				**Low vulnerable**			
Vulnerable settlements				**Vulnerable settlements**			
Bere	Gidan Madatsi	Jangaru	Wuna	Bere	Gidan Madatsi	Jangaru	Wuna
Samboro	Seikna	Layi	Baganakwo	Samboro	Seikna	Layi	Baganakwo
Berikago	Jiko	Tungan	shalukoShalko	Berikago	Jiko	Tungan	shalukoShalko
Guwa	Manta	Gijiwa	Mapi	Guwa	Manta	Gijiwa	Mapi
Sumaila	KamiKamt	Kwochi	Numbupi	Sumaila	KamiKamt	Kwochi	Numbupi

Table 4.11a: Model validation results between UAV 1 m DEM and NSEMA data

UAV 1 m DEM											
Flood height_250 m											
Vulnerable settlements											
Bere	Gidan Madatsi	Jangaru	Wuna	Kwatayi	Gidan Tarasilawa	Ungwan	Maikunke	Kunu	Sumaila	KamiKamt	Kwochi
Samboro	Seikna	Layi	Baganakwo	Baha	Padgaya	Zarumayi Ungwan	Daboyi	Gijiwa	Gidan Madatsi	Jangaru	Numbupi
Berikago	Jiko	Tungan	shalukoShalko	Kafa	Awolu	Kuyi	Epigi	Samboro	Seikna	Mapi	Baganakwo
Guwa	Manta	Gijiwa	Mapi	Gidan Basakuri	Shaga	Bosso	Matumbi	Berikago	Jiko	Tungan	shalukoShalko
Sumaila	KamiKamt	Kwochi	Numbupi	Ebbe	Lashin	Minna	Samanna	Manta			

Table 11b: Model validation results between UAV 1 m DEM and NSEMA data

						NSEMA 2021					
						High vulnerable					
						Vulnerable settlements					
Bere	Gidan Madatsi	Jangaru	Wuna	Kwatayi	Gidan Tarasilawa	Ungwan	Maikunke	Kunu	Sumaila	KamiKamt	Kwochi
Samboro	Seikna	Layi	Baganakwo	Baha	Padgaya	Zarumayi Ungwan	Daboyi	Gijiwa	Gidan Madatsi	Jangaru	Numbupi
Berikago	Jiko	Tungan	shalukoShalko	Kafa	Awolu	Kuyi	Epigi	Samboro	Seikna	Mapi	Baganakwo
Guwa	Manta	Gijiwa	Mapi	Gidan Basakuri	Shaga	Bosso	Matumbi	Berikago	Jiko	Tungan	shalukoShalko
Sumaila	KamiKamt	Kwochi	Numbupi	Ebbe	Lashin	Minna	Samanna	Manta			

Table 4.12: Model validation results between InSAR 10 m DEM and NSEMA data

InSAR 10 m DEM				NSEMA 2021			
Flood height_160 m				Low vulnerable			
Vulnerable settlements				Vulnerable settlements			
Gidan Magwi	Bere	KamiKamt	Wuna	Bere	Gidan Madatsi	Jangaru	Wuna
Samboro	Gijiwa	Seikna	Jangaru	Samboro	Seikna	Layi	Baganakwo
Berikago	Sumaila	Gidan Madatsi	Baganakwo	Berikago	Jiko	Tungan	shalukoShalko
Guwa	Jiko	Kwochi	Shaluko Shalko	Guwa	Manta	Gijiwa	Mapi
Tungan Gamba	Manta	Layi	Numbupi	Sumaila	KamiKamt	Kwochi	Numbupi
Mapi	Kurmin	Kakuri	Gini				

Table 4.12a: Model validation results between InSAR 10 m DEM and NSEMA data

InSAR 10 m DEM										
Flood height_270 m										
Vulnerable settlements										
Madaka Makuri	Gijiwa	Yako	Gidan Tarasilawa	Kwatayi	Ungwan Makama	Ungwan	Berikago	Bere	KamiKamt	Daboyi
Kakuri	Baha	Gwope	Ebbe	Baha	Lashin	Zarumayi Ungwan	Guwa	Gijiwa	Seikna	Epigi
Maguga	Gusuru	Awolu	Gidan Basakuri	Kafa	Samanna	Kuyi	Tungan Gamba	Sumaila	Gidan Madatsi	Tungan
Dami Dami	Gurmana	Shaga	Kafa	Gidan Basakuri	Bosso	Gidan Magwi	Mapi	Jiko	Kwochi	
Kwatayi	Yelwa	Padgaya	Ungwan Zarumayi	Ebbe	Minna	Samboro	Kurmin	Manta	Layi	
Kakuri	Gini	Wuna	Jangaru	Baganakwo	Shaluko Shalko	Numbupi	KamiKamt	Jangaru	Tungan	

Table 4.12b: Model validation results between InSAR 30 m DEM and NSEMA data

NSEMA 2021											
High vulnerable											
Vulnerable settlements											
Bere	Gidan Madatsi	Jangaru	Wuna	Kwatayi	Gidan Tarasilawa	Ungwan	Maikunke	Kunu	Sumaila	KamiKamt	Kwochi
Samboro	Seikna	Layi	Baganakwo	Baha	Padgaya	Zarumayi Ungwan	Daboyi	Gijiwa	Gidan Madatsi	Jangaru	Numbupi
Berikago	Jiko	Tungan	shalukoShalko	Kafa	Awolu	Kuyi	Epigi	Samboro	Seikna	Mapi	Baganakwo
Guwa	Manta	Gijiwa	Mapi	Gidan Basakuri	Shaga	Bosso	Matumbi	Berikago	Jiko	Tungan	shalukoShalko
Sumaila	KamiKamt	Kwochi	Numbupi	Ebbe	Lashin	Minna	Samanna	Manta			

Table 4.13: Model validation results between SRTM 30 m DEM and NSEMA data

SRTM 30 m DEM Flood height_200 m Settlements name vulnerable					NSEMA 2021 Low Vulnerable Settlements name vulnerable			
Samboro	Layi	KamiKamt	Wuna	Madaka Makuri	Bere	Gidan Madatsi	Jangaru	Wuna
Bere	Jiko	Seikna	Jangaru	Kakuri	Samboro	Seikna	Layi	Baganakwo
Gijiwa	Manta	Gidan Madatsi	Baganakwo	Maguga	Berikago	Jiko	Tungan	shalukoShalko
Tungan Gamba	KamiKamt	Kwochi	Shaluko Shalko	Dami Dami	Guwa	Manta	Gijiwa	Mapi
Berikago	Seikna	Layi	Numbupi	Kwatayi	Sumaila	KamiKamt	Kwochi	Numbupi
Guwa	Baganakwo	Kakuri	Gini	Kakuri				

Table 4.13a: Model validation results between SRTM 30 m DEM and NSEMA data

SRTM 30 m DEM

Flood height_280 m

Vulnerable settlements

Madaka Makuri	Gijiwa	Yako	Gidan Tarasilawa	Kwatayi	Ungwan Makama	Ungwan	Berikago	Bere	KamiKamt	Daboyi	Maikunke
Kakuri	Baha	Gwope	Ebbe	Baha	Lashin	Zarumayi Ungwan	Guwa	Gijiwa	Seikna	Epigi	Samana
Maguga	Gusuru	Awolu	Gidan Basakuri	Kafa	Samanna	Kuyi	Tungan Gamba	Sumaila	Gidan Madatsi	Tungan	Prinna
Dami Dami	Gurmana	Shaga	Kafa	Gidan Basakuri	Bosso	Gidan Magwi	Mapi	Jiko	Kwochi	Berikago	Asha
Kwatayi	Yelwa	Padgaya	Ungwan Zarumayi	Ebbe	Minna	Samboro	Kurmin	Manta	Layi	Guwa	Mukama
Kakuri	Gini	Wuna	Jangaru	Baganakwo	Shaluko Shalko	Numbupi	KamiKamt	Jangaru	Tungan	Kunu	Nabi

Table 4.13b: Model validation results between SRTM 30 m DEM and NSEMA data

						NSEMA 2021						
						High vulnerable						
						Vulnerable settlements						
Bere	Gidan Madatsi	Jangaru	Wuna	Kwatayi	Gidan Tarasilawa	Ungwan	Maikunke	Kunu	Sumaila	KamiKamt	Kwochi
Samboro	Seikna	Layi	Baganakwo	Baha	Padgaya	Zarumayi Ungwan	Daboyi	Gijiwa	Gidan Madatsi	Jangaru	Numbupi
Berikago	Jiko	Tungan	shalukoShalko	Kafa	Awolu	Kuyi	Epigi	Samboro	Seikna	Mapi	Baganakwo
Guwa	Manta	Gijiwa	Mapi	Gidan Basakuri	Shaga	Bosso	Matumbi	Berikago	Jiko	Tungan	shalukoShalko
Sumaila	KamiKamt	Kwochi	Numbupi	Ebbe	Lashin	Minna	Samanna	Manta			

Figure 4.30: UAV-derived DEM 1 m conformity with NSEMA 2021 data

4.11 Discussion of Results

4.11.1 Hydrological data presentation discussion of results

Figure 4.1 shows that from May to October, there was an increase in rainfall, which also increased the volume of water in the dam reservoir. Likewise, with no rain between January and April, there needed to be more rainfall to fill the dam reservoir. Figure 4.2 shows months when there is less inflow into the dam reservoir, from January to May, and when there is an increased inflow into the reservoir, from June to October. Based on this information, the inflow data helped to know the months when there is more or less inflow to the dam reservoir. Figure 4.3 shows that the temperature from January to April increases and begins decreasing from May to August.

By indication, when the temperature is low, the water in the dam reservoir increases. Figure 4.4 shows the water level in the dam reservoir that increased from July to September and started diminishing in October. These indicate the months when the water level in the dam reservoir is high. Figure 4.5 shows an increase in outflow from July to

September, which is high in those months, which is the contributing factor leading to water released downstream when it is over the bank to flood the downstream.

4.11.2 Hydrological data correlation discussion of results

Figure 4.6 shows that rainfall significantly contributed to the increase in the amount of water in the dam reservoir, which causes the water surface level of the dam to increase (i.e., an increase in rainfall causes an increase in the water surface level of the dam reservoir). Similarly, from July to September, the amount of rainfall significantly increased. Hence, rainfall is the factor in the hydrological data that contributed to the flooding along the Shiroro floodplain.

Figure 4.7 shows the graphical representation of the two data sets. Looking at the chart, from April to September, the inflow into the dam reservoir increased more than the amount of rainfall. Whether there is rainfall or not, water goes into the dam reservoir from the upstream Kaduna River. As a result, it increased the water level in the dam reservoir. Thus, the inflow is one of the hydrological factors that contributed to the increase of water in the dam reservoir, which overflows its banks, causing the release of the deluge to the downstream communities by the dam authorities.

The correlation between the inflow discharge and water elevation in the study under investigation is shown in Figure 4.8, which shows that when the amount of inflow entering the dam reservoir is higher, the water level in the dam reservoir increases. Figure 4.9 shows that storage increases when peak inflow occurs and continues until the outflow rises to equal the receding inflow. At this time, the flood crest occupies a position in the reach. The amount of water is higher from July to September, and the low temperature is also observed in the same months, as shown in Figure 4.10. The low temperatures increased the dam reservoir's water level.

Thus, the correlation of the various plots reveals the following relationships, validating the authenticity of the hydrological dataset: (i) As rainfall increases over the months, the water level in the reservoir is also on the rise (ii) Similarly, the inflow and water level elevation also respond positively to increased rainfall and vice versa. It shows that the perennial flooding event witnessed in the floodplain could result in changing hydrological patterns in the study area, which resulted in the opening and closing of the spillway gate (iii). In contrast, high temperatures are associated with low rainfall.

The correlation between various datasets shows that the hydrological data is the contributing factor to the annual flooding downstream of the dam (Adesina *et al.,* 2022), which is caused by the Shiroro Dam authorities opening the spillway gates to release excess water from the dam reservoir whenever it overflows its bank.

4.11.3 Bathymetry data presentation discussion of results

The river channel bathymetry in Table 4.1 was used with DEM sources and SWE (MATLAB) to compute discharge volume, discharge rate, and flow velocity for two flood level (low and high) comparisons.

4.11.4 NSEMA damaged assessment data presentation discussion of results

The NSEMA data validated the study and confirmed that the three DEMs (UAV-derived 1 m, InSAR 10 m, and SRTM 30 m) perform differently in modelling floods in the study area shown in Figure 4.30.

4.11.5 Comparative assessment of the DEM sources discussion of results

A visual examination of the three different DEM sources generated indicates similarities in the patterns of the DEM produced (Figures 4.15 a, b, and c). It shows that the data sources have some form of consistency with each other within the study area and, as such,

allow for some form of "replaceability" between them. However, DEM statistics (Table 4.1) show that all three DEMs have striking data differences that are large enough to cause a significant difference in the results obtained from their analyses.

The descriptive statistics of the data reveal that the UAV data has the lowest absolute values (156.527 m) compared to others (173.031 m and 177.110 m for the InSAR and SRTM DEMs, respectively). It is clear that the InSAR and SRTM maximum and minimum height values (635.599 m, 665.032 m, and 173.031 m, 177.110 m, respectively) appear to be more consistent with themselves than the values obtained from the UAV, some of the reasons for this trend, as observed, are:

i.   Both InSAR and SRTM DEMs have the same vertical reference surface, which is the WGS 84 ellipsoid used as a reference ellipsoid for the Sentinel and SAR satellites for data collection (Nwilo *et al.,* 2012).

ii.   Aside from their ground sampling distance (GSD) or spatial resolution, the other difference between both data generation sources is the radar band used in the payloads of each of the satellites. While the Sentinel satellite carries a C-band-enabled payload, the SRTM twin-SAR satellites carry X-band-enabled payloads (Farr *et al.,* 2007; Foni and Seal, 2004; Rabus *et al.,* 2003).

iii.   Since the X-band has limited material penetrative power compared to the C-band, the SRTM DEM is more of a surface model than a terrain model (Farr *et al.,* 2007), wherein the radar pulses are reflected by foliage (in forested areas), building components (in built-up areas), and vehicle tops. Although the C-band does not penetrate all terrain materials, it does pass through foliage and may return to the tree's trunk.

iv.   Invariably, the InSAR and SRTM DEMs are surface models, not terrain models (Dowman and Michalis, 2004). For this reason, it is scientifically consistent if the InSAR

and SRTM DEM's absolute heights are higher in value than the UAV data set. The InSAR and SRTM data do not reach the terrain surface; instead, the radar pulses generating the measurements are reflected from tree trunks and foliage, respectively.

In addition, considering the statistical parameter differences between the three DEM datasets, the DEM with the highest range is the SRTM at 30 m, followed by InSAR at 10 m and UAV at 1 m. UAV has the lowest standard deviation, which shows a more accurate representation of its accuracy. It could be inferred from the graph in Figure 4.16 that, in terms of descriptive statistics, the InSAR is a better representation of the study relative to the UAV, which is considered the measure of accuracy.

Based on the facts presented in items 1 – 4 of this section, it is clear that the UAV data is the most precise among all three (3) tested data sources. For this reason, the UAV-derived DEM, which has a spatial resolution of 1 m, was chosen as the control data set for this work, to which all other DEMs are correlated. Comparing the UAV data with InSAR and SRTM data yielded root mean square errors (RMSE) of 0.249 m, 0.352 m, and 0.455 m, respectively. It further confirms that the UAV data outperforms the InSAR and SRTM data. For this reason, it is also scientifically acceptable to state that the InSAR-derived DEM is next in accuracy to the UAV-derived DEM, and SRTM DEM has the lowest precision and accuracy notwithstanding, analysis of the variances (ANOVA) between UAV, InSAR, and SRTM data using a single-factor analysis carried out. Going by the result of the test as presented in Tables 4.2 and 4.2a, although the ANOVA test performed on the three DEM sources indicates statistically low significance with an F-critical (2.996), it is lower than the expected F-table value for 10,000 points (394.722) at a 95% confidence interval. The correlation analysis in Table 4.3 backs up the results in Tables

4.2 (a, b). There is a correlation between the three different data sets; a positive correlation (0.9996) between the InSAR DEM and the SRTM and UAV-derived DEMs.

4.11.6 Implications of the DEM on hydrological analysis of the study area discussion of results

Figures 4.17- 4.19 show the flow direction map, while Figure 4.20 flow accumulation and surface runoff generated from all three DEMs. The river watersheds derived from the selected DEMs differ significantly (Figures 4.21– 4.23). It shows the differences in the floodable areas of the used DEM obtained.

Table 4.4 further shows that the accuracy of the DEM plays a significant role in generating flood inundation maps by adequately presenting the topographic data of the river and the floodplain. Additionally, the quality of DEM-derived hydrological features is sensitive to the DEM's accuracy and resolution. There are differences between the elevation values derived from high-resolution UAV-derived DEMs and low-resolution InSAR-derived and SRTM DEMs. Watershed boundaries derived from these three DEM sources are also quite different (Figures 4.21- 4.23). The higher accuracy of the UAV-derived DEM gave a more detailed delineation of watersheds. The results indicate that the UAV-derived DEM with high resolution offers the capability of improving the quality of hydrological features extracted from DEMs. Thus, higher-resolution DEMs provide more reliable maps of flood simulations.

4.11.7 Implications of the DEM on hydraulic analysis of the study area discussion of results

Considering the discharge difference from UAV-derived 1 m, InSAR 10 m, and SRTM 30 m DEMs, the analysis of the differences shows that the InSAR data shows a close relationship with the UAV data in a few locations, such as A02, A04, A05, A07, A08,

and A09, as seen in the differences in Appendix B3. It is more precise than the difference observed between UAV and SRTM. Details of this analysis are in Figure 4.24a. The root mean square error (RMSE) for UAV-InSAR is 72.0248, and that of UAV-SRTM is 127.859; this shows that InSAR gives a closer difference in discharge value concerning UAV than SRTM.

Also, an analysis of the differences in flow velocity is in Table 4.5-4.5a for UAV-derived 1 m, InSAR 10 m, and SRTM 30 m DEMs, respectively. InSAR gives a more precise difference in the discharge velocity compared to SRTM using UAV as a reference. The chart in Figure 4.24b represents the variation in the discharge velocity derived from these datasets. The settlement with code A09 has the highest velocity range, and the same case for the discharge rate in Appendix B4.

The analysis of the root mean square error (RMSE) for UAV-InSAR is 0.49863, and that of UAV-SRTM is 0.81878; this shows that InSAR gives a closer difference in velocity value concerning UAV than SRTM. Appendix B5 shows the analysis of the difference in the parameter elevation for the DEM datasets, and Figure 4.24c shows the variation in the charts. The root mean square error (RMSE) for UAV-InSAR DEMs is 15.688, and that of UAV-SRTM DEMs is 20.7791; this shows that InSAR DEM gives a closer difference in elevation value concerning UAV DEM than SRTM DEM.

4.11.8 Derived flood levels of the study area discussion of results

The discharge values obtained at nodes in Tables 4.5 -4.5a for the used DEMs show the flood heights where the inundation occurred in the study area and its environs. The results presented in Figures 4.27 (a, b, and c) show the flood heights obtained for UAV-derived 1 m DEM, InSAR 10 m DEMs, and SRTM 30 m DEM capable of flooding the entire floodplain of Shiroro Dam and its environs. Then, the simulated flood heights in the

ArcScene environment created a flood vulnerability graphical model for the study area, shown in Figures 4.28 (a, b, and c).

According to Figure 4.27a, twenty (20) settlements were affected at a flood height of 150 m and Fifty-seven (57) settlements at 250 m from 1 m UAV-derived DEM. Twenty-four at the flood height of 160 m and sixty-three (63) were affected by flood at the flood height of 270 m, according to Figure 4.27b, the InSAR 10 m DEM. Figure 4.27c, the SRTM 30 m DEM shows the number of settlements affected at various flood heights: 32 and 72 at 200 m and 280 m, respectively. However, as shown in Figures 4.28 (a, b, and c), the vulnerability map was generated for the study. The map of the DEMs used at different flood levels shows the coverage areas where the volume of water (outflow) flooded when the dam authorities opened the spillway gate when the dam reservoir overflowed its bank.

The overlay map shows areas' potential for flooding in the study area. Based on Figures 4.29 (a, b, and c) show the settlements in the Shiroro downstream in the flood vulnerability category. This area has a contour that tends to be sloping, with an elevation mostly below 20 meters above sea level. In addition, what exacerbates the potential for flood vulnerability is the opening of the Shiroro dam reservoir through the dam spillway gates whenever it overflows.

Figure 4.29a shows the settlements in light blue downstream of the dam that are highly vulnerable when the dam water spills to the floodplain and the settlements in sky blue that are not vulnerable. Figure 4.29b presents the settlements in blue that are highly vulnerable when the dam water spills to the floodplain; likewise, Figure 4.29c shows the settlements in deep blue high flooded and in sky blue that will be fair when the dam water is released when the weighted overlay of flood-vulnerable areas in the study area.

On the other hand, Tables 4.7–4.7a, Tables 4.8–4.8a, and Tables 4.9–4.9a present the names and total numbers of the settlements that invaded at the different flood heights obtained from the DEMs (UAV 1 m, InSAR 10 m, and SRTM 30 m). However, the effect of DEM on regional flood vulnerability varies depending on the level of elevation. Where a region shows low heights, the flooding is high, and vice versa.

4.11.9 Model validation of the study area discussion of results

When compared to the earlier study by NSEMA, only the UAV-derived 1 m DEM resolution agreed with the NSEMA record and also agreed with the work of Leitao *et al.* (2016) and Esmaeel *et al.* (2022), while the other DEMs (10 m InSAR DEM and 30 m SRTM DEM resolution) show a significant difference in the flood extent in the study area. Tables 4.10-4.10a, b; Tables 4.11-4.11a, b; and Tables 4.12-4.12a, b show the results of different DEM sources used for this study and the NSEMA (2021) results. Figure 4.30 presents the graphical representation of UAV-derived DEM 1 m conformity with the NSEMA data and other overestimates of the flood extent.

4.12 Discussion of Results Based on the Objectives of the Study

The section discussed the results concerning the objectives of the study. Subsections 4.10.1 to 4.10.4 discuss the results achieved.

4.12.1 Assessment of the topographic accuracies of the DEM Sources discussion of results

The topographic accuracies between the generated UAV, InSAR, and SRM DEMs were assessed by comparing the descriptive statistics of both DEMs (Figure 4.16). The differences between the UAV-derived DEM, InSAR-derived DEM, and the SRTM DEM are visually minimal and are better than the residuals. The vertical accuracy of the DEM sources was achieved using the actual heights of the DEMs. The analysis shows that

UAV-derived DEM is more reliable and accurate, followed by InSAR DEM, and the least was the SRTM DEM. The results indicate that the vertical accuracy of DEMs is 601.679 m, 635.599 m, and 665.032 m for UAV, InSAR, and SRTM DEMs, respectively (Table 4.1). SRTM DEM had the highest absolute, relative, and root mean square errors, maximum positive and negative deviation, a difference with reference heights, and the lowest correlation coefficient. Therefore, SRTM DEM is the least acceptable source for studying flood vulnerability among the DEM sources used.

4.12.2 Generation of high-resolution DEM using UAV data discussion of results

The second objective was to generate a high-resolution DEM of the study area from primary UAV data and ascertain its topographic accuracy. Raster elevation maps were successfully generated from photogrammetric data using Trimble Business Centre Photogrammetry Software. Conclusions from the results and analysis obtained from this study indicate that the UAV images the updating and revision of topographic maps with ground control points (GCPs) and a high percentage of forward and side overlaps. This research affirms the suitability of UAVs in areas that are partly accessible or inaccessible. The map accuracy in terms of horizontal and vertical accuracy is 3.207 m (RMSE = 1.85 m) and 0.884 m (RMSE = 0.45 m), respectively. The DEM generated from Trimble Aerial Imaging Solution should be employed to achieve accurate mapping because it falls below the maximum allowable RMSE according to the American Society for Photogrammetry and Remote Sensing (Lawali and Dauda, 2014) and the National Standard for Spatial Data Accuracy. This study has looked into the geometric quality through the geometric accuracy and resolution of its products for flood modelling.

4.12.3 Develop an accurate flood extent modelling approach using DEM sources in the study area discussion of results

The third objective modelled the flood extent of the study area using DEMs from three sources: UAV 1 m, InSAR 10 m, and SRTM 30 m. The 2D flood inundation modelling using ArcScene in ArcGIS 10.4 software was used to simulate surface flooding caused by rainfall and river flooding in the study area. The river discharge, flow velocity, and flood level that determined the flood extent of the study area using DEMs from three sources were computed in MATLAB using the shallow water equation, the river bathymetry data, and the different DEMs. The analysis of discharge data from UAV-derived 1 m, InSAR 10 m, and SRTM 30 m DEMs has a close relationship between InSAR and UAV data in some locations. The RMSE for UAV-InSAR is 72.0248, while SRTM has 127.859, indicating a difference in discharge value (Figure 4.24a).

Figure 4.24b analyses flow velocity differences between UAV-derived 1 m, InSAR 10 m, and SRTM 30 m DEMs. InSAR provides a more precise discharge velocity difference to SRTM, with an RMSE of 0.49863 for UAV-InSAR and 0.81878 for UAV-SRTM. While Figure 4.24c shows UAV-InSAR DEMs have a 15.688 RMSE, UAV-SRTM DEMs have a 20.7791 RMSE, indicating a closer elevation difference. The results clearly show the effectiveness of the UAV-derived 1 m DEM with its high resolution on the discharge rate and flow velocity to model the flood extent of the study area scientifically, followed by the InSAR 10 m DEM, while the SRTM 30 m DEM is the least effective among them based on poor resolution.

4.12.4 Assessment of the effect of DEM resolution on flood modelling discussion of results

The fourth objective evaluated the impact of the various DEM sources on the accuracy of flood modelling in the study area. It is observed from the results in Figure 4.30 that only the UAV-derived 1 m DEM conformed with the existing ground conditions with the other DEMs (10 m InSAR DEM and 30 m SRTM DEM) showed a significant difference in the flood extent in the study area. The 1 m DEM from the UAV was in line with how the Niger State Emergency Agency (NSEMA, 2021) classified the flood-vulnerable settlements in the study area. The high resolution agreed with the work done by Mazoleni *et al.* (2020).

However, results from the InSAR 10 m DEM have some reasonable performance ranked with the UAV-derived 1 m DEM. The SRTM DEM indicated that it overpredicted the flood levels in the study area due to the poor resolution of the DEM. Also, studies that compare UAV DEM accuracy with high-accuracy DEM data from other sources, such as LiDAR (Unger *et al.,* 2014; Leitao *et al.,* 2016), show that UAV DEM performance may be on par with LiDAR. (Esmaeel *et al.,* 2022) also revealed in their study that UAV DEMs provide high accuracy in flood simulation compared to global DEMs. These all show convergence with the conclusions derived from this study.

The findings of this study also have implications for other flood risk management activities, such as emergency evacuation routes. The approach provides reliable flood risk maps from high- and low-resolution DEM sources. Such maps can then inform the development of better overall flood risk management practices.

4.13 Findings from the Results

This study examined the impact of spatial resolutions of DEMs on the accuracy of flood modelling using the floodplain of the Shiroro Dam in Niger State, Nigeria, as a case study. The key findings of the study are as follows:

i.   A strong correlation exists between the InSAR-derived 10 m DEM and the SRTM-derived 30 m DEM despite differences in their spatial resolution. Even though the InSAR DEM with a 10 m spatial resolution is still more similar to the UAV DEM than the SRTM DEM with a 30 m spatial resolution, the study suggests that the similarity between the InSAR and SRTM DEMs is because they are both radar-derived heights and, as a result, have similar spatial responses to their environments (Nwilo *et al.,* 2012). Even though both the InSAR DEM and the SRTM DEM use the same operational method, the InSAR DEM is better than the SRTM DEM because of the difference in the radar response bands (band C for InSAR and band L for SRTM) and the spatial resolution of the resulting image (Nwilo *et al.,* 2012).

ii.   The study found that selecting the same DEM and different spatial resolutions for flooding simulations results in differences. As the spatial resolution of the DEM decreases, the predicted flood inundation area and the maximum inundation depth increase for all the low-resolution DEMs. It implies that a low-resolution DEM may lead to more errors in the inundation results.

iii.   InSAR DEMs and SRTM have a positive (0.9996) correlation with UAV-derived DEMs in the elevation data (Table 4.4).

iv.   UAV data with InSAR and SRTM yielded RMSEs of 0.249 m, 0.352 m, and 0.455 m, respectively.

v.   The F-critical value for DEMs is 2.996, below the expected F-table value for 10,000 points, 394.722, at the 95% confidence interval (Table 4.2 and 4.2a).

vi.   Low-resolution DEMs lead to an increase in the flood extent and depth. Invariably, it exaggerates the flood depths due to increased elevation. The flood depth and flood extent increased with decreasing DEM resolution.

vii.   Conversely, flood models generated from high-resolution DEM have better accuracy than the resulting models.

viii.   In flood extent, low-resolution DEMs produced higher estimate of the flood risk situation in the study area compared with high-resolution DEMs.

ix.   The result from the UAV-derived 1 m DEM provided a more defined flood extent and clearly showed the distribution of hazard levels based on its high resolution. However, the InSAR 10 m DEM has some reasonable performance with the UAV-derived 1 m DEM. While the SRTM DEM indicated that it produced higher estimate of the flood risk situation in the study area, this was due to the poor resolution of the DEM.

CHAPTER FIVE

5.0   **CONCLUSION AND RECOMMENDATIONS**

5.1   Conclusion

Flooding is one of the most devastating natural disasters, occurring annually in many parts of the world (Sauer *et al.,* 2021). It remains a significant natural hazard despite recent advances in the scientific mechanisms causing it and increased expenditure on flood defenses. Developing flood models helps policymakers make timely decisions about emergency responses and future planning. The thesis established the impact of DEM resolutions in flood modelling. This study generated two different DEMs of high spatial resolution: a UAV-derived 1 m DEM and an InSAR 10 m DEM, and also utilised an SRTM 30 m DEM, and then investigated how the DEMs affected flood modelling results in the study area.

The SWE was implemented in MATLAB using river channel bathymetric data, Manning coefficients, and DEMs computed for discharge and flow velocity, determined flood levels for the study area. The findings from the study confirmed that accurate terrain data has an impact on modelling flood hazards. Specifically, the results of flood simulations varied in response to different DEM resolutions, which can be associated with the degree of representation of the topography by the DEMs.

In addition, high-resolution DEMs from UAV-derived 1 m resolution provide relevant and reliable flood modelling results; low-resolution DEMs from InSAR 10 m and SRTM 30 m produced higher estimate of the flood risk situation in the study area. The UAV-derived 1 m gives a more defined flood extent and clearly shows the distribution of hazard levels. Hence, a high-resolution DEM is necessary for decision-makers in local-scale inundation predictions. Furthermore, accurate DEM for flood simulation provides an initial assessment of the possible population and areas affected by low and high flood

hazards. The Root Mean Square Error (RMSE) values of the three DEM resolution data were 0.249 m, 0.352 m, and 0.455 m, respectively. The thesis affirmed that UAV DEM provides higher accuracy in the simulation of flood hazards compared to the other two DEMs (10 m InSAR and 30 m SRTM), which contain observational constraints in flood risk simulation. It implies that the higher the DEM resolution, the greater the preservation of the topographic terrain features.

In this study, flood levels within the Shiroro floodplains were 150 m and 250 m from UAV-derived DEM 1 m resolution data as against 160 m and 270 m and 200 m and 280 m from the InSAR 10 m and SRTM 30 m DEM resolution data, which conforms with the results of the Niger State Emergency Management Agency (NSEMA, 2021). The study confirmed that 1 m UAV-derived resolution DEMs provide high accuracy in flood simulation compared to global DEMs. These all show convergence with the conclusion derived from this study by Unger *et al.,* (2014), Leitao and de Sousa (2018), and Esmael *et al.,* (2022). This finding from the study helps determine possible evacuation centers and establish significant infrastructure for the settlements around the floodplain.

5.2   Recommendations

The study recommends that DEMs of higher resolution from 1 m UAV-derived data be used in floodplain modelling for optimal accuracy instead of adopting the trial-and-error method. Government agencies such as NEMA, NSEMA, NIMET, and other relevant stakeholders should use the findings from the study for effective flood disaster planning, response, and mitigation.

5.3   Contribution to Knowledge

The study has contributed to the existing body of knowledge by generating two different DEMs of high spatial resolution from an unmanned aerial vehicle (UAV) at 1 m

resolution, an interferometry synthetic aperture radar (InSAR) at 10 m resolution, and also utilising a Shuttle Radar Topographic Mission (SRTM) at 30 m resolution. The study has used generated DEMs to examine the assessment of the impact of flooding at Shiroro Dam, Niger State, Nigeria. The study developed a MATLAB program to implement the Shallow Water Equation (SWE) using river channel bathymetric data, Manning coefficients, rainfall data, DEMs, and hydrological and hydraulic flood models for the assessment.The findings of the study showed that the UAV-derived 1 m DEM reliably predicted the flood risk situation due to its superior spatial resolution compared to the other two DEMs, InSAR 10 m and SRTM 30 m, which produced a higher estimate of the flood risk situation in the study area.The study affirmed that the UAV-derived 1 m DEM provides high accuracy in the flood simulation of flood hazards compared to the other two DEMs (10 m InSAR and 30 m SRTM), which contain observational constraints in flood risk simulation. It implies that the higher the DEM resolution, the greater the preservation of topographic terrain features.

5.4 Suggestions for Further Study

Based on the study's findings and limitations, further studies should consider high-spatial-resolution DEMs < 1 m from various sources for flood vulnerability assessment.

References

Abrams, M. (2000). The Advanced Spaceborne Thermal Emission and Reflection Radiometer (ASTER): Data products for the high spatial resolution imager on NASA's Terra platform. *International Journal of Remote Sensing*, 21, 847-859.

Adebanji, W. A. (2014). *Empirics of Standard Deviation.* Conference Research Presentation at Covenant University. DOI:10.13140/2.1.1444.6729

Adesina, E. A., Musa, A., Ajayi, O. G., Odumosu, J. O., Opaluwa, Y. D., & Onuigbo, I. C. (2021). Comparative Assessment of SRTM and UAV-Derived Dem in Flood Modelling. *Environmental Technology and Science Journal.* 12(2), 58-70. https://dx.doi.org/10.4314/etsj.v12i2.6.

Adesina, E.A., Musa, A., Onuigbo, I.C., & Adesiji, A. R. (2022). *Assessment of the Hydrological Characteristics of Shiroro Dam, Nigeria.* SETIC 2022 International Conference: Sustainable Development and Resilience of the Built Environment in the Era of Pandemic. School of Environmental Technology, Federal University of Technology, Minna. 115-122. ISBN 978-978-54580-8-4.

Adetunji, M. A., & Oyeleye, O. I. (2018). Assessment and Control Measures of Flood Risk in Ajibode Area of Ibadan, Oyo State, Nigeria. *International Journal of Physical and Human Geography*, 6(1): 1-16.

Adie, D.B., Ismail, A., Uhammad, M. M., & Aliyu, U. B. (2012). Analysis of the Water Resources Potential and Useful Life of the Shiroro Dam, Nigerian. *Journal of Basic and Applied Science*, 20(4), 341-348. http://www.ajol.info/index.php/njbas/index.

Adnan, N. A., & Atkinson, P. M. (2012). *Remote Sensing of River Bathymetry for Use in Hydraulic Model Prediction of Flood Inundation*. IEEE 8th International Colloquium on Signal Processing and its Applications. 159-163. DOI:10.1109/CSPA.2012.6194710

Afshari, S., Tavakoly, A. A., Rajib, M. A., Zheng, X., Follum, M. L., Omranian, E., & Fekete, B. M. (2018). Comparison of New Generation Low-Complexity Flood Inundation Mapping Tools with a Hydrodynamic Model. *Journal of Hydrology*, 556, 539-556.

Ahmad, A. (2014). Dynamic Modelling of Flood Management Policies. In S. P. Simonovic (Ed.), *Floods in a Changing Climate*: *Risk management*. Cambridge University Press, 83-108.

Ajayi, O. G., Salubi, A. A., Angbas, A. F., & Odigure, M. G. (2017). Generation of Accurate Digital Elevation Models from UAV Acquired Low Percentage of Overlapping Images. *International Journal of Remote Sensing*. 8-10(38), 3113-3134.

Alfieri, L., Bisselink, B., Dottori, F., Naumann, G., De Roo, A., Salamon, P., Wyser, K. & Feyen, L. (2017). Global Projections of River Flood Risk in a Warmer World. *Earth's Future*, 5, 171-182.

Ali, A.M., Baldassarre, G.D., & Solomatine, D.P. (2015). Testing Different Cross-Section Spacing in 1D Hydraulic Modelling: A Case Study on Johor River, Malaysia. *Hydrology Science Journal,* 60, 351–360. https://doi.org/10.1080/02626667.2014.889297.

Allen, G. H., & Pavelsky, T. M. (2018). Global Extent of Rivers and Streams. *Science*. 10.1126/science. aat0636.

Almoradie, A., de Brito, M. M., Evers, M., Bossa, A., Lumor, M., Norman, C., Yacouba, Y., & Hounkpe, J. (2020). Current Flood Risk Management Practices in Ghana: Gaps and Opportunities for Improving Resilience. *Journal of Flood Risk Management*. 13 (4), p. e12664.

Anuar, B. (2018). Flood Inundation Modelling and Hazard Mapping Under Uncertainty in the Sungai Johor Basin, Malaysia. *Earth Sciences, Engineering & Technology.* https://doi.org/10.1201/9780429469015.

Anusha, N., & Bharathi, V. (2019). Change Detection and Flood Water Mapping Using Sentinel-1A Synthetic Aperture Radar Images. *Journal of Computational and Theoretical Nanoscience*. 16(8):3544-3549. DOI:10.1166/jctn.2019.8321.

Arnell, N. W., & Gosling, S. N. (2016). The Impacts of Climate Change on River Flood Risk at the Global Scale. *Climatic Change*, 134, 387-401.

Arnell, N. W., Lowe, J. A., Lloyd-Hughes, B., & Osborn, T. J. (2018). The impacts Avoided with a 1.5 °C Climate Target: A Global and Regional Assessment. *Climatic Change*, 147, 61-76.

Aronica, G., Franza, F., Bates, P.D., & Neal, J.C. (2016). Probabilistic Evaluation of Flood Hazard in Urban Areas Using Monte Carlo Simulation. *Hydrological Processes* 26: 3962–3972.

Asselman, N., Bates, P., Woodhead, S., Fewtrell, T., Soares-Frazao, S., Zech, Y., Velickovic, M., De Wit, A., Ter Maat, J., Verhoeven, G., & Lhomme, J. (2009). Flood Inundation Modelling – Model Choice and Proper Application. *Flood Site Report*. T08-09-03, pp.142.

Azizian, A., & Brocca, L. (2020). Determining the Best Remotely Sensed DEM for flood Inundation Mapping in Data-Sparse Regions. *International Journal of Remote Sensing*. 41, 1884–1906. https://doi.org/10.1080/01431161.2019.1677968.

Azmi, S. M., Baharin, A., & Ahmad, A. (2014). *Accuracy Assessment of Topographic Mapping Using UAV Image Integrated with Satellite Images*. IOP Publishing Ltd.

Bamidele, O. F., & Badiora, A. I. (2019). Flood disaster vulnerability in North Central Nigeria. *International Journal of Research and Innovation in Social Science*, 3(12): 364-371.

Baran, M.P., Stewart, B., Kampes, B.M., Perski, Z., & Lilly, P. (2003). *A Modification to the Goldstein Radar Interferogram Filter.* IEEE Transactions on Geoscience and Remote Sensing, 41(9): 2114-2118.

Barthelemy, S., Ricci, S., Morel, T., Goutal, N., Le Pape, E., & Zaoui, F. (2018). On operational Flood Forecasting System Involving 1D/2D Coupled Hydraulic Model and Data Assimilation. *Journal of Hydrology*, 562, 623-63

Bates, P. D., Dawson, R. J., Hall, J. W., Horritt, M. S., Nicholls, R. J., Wicks, J., Mohamed, A. A., & Mohamed, H. (2005). Simplified Two-Dimensional Numerical Modelling of Coastal Flooding and Example Applications. *Coastal Engineering*, 52, 793-810.

Bates, P., & De Roo, A. P. J. (2000). A Simple Raster-Based Model for Flood Inundation Simulation. *Journal of Hydrology,* 236, 54-77.

Bates, P. D. (2012). Integrating Remote Sensing Data with Flood Inundation Models: How Far Have We Got? *Hydrological Processes*, 26, 2515-2521.

Bates, P., Pappenberger, F., & Romanowicz, R. J. (2013). Uncertainty in Flood Inundation Modelling (chap. 10). In K. Beven & J. Hall (Eds.), *Applied Uncertainty Analysis for Flood Risk Management*, 230–267. London: Imperial College Press.

Berner, Z. A., Bleeck-Schmidt, S., Stuben, D., Neumann, T., Fuchs, M. & Lehmann, M. (2012). Floodplain deposits: A geochemical archive of flood history – A case study on the River Rhine, Germany. *Applied Geochemistry*, 27, 543-561.

Berti, M., Corsini, A., Franceschini, S., Iannacone, J. P. (2013). Automated classification of Persistent Scatterers Interferometry time series. *Natural Hazards and Earth System Sciences,* 13(8), 1945-1958.

Beven, K. J., Aspinall, W. P., Bates, P. D., Borgomeo, E., Goda, K., Hall, J. W., Page, T., Phillips, J. C., Simpson, M., Smith, P. J., Wagener, T., & Watson, M. (2018). Epistemic Uncertainties and Natural Hazard Risk Assessment, Part 2: What should constitute good practice? *Natural Hazards and Earth System Sciences,* 18, 2769-2783.

Beven, K., & Westerberg, I. (2011). On Red Herrings and Real Herrings: Disinformation and Information in Hydrological Inference. *Hydrological Processes*, 25, 1676-1680.

Bhuyian, M. A. H., & Kalyanapu, A. J. (2018). Comparative Assessment of Shuttle Radar Topography Mission (SRTM) and Advanced Space-borne Thermal Emission and Reflection Radiometer Global Digital Elevation Model (ASTER GDEM) in flood inundation modelling. *Journal of Hydrology*, 566, 826-838.

Box, G. E. P. & Jenkins, G. M. (1970). *Time Series Analysis: Forecasting and Control,* San Francisco, USA, Holden-Day Press.

Brandimarte, L. (2012). Theoretical background: steady flow. In: Di Baldassarre, G. (ed.) *Floods in a Changing Climate: Inundation Modelling*. Cambridge: Cambridge University Press.

Brazdil, R., Chroma, K., Reznickova, L., Valasek, H., Dolák, L., Stachon, Z., Soukalova, E., & Dobrovolny, P. (2014). The Use of Taxation Records in Assessing Historical Floods in South Moravia, Czech Republic. *Hydrology and Earth System Sciences*, 18, 3873-3889.

Brazdil, R., Kundzewicz, Z. W., & Benito, G. (2006). Historical Hydrology for Studying Flood Risk in Europe. *Hydrological Sciences Journal*, 51, 739-764.

Burnham, K. P., & Anderson, D. R. (2002). *Model Selection and Multimodel Inference*, New York, Springer.

Chaudhry, M. H. (2007). *Open-Channel Flow,* Second Edition. Springer. Library of Congress Control Number: 2007936602. ISBN 978-0-387-30174-7 e

Chen, C. W., & Zebker, H. A. (2001). Two-Dimensional Phase Unwrapping with the Use of Statistical Models for Cost Functions in Nonlinear Optimization. *Journal of the Optical Society of America,* 18(2), 338-351

Chow, V. (1959). *Open-channel Hydraulics*. New York, McGraw Hill.

Chu, T., & Lindenschmidt, K.E. (2017). Comparison and Validation of Digital Elevation Models Derived from InSAR for a Flat Inland Delta in the High Latitudes of Northern Canada. *Journal Remote Sensing*. 43, 109–123. doi: 10.1080/07038992.2017.1286936.

Cobby, D.M., Mason, D.C., & Davenport, I. J. (2001). Image Processing of Airborne Scanning Laser Altimetry Data for Improved River Flood Modelling. *ISPRS Journal of Photogrammetry and Remote Sensing* 56(2): 121–138.

Cook, A., & Merwade, V. (2009). Effect of Topographic Data, Geometric Configuration and Modelling Approach on Flood Inundation Mapping. *Journal of Hydrology*, 377 (1-2), 131-142.

Corringham, T.W., & Cayan, D.R. (2019). The Effect of Flood Damages in the Western United States Weather. *Climate Society*, 11, 489–504. https://doi.org/10.1175/ WCAS-D18-0071.1

Coveney, S., & Fotheringham, A.S. (2011). The impact of DEM Data Source on Prediction of Flooding and Erosion Risk due to Sea-Level Rise. *International Journal of Geographical Information Science* 25 (7): 1191–1211.

Coveney, S., & Roberts, K. (2017). Lightweight UAV Digital Elevation Models and Ortho Imagery for Environmental Applications: Data Accuracy Evaluation and Potential for River Flood Risk Modelling. *International Journal of Remote Sensing*, 38, 3159-3180.

Crippen, R., Buckley, S., Agram, P., Belz, E., Gurrola, E., Hensley, S., Kobrick, M., Lavalle, M., Martin, J., Neumann, M., Nguyen, Q., Rosen, P., Shimada, J., Simard, M., & Tung, W. (2016). NASADEM Global Elevation Model: Methods and Progress. *ISPRS Annals of Photogrammetry, Remote Sensing and Spatial Information Sciences.* XLI-B4, 125–128, http://www.isprs-ann-photogramm-remote-sens-spatial559 inf-sci.net/III-4/17/2016/.

Cunge, J. A. (2003). Comment on Data and Models. *Journal of Hydroinformatics* 6(1):75-77. DOI:10.2166/hydro.2004.0006

Curtis, W. C., & Zebker, H. A. (2000). Network Approaches Two-Dimensional Phase Unwrapping: Intractability and Two New Algorithms: erratum. *Journal of the Optical Society of America*, 18(5). DOI:10.1364/JOSAA.18.001192.

Danielson, J. J., & Gesch, D. B. (2011). *Global Multi-Resolution Terrain Elevation Data 2010 (GMTED2010).*

Darnell, A., Tate, N., & Brunsdon, C. (2008). Improving User Assessment of Error Implications in Digital Elevation Models. *Computers, Environment and Urban Systems*, 32:268–277.

Dawod, G. M., & Ascoura, I. E. (2021) The Validity of Open-Source Elevations for Different Topographic Map Scales and Geomatics Applications. *Journal of Geographic Information System,* 13(2): 1-18

Deng, B., Lai, S. H., Jaing, C., Kumar, P., El-Shafie, A., & Chin, R. J. (2021). Advanced Water Level Prediction for a Large-Scale River–Lake System using Hybrid Soft Computing Approach: A Case Study in Dongting Lake, China. *Earth Science Informatics*, 14(4), 1987–2001. https://doi.org/10.1007/s12145-021-00665-8

Di Baldassarre, G. (2012a). Model Building. In: Di Baldassarre, G. (ed.) *Floods in a Changing Climate: Inundation Modelling.* Cambridge: Cambridge University Press.

Di Baldassarre, G. (2012b). Model Evaluation. In: Di Baldassarre, G. (ed.) *Floods in a Changing Climate: Inundation Modelling.* Cambridge: *Cambridge University Press*.

Domeneghetti, A., Vorogushyn, S., Castellarin, A., Merz, B., & Brath, A. (2013). Probabilistic Flood Hazard Mapping: Effects of Uncertain Boundary Conditions. *Hydrology and Earth System Sciences,* 17, 3127-3140.

Dottori, F., Szewczyk, W., Ciscar, J.-C., Zhao, F., Alfieri, L., Hirabayashi, Y., Bianchi, A., Mongelli, I., Frieler, K., Betts, R. A., & Feyen, L. (2018). Increased Human and Economic Losses from River Flooding with Anthropogenic Warming. *Nature Climate Change*, 8, 781-786.

Dowman, I., & Michalis, P. (2004). The use of Rational Functions for Mapping from High-Resolution Satellites: A Case Study Using IKONOS Imagery. *Photogrammetric Engineering & Remote Sensing,* 70(11), 1267-1272.

Egbenta, A. N., Ojeh, V. N., & Ekwe, C. I. (2015). Climate change and flooding in Nigeria: The impacts, implications, and the way forward. *Journal of Geosciences and Geomatics*, 3(1), 18-29.

Ejemma, E., Sunday, V. N., Eluwah, A.N., & Onwuchkwa, I. S. (2014). Mapping Flood Vulnerability Arising from Land Use / Land Covers Change along River Kaduna, Kaduna State, Nigeria. *(IOSR) Journal of Humanities and Social Sciences*, 19(7), 155–160.

Ekpoh, I. J. (2015). Climate Change and Recent Severe Flooding in Uyo, Akwa Ibom State, Nigeria. *Global Journal of Social Sciences*, 14, 23-3

Erban, L. E., & Gorelick, S. M. (2016). Closing the Irrigation Deficit in Cambodia: Implications for Transboundary Impacts on Groundwater and Mekong River flow. *Journal of Hydrology*, 535, 85-92.

Esmaeel, P., Shokoufeh, K., Seiyed, M.H., & Yaser, J.M. (2022). Application of Unmanned Aerial Vehicle DEM in Flood Modelling and Comparison with Global DEMs: A Case Study of the Atrak River Basin, Iran. *Journal of Environmental Management*, Volume 317, 115492 https://doi.org/10.1016/j.jenvman.2022.1154 92.

ESRI. (2014a). *ArcGIS 10.1 Help-Cell Size of Raster Data*. Environmental Systems Research Institute.

ESRI. (2014b). *ArcGIS 10.1 Help- Managing Elevation Data, Part 1*: About Elevation Data. Environmental Systems Research Institute.

Evans, U. F., Dominic, K. O., Evans, G. U., & Utting, C. (2017). Analysis of the Relative Contributions of Climatic Elements and Environmental Variables to Flood Disaster in Uyo, Akwa Ibom State, Nigeria. *International Journal of Environmental Sciences and Natural Resources*, 6(2)52-56

Eze, J.N., Vogel, C., & Ibrahim, P.A. (2018). Assessment of the Social Vulnerability of Households to Floods in Niger State, Nigeria. *International Letters of Social and Humanistic Sciences,* 84, 22–34. doi: www.scipress.com/ILSHS.84.22

Fang, J., Lincke, D., Brown, S., Nicholls, R., Wolff, C., Merkens, J., Hinkel, J., Vafeidis, A. (2020). Coastal Flood Risks in China through the 21st century – An application of DIVA. *Science of the Total Environment*. 704: Article 135311.

Farr, T. G., Rosen, P. A., Caro, E., Crippen, R., Duren, R., Hensley, S., & Alsdorf, D. (2007). The Shuttle Radar Topography Mission. *Reviews of Geophysics*, 45(2), RG2004. 1–33.

Ferretti, A. (2007). InSAR Principles: Guidelines for SAR Interferometry Processing and Interpretation. *European Space Agency*.

Fewtrell, T. J., Duncan, A., Sampson, C. C., Neal, J. C., & Bates, P. D. (2011). Benchmarking Urban Flood Models of Varying Complexity and Scale Using High-Resolution Terrestrial LiDAR Data. *Physics and Chemistry of the Earth, Parts* A/B/C, 36, 281-291.

Foni, A., & Seal, D. (2004). Shuttle Radar Topography Mission: An Innovative Approach to Shuttle Orbital Control. *Acta Astronautica*, 54: 565–570.

Gallegos, H. A., Schubert, J. E., & Sanders, B. F. (2009). Two-Dimensional, High-Resolution Modelling of Urban Dam-Break Flooding: A Case Study of Baldwin Hills, California. *Advances in Water Resources*, 32, 1323-1335.

Gallien, T. W., Schubert, J. E., & Sanders, B. F. (2011). Predicting Tidal Flooding of Urbanized Embankments: A Modelling Framework and Data Requirements. *Coastal Engineering*. 58, 567–577. doi: 10.1016/j.coastaleng.2011.01.011

Garba, S. B., Mustafa, M. R., & Ahmad, A. (2016). Flood Risk Assessment of River Kaduna Using Hydraulic Modelling and GIS Techniques. *Journal of Hydrology*: Regional Studies, 8, 69-79.

Getorb, 2005. Get Orbit (getorb), http://enterprise.lr.tudelft.nl/doris/tools/getorb/

Glaser, R., & Stangl, H. (2001). Floods in Central Europe since AD 1000: Dynamics, Risks and Cultural Adaptation. In Pfister, C., & Brazdil, R. (Eds.), *Climatic variability in sixteenth-century Europe and its social dimension*. Springer, 125-140.

GMT (2005). Generic Mapping Tools (GMT), University of Hawaii, http://gmt.soest.hawaii.edu/ Goldstein, R.M. and Werner, C.L., 1998. *Radar Interferogram Filtering for Geophysical Applications*. Geophysical Research Letters, 25(21): 4035-4038.

Goldstein, R. M., & Werner, C. L. (1998). Radar Interferogram Filtering for Geophysical Applications. *Geophysical Research Letters,* 25(21), 4035-4038.

Gonçalves, J. A., & Hawkere, R. (2015). UAV Photogrammetry for Topographic Monitoring of Coastal Areas. *ISPRS Journal of Photogrammetry and Remote Sensing*, 104, 101-111.

Grimaldi, S., Li, Y., Walker, J. P., & Pauwels, V. R. N. (2018). Effective Representation of River Geometry in Hydraulic Flood Forecast Models. *Water Resources Research*, 54, 1031-1057.

Gu, X., Zhang, Q., Singh, V.P., Song, C., Sun, P., & Li, J. (2019). Potential Contributions of Climate Change and Urbanization to Precipitation Trends Across China at National, Regional and Local Scales. *International Journal of Climatology* 39(6): 2998–3012.

Gupta, R., Negi, H. S., Pandey, A., & Pant, A. (2020). Evaluation of Digital Elevation Models for Flood Modelling Using Geomorphic Indices. *ISPRS International Journal of Geo-Information,* 9(5), 313.

Guzzetti, F., Cardinali, M., & Reichenbach, P. (1994). The AVI Project: A Bibliographical and Archive Inventory of Landslides and Floods in Italy. *Environmental Management*, 18, 623-633.

Haile, A., & Rientjes, T. (2005). Effects of LiDAR DEM Resolution in Flood Modelling: A Model Sensitivity Study for the City of Tegucigalpa, Honduras. *ISPRS* WG III/3, III/4, 168–173.

Hall, J. W., Tarantola, S., Bates, P. D., & Horritt, M. S. (2005). Distributed Sensitivity Analysis of Flood Inundation Model Calibration. *Journal of Hydraulic Engineering*, 131, 117-126.

Hanington, P., Thao, Q. T., Van, P. D. T., Doan, N. A. V., & Kiem, A. S. (2017). A Hydrological Model for Interprovincial Water Resource Planning and Management: A case study in the Long Xuyen Quadrangle, Mekong Delta, Vietnam. *Journal of Hydrology*, 547, 1-9.

Hashemi-Beni, L., Jones, J., & Thompson, G. (2018). Challenges and Opportunities for UAV-Based Digital Elevation Model Generation for Flood-Risk Management: A Case of Princeville, North Carolina. *Sensors,* 18:3843.

Hawker, L., Neal, J., & Bates, P. (2019) Accuracy assessment of the TanDEM-X Digital Elevation Model for Selected Floodplain Sites. *Remote Sensing of Environment,* 232: 1-14

Hawker, L., Bates, P. Neal, J., & Rougier, J. (2018). Perspectives on Digital Elevation Model (DEM) Simulation for Food Modelling in the Absence of High-Accuracy Open Access Global DEM. *Frontiers in Earth Science* 6: Article 233.

Herget, J., & Meurs, H. (2010). Reconstructing Peak Discharges for Historic Flood Levels in the City of Cologne, Germany. *Global and Planetary Change*, 70, 108-116.

Hilldale, R. C., & Raff, D. (2008). Assessing the Ability of Airborne LiDAR to Map River Bathymetry. *Earth Surface Processes and Landforms*, 33, 773-783. 295.

Hirabayashi, Y., Mahendran, R., Koirala, S., Konoshima, L., Yamazaki, D., Watanabe, S., Kim, H., & Kanae, S. (2013). Global Flood Risk Under Climate Change. *Nature Climate Change,* 3, 816-821.

Hladik, C., & Alber, M. (2012) Accuracy Assessment and Correction of a LIDAR-Derived Salt Marsh Digital Elevation Model. *Remote Sensing of Environment*. 121: 224-235

Horritt, M., Di Baldassarre, G., Bates, P., & Brath, A. (2007). Comparing the Performance of a 2-D Finite Element and a 2-D finite volume model of Floodplain Inundation using Airborne SAR Imagery. *Hydrological Processes*, 21, 2745-2759.

Horritt, M.S., & Bates, P. D. (2002). Evaluation of 1D and 2D Numerical Models for Predicting River Flood Inundation. *Journal Hydrology.* 268, 87–99. https://doi.org/10.1016/S0022-1694(02)00121-X

http://earthexplorer.usgs.gov

https://scihub.copernicus.eu/dhus/#/home.

Hu, Z., Peng, J., Hou, Y., & Shan, J. (2017). Evaluation of Recently Released Open Global Digital Elevation Models of Hubei, China. *Remote Sensing*, 9, 262. https://doi.org/10.3390/rs9030262.

Hughes, M.L., Patricia, F M., & Andrew, M.W. (2005). Accuracy Assessment of Georectified Aerial Photographs: Implications for Measuring Lateral Channel Movement in a GIS. *Elsevier B. V* doi: 10.1016/j.geomorph.2005.07.001.

Hunter, N. M., Bates, P. D., Horritt M. S., & Wilson, M. D. (2007). Simple Spatially-Distributed Models for Predicting Flood Inundation: A Review. *Geomorphology*. 90 (3-4), 208–225.

Hunter, N., Bates, P., Neelz, S., Pender, G., Villanueva, I., Wright, N., Liang, D., Falconer, R., Lin, B., Waller, S., Crossley, A., & Mason, D. (2008). Benchmarking 2D Hydraulic Models for Urban Flood Simulations. *Water Management,* 161. https://doi.org/10.1680/wama.2008.161.1.13.

Ikusemoran, M., Kolawole, M. S., & Martins, A. K. (2014). Terrain Analysis for Flood Disaster Vulnerability Assessment: A Case Study of Niger State, Nigeria. *American Journal of Geographic Information System*, 3(3), 122–134. http://doi.org/10.5923/j.ajgis.20140303.02

Ishaya, S., Ifatimehin, O. O & Abaje, I. B. (2009). Mapping Flood Vulnerable Areas in a Developing Urban Centre of Nigeria. *Journal of Sustainable Development in Africa*, 11(4): 180-194

Isikdogan, F., Bovik, A. C., & Passalacqua, P. (2017). Surface Water Mapping by Deep Learning. *IEEE Journal of Selected Topics in Applied Earth Observations and Remote Sensing*, 10(11), 4909-4918.

Jafarzadegan, A. A., & Merwade, V. (2017). Impact of DEM Resolution on Flood Inundation Modelling: A Case Study of the Wabash River. *Journal of Hydrology*, 547, 106-118.

Jakovljevic, A., Batica, J., & Gourbesville, P. (2019). Flood Modelling in Urban Areas: A Review of Challenges and Opportunities. *Water Science and Technology*, 79(7), 1264-1276.

James, G., Shaba, H., Zubair, O., Teslim, A., Nuhu, A., & Yusuf, G. (2013). Space-Based Disaster Management in Nigeria: The Role of the International Charter "Space & Major Disasters" Space-Based Disaster Management in Nigeria: *Journal Environment for Sustainability*, 1–16. Abuja, Nigeria.

Jarihani, A. A., Callow, J. N., Mcvicar, T. R., Van Niel, T. G., & Larsen, J. R. (2015). Satellite-derived Digital Elevation Model (DEM) selection, preparation and correction for Hydrodynamic Modelling in Large, Low-Gradient and Data-Sparse Catchments. *Journal of Hydrology*, 524, 489-506.

Jarvis, A., Reuter, H. I., Nelson, A., & Guevara, E. (2008). *Hole-Filled SRTM for the Globe Version 4*. Available from the CGIAR-CSI SRTM 90 m Database (http://srtm. csi. cgiar. org).

Javernick, L., Brasington, J., & Caruso, B. (2014). Modelling the Topography of Shallow Braided Rivers Using Structure-from-Motion Photogrammetry. *Geomorphology*, 213, 166-182.

Jawak, S. D., Trivedi, A., & Prakash, A. (2019). Evaluating the Accuracy of Digital Elevation Models Derived from UAV-Based Photogrammetry. *Geocarto International*, 34(11), 1172-1189.

Jing, C., Shortridge, A., Lin, S., & Wu, J. (2014). Comparison and Validation of SRTM and ASTER GDEM for a Subtropical Landscape in Southeastern China. *International Journal of Digital Earth,* 7, 969-992.

Jones, A. S., Charlesworth, S. M., & Gurney, R. J. (2020). A Comparative Study of Flood Frequency Estimation Techniques: Probabilistic Design Rainfall, Rainfall-Runoff and Continuous Simulation Models. *Journal of Hydrology*, 588, 125044.

Jones, A., Chadwick, A., Charlesworth, S., Gurney, R., & Brown, L. (2018). A Regional-Scale Assessment of the Impacts of Climate Change on Rainfall Intensity-Duration-Frequency Curves: Probabilistic Flood Risk Analysis for a Large Rural Catchment in Central England. *Journal of Hydrology*, 564, 948-961.

Jongman, B., Ward, P. J., & Aerts, J. C. (2012). Global Exposure to River and Coastal Flooding: Long-Term Trends and Changes. *Global Environmental Change*, 22, 823-835.

Junwei, Z., Weimin, B., Yu, L., Li, C., & Muxi, B. (2018). The Modified One-Dimensional Hydrodynamic Model Based on the Extended Chezy Formula. *Water*, 10, 1743; doi:10.3390/w10121743 www.mdpi.com/journal/water.

Kampes, B.M. (2005). Delft Object-oriented Interferometric Software (DORIS), Bert Kampes, TU, Delft, http:enterprise.lr.tudelft.nl/doris

Kampes, B.M., Hanssen, R.F., & Perski, Z. (2003). *Radar Interferometry with Public Domain Tools,* FRINGE 2003 Workshop. ESA/ESRIN, Frascati, Italy.

Karabork, H., Makineci, H.B., Orhan, O., & Karakus, P. (2021). Accuracy Assessment of DEMs Derived from Multiple SAR Data Using the InSAR Technique. *Arabian Journal Science Engineering.*, 46, 5755-5765.

Karamuz, E., Romanowicz, R., & Doroszkiewicz, J. (2020). The Use of Unmanned Aerial Vehicles in Flood Hazard Assessment. *Journal of Flood Risk Management,* 13(4): Article e12622.

Kenward, T., Lettenmaier, D.P., Wood, E.F., & Fielding, E. (2000). Effects of Digital Elevation Model Accuracy on Hydrologic Predictions. *Remote Sensing of Environment,* 74(3): 432–444.

Kepengn Xu., Jiayi, F., Yongqiang, F., Qinke, S., Chengbo, W., & Min, L. (2021). The Importance of Digital Elevation Model Selection in Flood Simulation and a Proposed Method to Reduce DEM Errors: A Case Study in Shanghai. *International Journal Disaster Risk Science*. 12:890–902 www.ijdrs.com. https://doi.org/10.1007/s13753-021-00377-z

Kiss, A. (2009). Floods and Weather in 1342 and 1343 in the Carpathian Basin. *Journal of Environmental Geography*, 2, 37-47

Koci, J., Jarihani, B., Leon, J. X., Sidle, R., Wilkinson, S., & Bartley, R. (2017). Assessment of UAV and Ground-Based Structure from Motion with Multi-View Stereo Photogrammetry in a Gullied Savanna Catchment. *ISPRS International Journal of GeoInformation*, 6(11), 328.

Kolawole, O.M., Olayemi, A. B., & Ajayi, K.T. (2011). Managing Flood in Nigerian Cities: Risk Analysis and Adaptation Options – Ilorin City as A Case study. *Archives of Applied Science Research,* 3 (1): 17-24

Komolafe, A. A., Adegboyega, S. A., & Akinluyi, F. O. (2015). A Review of Flood Risk Analysis in Nigeria. *American Journal of Environmental Sciences*, 11(3): 157-166

Komi, K., Neal, J., Trigg, M. A., & Diekkrüger, B. (2017). Modelling of Flood Hazard Extent in Data-Sparse Areas: A Case Study of the Oti River Basin, West Africa. *Journal of Hydrology: Regional Studies,* 10, 122-132.

Komolafe, A. A., Awe, B.S., Olorunfemi, I. E., & Oguntunde, P.G. (2020). Modelling Flood-Prone Area and Vulnerability using the Integration of Multi-Criteria Analysis and HAND Model in the Ogun River Basin, Nigeria. *Hydrological Sciences Journal*, 65(10), 17661783. doi: https://doi.org/10.1080/02626667.2020.1764960

Komolafe, A. A., Olorunfemi, I. E., Akinluyi, F.O., Adeyemi, M.A., & Ajayi, J.A. (2021). Enhanced Flood Hazard Modelling using Hydraulic, Analytical Hierarchical Process and Height Above Nearest Drainage Models in Ogunpa River Basin, Ibadan, Southwestern Nigeria. *Modelling Earth Systems and Environment* 7(2), 967–981. doi: https://doi.org/10.1007/s40808-020-01037-9

Komolafe, O. A. (2021). Rainfall Anomaly and Flooding in Nigeria: Implications and Preventive Measures. *International Journal of Water Resources and Environmental Engineering*, 7(9), 107-115.

Krsak, B., Blistan, P., Paulikova, A., Puskarova, P., Kovanic, L, Palkova, J., & Zeliznakova, V. (2016). Use of Low-Cost UAV Photogrammetry to Analyze the Accuracy of a Digital Elevation Model. *Measurement,* 91, 276–287

Kulkarni, A. T., Mohanty, J., Eldho, T. I., Rao, E. P., & Mohan, B. K. (2014). "A web GIS-Based Integrated Flood Assessment Modelling Tool for Coastal Urban Watersheds." *Computers & Geosciences,* 64, 7-14.

Kundzewicz, Z. W., Kanae, S., Seneviratne, S. I., Handmer, J., Nicholls, N., Peduzzi, P., Mechler, R., Bouwer, L. M., Arnell, N., Mach, K., Muir-Wood, R., Brakenridge, G. R., Kron, W., Benito, G., Honda, Y., Takahashi, K., & Sherstyukov, B. (2014). Flood Risk and Climate Change: Global and Regional Perspectives. *Hydrological Sciences Journal,* 59, 1-28.

Kung, O., Strecha, C., Beyeler, A., Zufferey, J. C., Floreano, D., Fua, P., & Gervais, F. (2011). *The Accuracy of Automatic Photogrammetric Techniques on Ultra-light UAV imagery.* In Unmanned Aerial Vehicle in Geomatics (No. EPFL-CONF-168806).

Kurniyaningrum, E., Limantara, L. M., Suhartanto, E., & Sisinggih, D. (2019). Sensitivity of Flow Depth Inundation Based on the Micro-Scale Topography in Krukut River, Jakarta, Indonesia. *International Journal of Civil Engineering and Technology*, 10, 697-706.

Lawali, R., & Dauda, A.W. (2014). "Digital Orthophoto Generation with Aerial Photographs." *Academic Journal of Interdisciplinary Studies,* MCSER Publishing. (3), 2281-3993.

Leandro, J., Chen, A. S., Djordjevic, S. & Savic, D. A. (2009). Comparison of 1D/1D and 1D/2D Coupled (Sewer/Surface) Hydraulic Models for Urban Flood Simulation. *Journal of Hydraulic Engineering*, 135, 495-506

Lee, G., Choi, M., Yu, W., & Jung, K. (2019). Creation of River Terrain Data Using Region Growing Method Based on Point Cloud Data from UAV Photography. *Quatum International* 519:255–262. https://doi.org/10.1016/j.quaint.2019.04.005

Lee, J., Ghorbanidehno, H., Farthing, M. W., Hesser, T. J., Darve, E. F., & Kitanidis, P. K. (2018). Riverine Bathymetry Imaging with Indirect Observations. *Water Resources Research*, 54, 3704-3727.

Legleiter, C. J., & Overstreet, B. T. (2012). Mapping Gravel Bed River Bathymetry from Space. *Journal of Geophysical Research: Earth Surface*, 117, n/a-n/a.

Leitao, J. P., Moy De Vitry, M., Scheidegger, A., Rieckermann, J. (2016). Assessing the Quality of Digital Elevation Models Obtained from Mini Unmanned Aerial Vehicles for Overland Flow Modelling in Urban Areas. *Hydrology and Earth System Sciences*, 20(4), 1637–1653. https://doi.org/10.5194/hess-20- 1637-2016

Leitao, J.P., & de Sousa, L.M. (2018). Towards the Optimal Fusion of High-Resolution Digital Elevation Models for Detailed Urban Flood Assessment. *Journal of Hydrology*. 561, 651–661.

Leon, J. X., Heuvelink, G. B. M., & Phinn, S. R. (2014). *Incorporating DEM Uncertainty in Coastal Inundation Mapping.* PLoS ONE, 9, e108727.

Leonard, M., Westra, S., Phatak, A., Lambert, M., Van Den, H.B., Mcinnes, K., Risbey, J., Schuster, S., Jakob, D., & Stafford-Smith, M. (2014). A Compound Event Framework for Understanding Extreme Impacts. Wiley Interdisciplinary Reviews: *Climate Change*, 5. 113-128.

Leopold, L. B., & Maddock, T. (1953). *Hydraulic Geometry of Stream Channels and Some Physiographic Implications*, Washington D.C, US Government Printing Office.

Li, F. F., Cao, H., Hao, C. F., & Qiu, J. (2021). Daily streamflow Forecasting Based on Flow Pattern Recognition. *Water Resources Management,* 35(13), 4601–4620. https://doi.org/10.1007/s11269-021-02971-8

Li, J., & Wong, D. W. S. (2010). Effects of DEM Sources on Hydrologic Applications. *Computers, Environment and Urban Systems,* 34, 251-261.

Li, J., He, Z., Plaza, J., Li, S., Chen, J., & Wu, H. (2017). Social Media: New Perspectives to Improve Remote Sensing for Emergency Response. *Process.* IEEE. 105, 1900–1912. doi: 10.1109/JPROC.2017.2684460

Li, W., Fang, H., Qin, G., Tan, X., Huang, Z., Zeng, F., Du, H., & Li, S. (2020). Concentration estimation of dissolved oxygen in Pearl River basin using Input Variable Selection and Machine Learning Techniques. *The Science of the Total Environment,* 731, 139099. https://doi.org/10.1016/j.scitotenv.2020.139099

Lin, N., Kopp, R.E., Horton, B.P., & Donnelly, J.P. (2016). Hurricane Sandy's flood frequency increased from the year 1800 to 2100. *Proceedings of the National Academy of Sciences* 113(43): Article 12071.

Manfreda, S., Nardi, F., Samela, C., Grimaldi, S., Taramasso, A. C., Roth, G., & Sole, A. (2014). Investigation on the use of Geomorphic Approaches for the Delineation of Flood-Prone Areas. *Journal of Hydrology*, 517, 863-876.

Manh, N. V., Dung, N. V., Hung, N. N., Merz, B., & Apel, H. (2014). Large-Scale Suspended Sediment Transport and Sediment Deposition in the Mekong Delta. *Hydrology and Earth System Sciences,* 18, 3033-3053.

Masood, M., & Takeuchi, K. (2011). Assessment of flood Hazard, Vulnerability and Risk of Mid-Eastern Dhaka Using DEM and 1D Hydrodynamic Model. *Natural Hazards*, 61(2): 757-770

Mayomi, I., Dami, A., & Maryah, U.M. (2014). GIS-Based Assessment of Flood Risk and Vulnerability of Communities in the Benue Floodplains, Adamawa State, Nigeria. *Journal Geography Geology.*, 5: 148-160. DOI: 10.5539/jgg. v5n4p148.

Mazzoleni, M., Paron, P., Reali, A., Juizo, D., Manane, J., Brandimarte, L. (2020). Testing UAV-Derived Topography for Hydraulic Modelling in A Tropical Environment. *Natural Hazards* 103:139–163. https://doi.org/10.1007/s11069-020-03963-4

McMillan, H., Krueger, T., & Freer, J. (2012). Benchmarking Observational Uncertainties for Hydrology: Rainfall, River Discharge and Water Quality. *Hydrological Processes*, 26, 4078-4111.

Mersel, M. K., Smith, L. C., Andreadis, K. M., & Durand, M. T. (2013). Estimation of River Depth from Remotely Sensed Hydraulic Relationships. *Water Resources Research*, 49, 3165-3179.

Merwade, V., Cook, A., & Coonrod, J. (2008). GIS Techniques for Creating River Terrain Models for Hydrodynamic Modelling and Flood Inundation Mapping. *Environmental Modelling and Software*, 23, 1300-1311.

Merz, B., Kreibich, H., Schwarze, R., & Thieken, A. (2010). Review the Article "Assessment of Economic Flood Damage". *Natural Hazards and Earth System Science*, 10, 1697-1724.

Mishra, D., & Satapathy, S. (2021). MCDM Approach for Mitigation of Flooding Risks in Odisha (India) Based on Information Retrieval. *International Journal Cognition Information National Intelligent.* 14 (2), 77–91. https://doi.org/10.4018/IJCINI.2020040105.

Mohamed, N., & Ali, G. (2019). Investigating Added Value of Improved DEM, River Geometry and Model Parameter Definitions on Flood Inundation Mapping. Proceedings SPIE 11149, Remote Sensing for Agriculture, *Ecosystems and Hydrology XXI*, 1114913. doi:10.1117/12.2532745

Mtamba, J., Van Der Velde, R., Ndomba, P., Zoltán, V., & Mtalo, F. (2015). Use of Radarsat2 and Landsat TM Images for Spatial Parameterization of Manning's Roughness Coefficient in *Hydraulic Modelling. Remote Sensing*, 7, 836-864.

Mukherjee, S., Joshi, P.K. Mukherjee, S. Ghosh, A. Garg, R.D., & Mukhopadhyay, A. (2013). Evaluation of vertical accuracy of open source Digital Elevation Model (DEM). *International Journal of Applied Earth Observation and Geoinformation*, 21(1): 205–217.

National Population Commission (NPC) (2006). *Nigeria National Census: Population Distribution by Sex, State, LGAs and Senatorial District: 2006 Census Priority Tables (Vol. 3).* http://www.population.gov.ng/index.php/publication/140-popn-distri-by-sex-state-jgas-and-senatorial-distr-2006

Neal, J., Schumann, G., & Bates, P. (2012). A Subgrid Channel Model for Simulating River Hydraulics and Floodplain Inundation Over Large and Data Sparse Areas. *Water Resources Research*, 48-52.

Neelz, S., & Pender, G. (2013). Benchmarking the Latest Generation of 2D Hydraulic Modelling Packages. Bristol: *Environment Agency*. 134-154.

Nickolay, Y.G., Vadim, A. S., & Andrey, V. K. (2018). Enforcing the Courant–Friedrichs–Lewy Condition in Explicitly Conservative Local Time Stepping Schemes. *Journal of Computational Physics.* 359, 93-105. https://doi.org/10.1016/j.jcp.2018.01.008.

Niger State Emergency Management Agency (NSEMA), (2021). Studies Conducted to Determine Flood Risk Communities Affected by Violent Water within Niger State, Nigeria.

Niger State Ministry of Lands and Survey Department, Minna, (2017)

Niger State. (2012). *Facts and Figures About Niger State, 52*. Retrieved from http://nigerstats.ni.gov.ng/uploads/docs/FACTS & FIGURES 2012.doc 2.pdf

Nigerian Emergency Management Agency (NEMA), (2019) *Floods – Situation Report*.

Niger State Geographical Information System (NIGIS)

Njoku, C. J., Effiong, J., & Ayara, N. (2020). A Geospatial Expose of Flood-Risk and Vulnerable Areas in Nigeria. *International Journal of Applied Geospatial Research,* 11(3): 87-110

Nkwunonwo, U.C M., & Whitworth, B. B. (2019). Urban flood Modelling Combining Cellular Automata Framework with Semi-Implicit Finite Difference Numerical Formulation, *Journal of Africa Earth Science*, 150, 272–281. Niger State. www.iiste.org ISSN 2224-5790 (Paper) ISSN 2225-0514 (Online) Vol.6, No.4.

Nkwunonwo, U.C., Whitworth, M., & Baily, B. (2020). A Review of the Current Status of Flood Modelling for Urban Flood Risk Management in Developing Countries. *Scientific African* 7, e00269. doi:https://doi.org/10.1016/j.sciaf. 2020.e00269

Nwilo, P.C., Olayinka, D. N., Okolie, C. J., & Adzandeh, E. A. (2012). Transformation OF Shuttle Radar Topography Mission (SRTM) Digital Elevation Data to Nigerian Height System. *FUTY Journal of the Environment*, Vol. 7, No. 1, ISSN: 1597-8826. http://dx.doi.org/10.4314/fje.v7i1.6

Ogania, J.L., Puno, G.R., Alivio, M.B.T., & Taylaran, J.M.G. (2019). Effect of digital elevation model' resolution in producing flood hazard maps. *Global Journal Environmental Science Management,* 5, 95-106. https://doi.org/10.22034/gjesm.2019.01.08.

Ojinnaka, O. C. (2007). *Principles of Hydrographic Surveying from Sextant to Satellite.* El' Demak Publishers, Enugu, Nigeria.

Okeke, F.I. (2006). *InSAR Operational and Processing Steps for DEM Generation. Promoting Land Administration and Good Governance*. 5th FIG Regional Conference Accra, Ghana. 1-13

Olagoke, D., James, Oluibukun, G.A., & Oladayo, O. (2017). The University of Lagos Assessing the Geometric Accuracy of UAV-Based Orthophotos. *South African Journal of Geomatics*. 6(3):395. DOI:10.4314/sajg. v6i3.9

Olajuyigbe, A. E., Rotowa, O. O., & Durojaye, E. (2012). An Assessment of Flood Hazard in Nigeria: The Case of Mile 12 Mediterranean, Lagos. *Journal of Social Sciences*, 3(2), 367–375. http://doi.org/10.5901/mjss.2012.v3n2.367

O'Loughlin, F. E., Neal, J., Yamazaki, D. & Bates, P. D. (2016a). ICESat-Derived Inland Water Surface Spot Heights. *Water Resources Research*, 52, 3276-3284.

O'Loughlin, F. E., Paiva, R. C., Durand, M., Alsdorf, D., & Bates, P. (2016b). A Multi-Sensor Approach Towards Global Vegetation Corrected SRTM DEM Product. *Remote Sensing Environment.* 182, 49–59. doi: 10.1016/j.rse.2016.04.018

Olukanni, D. O., & Salami, A. W. (2012). Assessment of Impact of Hydropower Dams Reservoir Outflow on the Downstream River Flood Regime–Nigeria's Experience. Chapters, in Hossein Samadi-Boroujeni (ed.), *Hydropower-Practice and Application*, Intech Open. http://doi.org/10.5772/33180.

Onwuemele, A. (2018). Public Perception of Flood Risks and Disaster Preparedness in Lagos Megacity, Nigeria. *Academic Journal of Interdisciplinary Studies*, 7(3): 179-185

Pedrozo-Acuna, A., Rodríguez-Rincón, J., Arganis-Juárez, M., Domínguez-Mora, R., & González Villareal, F. (2015). Estimation of probabilistic flood Inundation maps for an Extreme Event: Pánuco River, México. *Journal of Flood Risk Management* 8(2): 177–192.

Pender, G., & Neelz, S. (2007). Use of Computer Models of Flood Inundation to Facilitate Communication in Flood Risk Management. *Environmental Hazards*, 7, 106-114.

Popescu, I. (2012). Theoretical Background: Unsteady Flow. In: Di baldassarre, G. (ed.) *Floods in a Changing Climate: Inundation Modelling*. Cambridge: Cambridge University Press.

Popescu, D., Ichim, L., & Stoican, F. (2017). Unmanned Aerial Vehicle Systems for Remote Estimation of Flooded Areas Based on Complex Image Processing. *Sensors,*17, 446-456.

Puno, G., Amper, R.A., & Talisay, B.A. (2018). Flood simulation Using Geospatial and Hydrologic Models in Manupali Watershed, Bukidnon, Philippines. *Journal Biotechnology Environmental Science.,* 12(3): 294-303.

Puno, G., Villar, R., Bruno, A.G., & Corpuz, O. (2015). GIS-based DEM Resolution in Flood Hazard Maps Production Mapping and Morphometric Analysis of Flood Prone Sites in the Three Watersheds of Bukidnon. *International Journal Biotechnology. Allied Fields*, 3(7): 121-129.

Rabus, B., Eineder, M., Roth, A., & Bamler, R. (2003). The Shuttle Radar Topography Mission is A New Class of Digital Elevation Models Acquired by Space-Borne Radar. *ISPRS Journal of Photogrammetry and Remote Sensing*, 57, 241-262.

Rahmati, O., Darabi, H., Panahi, M., Kalantari, Z., Naghibi, S. A., Ferreira, C. S. S., Kornejady, A., Karimidastenaei, Z., Mohammadi, F., Stefanidis, S., Bu, D. T. & Haghighi, A. T. (2020). Development of Novel Hybridized Models for Urban Flood Susceptibility Mapping. *Scientific Reports* 10 (1), 1–19. https://doi.org/10.1038/s41598-020-69703-7.

Randa, O. T., Krhoda, O. G., Atela, O.J., Akala, H. (2022). Review of Flood Modelling and Models in Developing Cities and Informal Settlements: A case of Nairobi city. *Journal of Hydrology: Regional Studies.* Volume 43, 101188. https://doi.org/10.1016/j.ejrh.2022.101188

Rexer, M., & Hirt, C. (2014). Comparison of Free High-Resolution Digital Elevation Data Sets (ASTER GDEM2, SRTM v2.1/v4.1) and Validation Against Accurate Heights from the Australian National Gravity Database. *Australian Journal of Earth Sciences*, 61, 213-226. 305

Robinson, N., Regetz, J., & Guralnick, R. P. (2014). EarthEnv-DEM90: A Nearly-Global, Void-Free, Multi-Scale Smoothed, 90 m Digital Elevation Model from Fused ASTER and SRTM Data. *ISPRS Journal of Photogrammetry and Remote Sensing*, 87, 57-67.

Rodriguez, E., Morris, C.S., & Belz, J.E. (2006) A Global Assessment of the SRTM Performance. *Photogrammetry Engineering Remote Sensing*, 72:249–260

Saksena, S., & Merwade, V. (2015). Incorporating the Effect of DEM Resolution and Accuracy for Improved Flood Inundation Mapping. *Journal Hydrology,* 530, 180–194. https://doi.org/ 10.1016/j.jhydrol.2015.09.069.

Samela, C., Manfreda, S., Paola, F. D., Giugni, M., Sole, A. & Fiorentino, M. (2015). DEM-Based Approaches for the Delineation of Flood-Prone Areas in an Ungauged Basin in Africa. *Journal of Hydrologic Engineering*, 21.

Samela, C., Albano, R., Sole, A., & Manfreda, S. (2018). A GIS tool for cost-effective delineation of flood-prone areas. *Computers, Environment and Urban Systems*, 70, 43-52.

Sampson, C. C., Smith, A. M., Bates, P. D., Neal, J. C., Alfieri, L., & Freer, J. E. (2015). A High Resolution Global Flood Hazard Model. *Water Resources Research*, 51, 7358-7381. https://doi.org/10.1002/2015WR016954.

Sampson, C., Smith, A. Bates, P. Neal, J., & Trigg, M. (2016). Perspectives On Open Access High-Resolution Digital Elevation Models to Produce Global Flood Hazard Layers. *Frontiers in Earth Science 3*: Article 85.

Sanders, B. F. (2007). Evaluation of Online DEMs for Flood Inundation Modelling. *Advances in Water Resources*, 30, 1831-1843.

Sanders, B. F., Schubert, J. E., Goodrich, K. A., Houston, D., Feldman, D. L., Basolo, V. (2020). Collaborative Modelling with Fine-Resolution Data Enhances Flood Awareness, Minimizes Differences in Flood Perception, and Produces Actionable Flood Maps. *Earths Fut.* 8, 1–23. doi: 10.1029/2019EF001391

Sauer, I. J., Reese, R., Otto, C., Geiger, T., Willner, S. N., Guillod, B. P. (2021). Climate Signals in River Flood Damages Emerge Under Sound Regional Disaggregation. *Natural Communication.* 12, 1–11. doi: 10.1038/s41467-021-22153-9

Savage, J., Pianosi, F., Bates, P., Freer, J., & Wagener, T. (2016a). Quantifying the Importance of Spatial Resolution and Other Factors Through Global Sensitivity Analysis of a Flood Inundation Model. *Water Resources Research*, 52, 9146-9163.

Savage, J. T. S., Bates, P., Freer, J., Neal, J., & Aronica, G. (2016b). When Does Spatial Resolution Become Spurious in Probabilistic Flood Inundation Predictions? *Hydrological Processes*, 30, 2014-2032.

Sayers, P., Penning-Rowsell, E. C., & Horritt, M. (2018). Flood Vulnerability, Risk, and Social Disadvantage: Current and Future Patterns in the UK. *Regional Environmental Change*, 18, 339-352.

Scharroo, R., & Visser, P. (1998). Precise Orbit Determination and Gravity Field Improvement for the ERS Satellites. *Journal of Geophysical Research*, 103(C4): 8113- 8127.

Schumann, G.J.P., Muhlhausen, J., Andreadis, K. M. (2019). Rapid Mapping of Small-Scale River-Floodplain Environments using UAV SfM Supports the Classical Theory. *Remote Sensing*. 11:982-992

Serban, G., Rus, I., & Vele, D. (2016). Flood-Prone Area Delimitation using UAV Technology, in the Areas, Hard-to-Reach for Classic Aircraft: A Case Study in the North-East of Apuseni Mountains, Transylvania. *Natural Hazards*. 82:1817–1832. https://doi.org/10.1007/s11069-016-2266-4

Sheffer, N. A., Enzel, Y., Benito, G., Grodek, T., Poart, N., Lang, M., Naulet, R., & Coeur, D. (2003). Paleofloods and Historical Floods of the Ardèche River, France. *Water Resources Research*, 39. 345-355

Shibata, N., Nakai, F., Otsuyama, K., & Nakamura, S. (2022). Socio-Hydrological Modelling and its Issues in Japan: A Case Study in Naganuma District, Nagano City. *Hydrology Resource Letter* 16, 32–39. doi: 10.3178/hrl.16.32

Shiroro Dam Hydro-Power Authorities (2020). Hydrological data

Shiroro Local Government (SLG), (1999). The Potentiality of Industries and Agriculture in Shiroro Local Government Area of Niger State, Nigeria.

Slater, J. A., Garvey, G., Johnston, C., Haase, J., Heady, B., Kroenung, G., & Little, J. (2006). The SRTM Data 'Finishing' Process and Products, Photogrammetry. *Engineering Remote Sensing*., 72, 237–247.

Smith, A., Bates, P. D., Wing, O., Sampson, C., Quinn, N., & Neal, J. (2019). New Estimates of Flood Exposure in Developing Countries using High-Resolution Population Data. *Nature Communications,* 10(1), 1814-1824.

Smith, A., Sampson, C., & Bates, P. (2015). Regional Flood Frequency Analysis at the Global Scale. *Water Resources Research*, 51, 539-553.

SNAPHU, (2005). *Statistical-Cost, Network-Flow Algorithm for Phase Unwrapping (SNAPHU)*, Stanford University, http://www-star.stanford.edu/sar

Syifa, M., Chang-Wook, L., & Kadavi, P.R. (2019). An Artificial Intelligence Application for Post-Earthquake Damage Mapping in Palu, Central Sulawesi, *Indonesia. Sensors*. 19(3):542. DOI:10.3390/s19030542.

Tadono, T., Nagai, H., Ishida, H., Oda, F., Naito, S., Minakawa, K., & Iwamoto, H. (2016). Generation of the 30 M-Mesh Global Digital Surface Model by Alos Prism. *ISPRS - International Archives of the Photogrammetry, Remote Sensing and Spatial Information Sciences*, XLI-B4, 157-162.

Talchabhadel, R., Nakagawa, H., Kawaike, K. Yamanoi, K., & Thapa, B.R. (2021). Assessment of Vertical Accuracy of Open source 30m Resolution Space-Borne Digital Elevation Models. *Geomatics, Natural Hazards and Risk*, 12(1): 939-960.

Tariq, A., Shu, H., Kuriqi, A., Siddiqui, S., Gagnon, A. S., Lu, L., Linh, N., & Pham, Q. B. (2021). Characterization of the 2014 Indus River Flood Using Hydraulic Simulations and Satellite Images. *Remote Sensing*, 13 (11), 2053. https://doi.org/10.3390/rs13112053.

Tarpanelli, A., Brocca, L., Melone, F., & Moramarco, T. (2013). Hydraulic Modelling Calibration in Small Rivers by Using Coarse Resolution Synthetic Aperture Radar Imagery. *Hydrological Processes,* 27, 1321-1330.

Teng, J., Jakeman, A. J., Vaze, J., Croke, B. F. W., Dutta, D., & Kim, S. (2017). Flood inundation Modelling: A Review of Methods, Recent Advances and Uncertainty Analysis. *Environmental Modelling and Software* 90, 2012 16. doi: 10.1016/j.envsoft.2017.01.006.

Tom, G., & Mike, K.F. (2000). The Shuttle Radar Topography Mission. *Article in Eos Transactions American Geophysical Union*, 81, 583-585. DOI: 10.1029/EO081i048p00583

Udoh, J. J. (2015). Multi–Hazard Vulnerability Mapping: An Example of Akwa Ibom State, Nigeria. *European Scientific Journal,* 11(29): 293-300.

Ugbelase, V. N., Igbokwe, J. I., Emengini, J. E., Ejikeme, J. O., & Igbokwe, E. C. (2021). Generating and Analyzing Terrain Characteristics from Shuttle Radar Topographic Mission (SRTM), DEM. *World Journal of Advanced Research and Reviews*. 10(03), 198–206. DOI: https://doi.org/10.30574/wjarr.2021.10.3.0272

Unger, J., Reich, M., & Heipke, C. (2014). UAV-Based Photogrammetry: Monitoring of a Building Zone. *The International Archives of Photogrammetry, Remote Sensing and Spatial Information Sciences*, 40(5), 601.

UNISDR (2015). *The Human Cost of Weather-Related Disasters*. Geneva: UNISDR. Unmanned Aerial System (UAS) (2017. Flight Operations Manual

Unmanned Aerial System (UAS) (2017). *Flight Operations Manual*. City of Los Angeles Department of Public Works Bureau of Engineering.

Usman, A., & Ifabiyi, I. (2012). Socio-Economic Analysis of the Operational Impacts of Shiroro Hydropower Generation in the Lowland. *International Journal of Academic Research in Business and Social Sciences.* Vol. 2, No. 4 ISSN: 2222-6990.

USGS, (2005). PROJ.4, USGS, http://www.remotesensing.org/proj/

Uysal, M., Toprak, A. S., & Polat, N. (2015). DEM generation with UAV Photogrammetry and Accuracy Analysis in Sahitler Hill. *Measurement,* 73, 539-543.

Van De Sande, B., Lansen, J., & Hoyng, C. (2012). Sensitivity of Coastal Flood Risk Assessments to Digital Elevation Models. *Water Resource*, 4, 568-579.

Vaze, J., Teng, J., & Spencer, G. (2010). Impact of DEM Accuracy and Resolution on Topographic Indices. *Environmental Modelling and Software*, 25(10), 1086–1098. doi: 10.1016/j.envsoft.2010.03.014.

Vila, J.P., Chazel, F., & Noblea, P. (2017). *2D Versus 1D Models for Shallow Water Equations. 24th International Congress of Theoretical and Applied Mechanics.* www.eslvier.com/locate/ proceeding.http://creativecommons.org/licenses/by-nc-nd/4.0/. doi: 10.1016/j.piutam.2017.03.023

Wahl, T., Jain, S., Bender, J., Meyers, S. D., & Luther, M. E. (2015). Increasing Risk of Compound Flooding from Storm Surge and Rainfall for Major US Cities, *Natural Climate Change*, 5, 1093–1097.

Walker, J. P., & Willgoose, G. R. (1999). On the Effect of Digital Elevation Model Accuracy on Hydrology and Geomorphology. *Water Resource*, 35, 2259–2268. doi: 10.1029/1999WR900034

Wang, Y.C, Liu, A., & Tao, F. (2020). Digital Twin Driven Conceptual Design. *Digital Twin Driven Smart Design.* https:// doi. org/ 10. 1016/ B978-0- 12- 818918- 4. 00002-6.

Wechsler, S.P. (2007). Uncertainties Associated with Digital Elevation Models for Hydrologic Applications: A Review. *Hydrology and Earth System Sciences*, 11(4): 1481–1500.

Werner, M. G. (2001). Impact of Grid Size in Flood Mapping Using 1-D Flow GIS-Based Model-Werner.pdf. Physics and Chemistry of Earth, Part B: *Hydrology, Oceans and Atmosphere,* 26(7-8), 517–522.

Wessel, B., Huber, M., Wohlfart, C., Marschalk, U., Kosmann, D. & Roth, A. (2018). Accuracy Assessment of the Global TanDEM-X Digital Elevation Model with GPS data. *ISPRS Journal of Photogrammetry and Remote Sensing*, 139, 171-182

Wing, O. E. J., Bates, P. D., Sampson, C. C., Smith, A. M., Johnson, K. A., & Erickson, T. A. (2017). Validation of a 30 m Resolution Flood Hazard Model of the Conterminous United States. *Water Resources Research*, 53(9), 7968–7986. https://doi.org/10.1002/2017WR020917

Wing, O. E. J., Bates, P. D., Smith, A. M., Sampson, C. C., Johnson, K. A., Joseph, F., & Morefield, P. (2018). Estimates of Present and Future Flood Risk in the Conterminous United States. *Environmental Research Letters*, 13(3), 034023. https://doi.org/10.1088/1748-9326/aaac65

Winsemius, H. C., Aerts, J. C. J. H., van Beek, L. P. H., Bierkens, M. F. P., Bouwman, A., & Jongman, B. (2015). Global Drivers of Future River Flood Risk. *Natural Climate Change*, 6, 381. doi: 10.1038/nclimate2893

Wong, J. S., Freer, J. E., Bates, P. D., Sear, D. A., & Stephens, E. M. (2015). Sensitivity of a Hydraulic Model to Channel Erosion Uncertainty During Extreme Flooding. *Hydrological Processes*, 29, 261-279.

Wood, M., Hostache, R., Neal, J., Wagener, T., Giustarini, L., Chini, M., Corat, O, G., Matgen, P., & Bates, P. (2016). Calibration of Channel Depth and Friction Parameters in the LISFLOOD-FP Hydraulic Model Using Medium-Resolution SAR Data and Identifiability Techniques. *Hydrology and Earth System Sciences*, 20, 4983-4997.

Yague-Martinez, N., Prats-Iraola, P., Gonzalez, F., Brcic, R. Shau, R., Geudtner, D., Eineder, M., & Bamler, R. (2016) "Interferometric Processing of Sentinel-1 TOPS Data", *IEEE Trans. on Geoscience and Remote Sensing*, 54: 1-15, doi: 10.1109/TGRS.2015.2497902.

Yakubu, G. Z. (2012). *An Assessment of Socio-Economic Impacts of the Flood on the Inhabitantants of Galadima Kogo in Shiroro Local Government Area, Niger State, Nigeria.* An unpublished MTech. thesis, Department of Geography, Federal University of Technology, Minna, Niger State, Nigeria.

Yamazaki, D., Ikeshima, D., Tawatari, R., Yamaguchi, T., O'Loughlin, F., Neal, J.C., Sampson, C., Kanae, S., & Bates, P.D. (2017). A High-Accuracy Map of Global Terrain Elevations. *Geophysical Research Letters*. 44(11): 5844–5853. doi: 10.1002/2017GL072874

Yan, K., Tarpanelli, A., Balint, G., Moramarco, T., & Baldassarre, G. D. (2015). Exploring the Potential of SRTM Topography and Radar Altimetry to Support Flood Propagation Modeling: Danube Case Study. *Journal of Hydrologic Engineering*, 20, 04014048.

Yang, Q., Guan, M., Peng, Y., & Chen, H. (2020). Numerical Investigation of Flash Flood Dynamics Due to Cascading Failures of Natural Landslide Dams. *Engineering Geology*. 276, 105765. doi: 10.1016/j.enggeo.2020.105765

Yin, J., Yu, D., & Liao, B. (2020). A City-Scale Assessment of Emergency Response Accessibility to Vulnerable Populations and Facilities Under Normal and Pluvial Food Conditions for Shanghai, China. Environment and Planning B: *Urban Analytics and City Science*. https://doi.org/10.1177/2399808320971304.

Yoon, Y., Durand, M., Merry, C. J., Clark, E. A., Andreadis, K. M., & Alsdorf, D. E. (2012). Estimating river bathymetry from data assimilation of synthetic SWOT measurements. *Journal of Hydrology*, 464-465, 363-375.

Yue, L., Shen, H., Zhang, L., Zheng, X., Zhang, F., & Yuan, Q. (2017). High-Quality Seamless DEM Generation Blending SRTM-1, ASTER GDEM v2 and ICESat/GLAS Observations. *ISPRS Journal Photogrammetry Remote Sensing*. 123, 20–34. doi: 10.1016/j.isprsjprs.2016.11.002

Yu, D., & Lane, S. N. (2006). Urban Fluvial Flood Modelling Using a Two-Dimensional Diffusion-Wave Treatment, Part 1: Mesh Resolution Effects. *Hydrological Processes*, 20, 1541-1565.

Zazo, S., Molina, J. L., & RodriguezGonzalvez, P. (2015). Analysis of Flood Modelling Through Innovative Geomatic Methods. *Journal of Hydrology*, 524, 522-537.

Zhang, J., Huo, A., Zhao, Z., Yang, L., Peng, J., Cheng, Y., & Wang, Z. (2022). Impact of Mountain Reservoir Construction on Groundwater Level in Downstream Loess Areas in Guanzhong Basin, China. *Water*, 14.https://doi.org/10.3390/w14091470

Zhang, K., Gann, D., Ross, M., Robertson, Q., Sarmiento, J., Santana, S., Rhome, J. & Fritz, C. (2019). Accuracy Assessment of ASTER, SRTM, ALOS, and TDX DEMs for Hispaniola and Implications for Mapping Vulnerability to Coastal Flooding. *Remote Sensing of Environment.* 225: 290–306.

Zhang, Y., Xian, C., Chen, H., Grieneisen, M. L., Liu, J., & Zhang, M. (2016). Spatial Interpolation of River Channel Topography Using the Shortest Temporal Distance. *Journal of Hydrology*, 542, 450-462.

Zhao, X., Su, Y., Hu, T., Chen, L., Gao, S., Wang, R., & Jin, S. Q. (2018). A Global Corrected SRTM DEM Product for Vegetated Areas. *Remote Sensing Letters*, 9, 393-402. 313.

Appendix A1: Average monthly rainfall data from 2001 to 2020

Month	2001	2002	2003	2004	2005	2006	2007	2008	2009	2010
Jan	0.00	0.00	0.00	0.00	0.00	0.00	0.00	0.00	0.00	0.00
Feb	0.00	0.00	0.00	0.00	0.00	0.00	0.00	0.00	0.00	0.00
Mar	0.00	0.00	0.00	0.00	0.00	2.40	0.30	0.00	0.00	0.00
Apr	97.60	56.00	58.60	31.30	56.20	34.10	218.40	28.90	106.50	41.10
May	138.90	116.30	118.10	99.40	81.60	121.90	86.50	128.90	128.40	95.80
Jun	159.40	233.80	145.20	165.70	245.70	154.90	223.60	153.90	105.90	162.70
Jul	316.70	286.60	208.30	236.40	229.70	341.70	214.50	305.70	173.90	275.00
Aug	212.70	231.10	351.50	215.10	174.10	266.10	332.30	373.50	398.00	248.00
Sept	360.00	146.10	251.90	214.80	247.10	425.00	282.80	297.60	254.00	247.20
Oct	60.10	98.00	187.10	57.60	72.10	190.80	80.60	53.70	0.00	148.20
Nov	0.00	0.00	0.00	0.00	0.00	0.00	0.00	0.00	0.00	0.00
Dec	0.00	0.00	0.00	0.00	0.00	0.00	0.00	0.00	0.00	0.00
Month	**2011**	**2012**	**2013**	**2014**	**2015**	**2016**	**2017**	**2018**	**2019**	**2020**
Jan	1.00	0.00	0.00	0.00	0.00	0.00	0.00	0.00	0.00	0.00
Feb	0.00	0.00	0.00	0.00	0.00	0.00	0.00	0.57	1.82	0.00
Mar	0.00	0.00	9.80	5.30	70.10	44.45	0.80	0.00	0.00	0.09
Apr	34.00	47.60	96.30	1.90	0.00	123.95	33.95	0.72	1.26	1.87
May	113.70	281.50	65.40	5.20	67.20	136.05	252.80	4.93	8.86	4.34
Jun	83.00	277.70	149.60	252.30	196.10	180.65	105.70	7.56	12.33	7.29
Jul	218.30	310.00	215.00	181.60	239.20	353.30	228.15	11.37	6.58	9.76
Aug	272.90	296.70	221.10	300.10	350.30	320.68	193.70	14.29	11.91	13.26
Sept	368.10	371.00	253.50	327.20	254.20	280.50	312.60	9.64	16.38	12.32
Oct	146.80	75.20	111.40	166.70	52.52	81.30	49.20	2.51	13.54	3.29
Nov	0.00	0.00	0.00	0.00	0.00	0.00	0.00	0.00	0.00	0.00
Dec	0.00	0.00	0.00	0.00	0.00	0.00	0.00	0.00	0.00	0.00

(Source: Shiroro Dam Authorities, 2020)

Appendix A2: Average monthly inflow from 2001 to 2020 used for the study

Month	2001	2002	2003	2004	2005	2006	2007	2008	2009	2010
Jan	57.32	23.23	48.77	32.97	21.55	40.77	51.39	30.42	41.35	64.58
Feb	39.32	12.54	38.61	34.25	17.79	37.96	27.93	26.96	33.79	50.75
Mar	24.77	11.06	19.84	40.55	19.00	28.23	13.19	10.84	13.45	26.39
Apr	27.63	28.87	15.57	26.47	15.57	20.33	34.93	9.87	17.97	18.03
May	88.90	21.97	18.45	72.23	81.16	81.26	69.19	88.61	65.10	96.61
Jun	154.37	237.37	244.00	199.57	166.00	97.73	201.03	168.13	108.40	214.20
Jul	550.48	649.42	576.58	588.23	423.81	469.35	528.74	303.61	279.74	630.52
Aug	901.10	930.84	1327.68	1011.10	680.48	747.19	1048.90	1022.29	1431.29	1149.32
Sep	1246.53	926.10	1752.50	922.10	627.07	1265.63	951.50	1042.20	1130.00	1399.70
Oct	364.74	599.42	492.55	334.23	372.71	878.16	249.39	357.71	500.58	867.81
Nov	130.43	107.43	102.03	73.20	46.50	119.13	95.73	89.00	147.80	163.53
Dec	79.68	59.61	39.55	38.87	38.23	87.29	38.84	61.42	61.71	54.74
Month	**2011**	**2012**	**2013**	**2014**	**2015**	**2016**	**2017**	**2018**	**2019**	**2020**
Jan	68.68	45.19	56.29	45.29	27.29	42.16	41.87	31.97	52.87	67.90
Feb	43.29	20.32	34.46	23.29	14.32	30.71	24.68	19.11	39.36	51.46
Mar	55.26	8.32	35.84	7.42	11.13	19.97	9.55	1.48	47.77	44.42
Apr	26.77	11.27	20.27	27.63	9.20	21.70	14.90	29.83	21.27	33.00
May	77.71	126.58	52.00	159.68	13.55	119.06	168.71	81.65	95.23	104.74
Jun	166.93	366.10	187.47	201.87	130.60	237.70	434.50	286.13	422.60	309.33
Jul	330.10	846.26	671.71	363.48	348.42	713.29	597.06	906.97	653.32	877.71
Aug	768.84	1266.68	750.06	745.39	1181.55	1043.00	865.58	1207.58	943.52	1010.97
Sep	1027.17	2053.47	1197.47	1058.73	1571.43	1300.53	1029.83	1874.67	1408.40	2366.93
Oct	507.58	653.77	421.45	537.16	613.32	425.52	288.71	815.81	1382.26	860.32
Nov	109.77	147.20	127.03	112.40	89.10	106.23	78.30	133.97	316.13	142.73
Dec	57.61	83.16	71.71	54.45	74.10	72.61	39.65	71.19	113.84	92.90

(Source: Shiroro Dam Authorities, 2020)

Appendix A3: Monthly temperature used for the study range from 2001 to 2010

Mon	2001	2002	2003	2004	2005	2006	2007	2008	2009	2010
Jan	22.22	22.73	25.98	26.69	24.26	26.72	22.47	22.88	27.02	25.89
Feb	24.24	28.05	28.74	28.91	29.02	28.02	27.00	25.14	29.18	29.46
Mar	29.27	31.77	30.43	30.57	31.95	29.48	29.18	31.36	29.95	30.16
Apr	29.47	31.16	31.81	30.48	32.08	31.11	31.31	31.40	29.67	32.39
May	28.51	31.37	31.48	28.78	30.40	28.57	29.49	29.77	30.05	30.74
Jun	26.66	28.00	28.69	27.67	28.30	28.63	26.88	29.11	27.64	29.42
Jul	24.91	26.48	26.47	27.48	26.49	26.69	26.14	26.28	27.06	26.73
Aug	24.49	26.48	26.49	26.69	25.82	25.58	25.32	26.34	26.54	26.41
Sep	25.19	26.63	26.58	27.27	27.28	25.90	26.32	27.97	27.25	27.10
Oct	26.25	27.41	28.30	29.76	27.27	26.68	27.35	28.07	27.85	25.98
Nov	26.14	27.53	28.94	30.68	26.83	25.41	27.60	27.69	27.14	27.25
Dec	25.12	25.81	26.45	26.16	25.20	24.15	25.59	27.26	25.00	24.80
Mon	2011	2012	2013	2014	2015	2016	2017	2018	2019	2020
Jan	23.41	23.65	25.10	24.84	21.52	24.97	24.16	20.85	23.03	27.71
Feb	28.94	28.63	27.00	26.03	25.96	27.25	24.32	25.96	23.57	29.66
Mar	30.57	29.46	30.16	29.65	26.74	31.61	28.10	28.45	28.10	32.97
Apr	29.96	30.28	29.73	29.03	27.87	31.37	28.40	28.90	29.27	34.07
May	29.19	27.65	28.23	26.35	27.32	29.58	26.94	26.10	26.65	32.58
Jun	27.57	27.43	26.60	25.71	25.10	28.43	25.37	24.60	25.13	31.60
Jul	27.22	26.09	25.84	24.06	25.56	29.10	24.61	24.26	25.35	32.61
Aug	26.72	26.14	26.68	24.23	24.29	24.58	24.61	24.29	26.00	33.90
Sep	27.45	26.17	26.10	23.94	24.43	25.10	25.27	24.23	27.93	36.50
Oct	28.56	27.19	26.26	25.35	27.97	25.55	26.97	25.87	29.90	39.45
Nov	25.61	27.53	27.20	25.33	28.40	28.10	25.47	25.13	32.07	38.43
Dec	24.87	24.74	25.19	23.06	24.55	24.87	24.10	22.90	2.92	37.87

(Source: Shiroro Dam Authorities, 2020)

Appendix A4: Monthly average water level data from 2001 to 2020

Month	2001	2002	2003	2004	2005	2006	2007	2008	2009	2010
Jan	370.43	374.29	377.14	371.15	376.58	374.26	372.31	373.84	376.75	377.95
Feb	367.97	371.11	375.31	369.78	374.24	370.09	369.55	370.85	373.54	375.76
Mar	365.77	367.49	371.92	368.03	371.31	365.86	366.00	367.48	369.76	371.96
Apr	364.03	362.65	367.13	365.38	367.62	362.86	362.28	363.24	365.29	365.99
May	362.83	360.24	362.80	362.57	363.86	361.05	358.25	358.61	362.98	358.81
Jun	359.98	361.47	360.25	360.79	359.67	361.27	359.37	358.74	355.33	361.61
Jul	362.43	362.53	360.96	360.11	360.47	360.47	359.67	358.55	355.54	361.82
Aug	368.59	368.94	369.61	365.27	353.19	365.71	366.46	368.14	364.65	369.03
Sep	377.61	363.51	380.75	372.53	374.35	376.87	377.51	377.98	378.60	379.97
Oct	381.50	380.60	382.02	375.56	379.70	382.08	379.15	380.42	381.84	382.30
Nov	379.25	379.65	380.80	374.87	380.06	380.15	377.21	378.86	381.78	381.99
Dec	374.48	377.08	378.90	372.91	378.55	377.84	374.69	376.62	379.50	380.26

Month	2011	2012	2013	2014	2015	2016	2017	2018	2019	2020
Jan	370.22	375.42	371.50	370.75	373.98	373.55	373.83	373.83	376.00	377.33
Feb	366.23	372.49	367.24	366.34	370.28	369.83	371.45	371.45	373.21	374.18
Mar	360.86	368.95	362.55	361.99	365.43	365.42	370.87	370.87	369.68	369.67
Apr	358.02	363.59	359.29	358.63	359.02	359.75	369.33	369.33	364.76	364.45
May	357.16	358.24	358.78	356.19	356.78	357.40	364.96	364.96	360.03	359.81
Jun	357.31	358.95	356.81	357.69	356.65	359.41	361.80	359.73	360.02	360.26
Jul	358.42	361.87	361.36	359.23	358.21	362.42	365.21	366.40	364.69	365.77
Aug	361.37	371.11	365.23	361.81	370.81	369.36	369.08	373.60	371.67	375.56
Sep	371.22	380.92	375.27	370.80	380.84	377.77	375.78	382.08	380.07	381.91
Oct	377.35	382.15	379.39	377.31	382.24	382.08	379.85	382.40	382.58	382.51
Nov	376.56	380.93	377.69	377.04	380.59	380.17	378.52	380.98	382.30	381.22
Dec	373.76	378.48	374.98	374.40	377.45	377.20	376.49	378.50	380.15	378.74

(Source: Shiroro Dam Authorities, 2020)

Appendix A5: Monthly outflow data from 2001 to 2020

Month	2001	2002	2003	2004	2005	2006	2007	2008	2009	2010
Jan	76.43	30.97	65.03	43.96	28.73	54.37	68.52	40.56	55.14	86.11
Feb	56.54	19.17	53.67	35.39	21.03	46.68	46.37	36.87	47.68	70.66
Mar	34.41	7.83	32.54	43.52	20.82	37.01	17.01	19.84	23.36	43.93
Apr	9.47	24.15	20.26	16.90	-4.55	5.58	17.54	-13.06	4.05	0.47
May	40.60	-49.10	-56.13	11.34	24.31	50.54	8.03	28.22	30.31	25.37
Jun	-15.59	4.53	33.10	7.27	32.84	-41.87	27.46	76.33	25.26	12.48
Jul	244.92	340.65	145.05	253.62	207.92	206.33	188.26	-11.71	-188.94	251.57
Aug	567.23	735.69	791.86	788.27	540.77	394.09	794.49	670.99	991.65	766.61
Sep	1314.03	971.52	1852.27	1073.45	683.09	1104.28	1133.20	1146.63	1293.69	1365.97
Oct	759.27	887.45	1075.96	667.64	584.91	1206.54	595.21	710.25	882.54	1268.62
Nov	356.97	383.38	447.50	282.79	228.73	492.22	281.19	305.28	421.41	568.16
Dec	198.67	187.41	188.72	133.13	114.47	251.36	132.57	163.18	202.18	244.13
Month	2011	2012	2013	2014	2015	2016	2017	2018	2019	2020
Jan	91.57	60.26	75.05	60.39	36.39	56.22	55.83	42.62	70.49	90.54
Feb	55.39	37.63	47.54	40.94	22.74	42.80	40.11	32.82	46.93	66.84
Mar	64.80	17.11	44.93	11.86	15.64	27.00	17.95	2.48	56.33	55.70
Apr	22.46	-25.22	17.91	-21.64	9.90	-8.99	-35.35	3.44	8.30	16.65
May	29.55	-3.86	-4.52	85.17	-26.69	36.84	12.09	-12.58	-42.87	7.18
Jun	66.75	82.73	-37.94	109.10	5.57	12.21	239.51	-20.38	190.53	19.16
Jul	96.07	451.61	409.04	151.39	-43.58	369.70	388.37	497.65	402.33	547.11
Aug	458.47	732.72	487.26	442.94	643.21	732.72	651.76	748.57	608.16	404.36
Sep	1010.80	2079.78	1219.40	1027.33	1581.40	1402.93	1150.85	1852.26	1150.37	2214.95
Oct	807.92	1297.97	785.57	842.14	1110.75	857.75	646.23	1388.57	1660.34	1551.06
Nov	359.87	552.14	364.99	374.96	434.65	367.95	280.49	573.09	831.63	628.79
Dec	177.57	267.21	193.37	179.44	218.98	195.26	133.14	262.22	391.05	302.50

(Source: Shiroro Dam Authorities, 2020)

Appendix A6: Rainfall and water elevation data

Month	Rainfall	Water elevation
Jan	0.00	375.42
Feb	0.00	372.49
Mar	0.00	368.95
Apr	47.60	363.59
May	281.50	358.24
Jun	277.70	358.95
Jul	310.00	361.87
Aug	296.70	371.11
Sep	371.00	380.92
Oct	75.20	382.15
Nov	*0.00*	380.93
Dec	*0.00*	378.48

(Source: Shiroro Dam Authorities, 2020)

Appendix A7: Rainfall and temperature data

Month	Rainfall	Temperature
Jan	0.00	23.65
Feb	0.00	28.63
Mar	0.00	29.46
Apr	47.60	30.28
May	281.50	27.65
Jun	277.70	27.43
Jul	310.00	26.09
Aug	296.70	25.14
Sep	371.00	23.17
Oct	75.20	27.19
Nov	0.00	27.53
Dec	0.00	24.74

(Source: Shiroro Dam Authorities, 2020)

Appendix A8: Inflow and rainfall data

Month	Inflow	Rainfall
Jan	45.19	0.00
Feb	20.32	0.00
Mar	8.32	0.00
Apr	11.27	47.60
May	126.58	281.50
Jun	366.10	277.70
Jul	846.26	310.00
Aug	1266.68	296.70
Sep	2053.47	371.00
Oct	653.77	75.20
Nov	147.20	0.00
Dec	83.16	0.00

(Source: Shiroro Dam Authorities, 2020)

Appendix A9: Water elevation and inflow data

Month	Water elevation	Inflow
Jan	375.42	45.19
Feb	372.49	20.32
Mar	368.95	8.32
Apr	363.59	11.27
May	358.24	126.58
Jun	358.95	366.10
Jul	361.87	846.26
Aug	371.11	1266.68
Sep	380.92	2053.47
Oct	382.15	653.77
Nov	380.93	147.20
Dec	378.48	83.16

(Source: Shiroro Dam Authorities, 2020)

Appendix A10: Water elevation and Temperature

Month	Water elevation	Temperature
Jan	375.42	23.65
Feb	372.49	28.63
Mar	368.95	29.46
Apr	363.59	30.28
May	358.24	27.65
Jun	358.95	27.43
Jul	361.87	26.09
Aug	371.11	25.14
Sep	380.92	23.17
Oct	382.15	27.19
Nov	380.93	27.53
Dec	378.48	24.74

(Source: Shiroro Dam Authorities, 2020)

Appendix A11: Bathymetric information for the study area

SN	Parameter	Value (m)
i	Minimum depth	0.95
ii	Maximum depth	2.15
iii	Average depth	1.20
iv	Total number of points	955

Appendix A12: NSEMA DATA

Eastings	Northings	Name of Settlement

258846.390	1108098.029	Aguwi
257145.029	1099700.298	Asha
260625.372	1095140.819	Awasha
253325.277	1102602.891	Awolu
247853.178	1104410.981	Baha
238843.032	1117422.097	Bassa
229521.571	1102772.650	Bere
225859.630	1097266.693	Berikago
238843.032	1117422.097	Besse
262476.998	1109844.235	Boladna
246040.699	1111837.516	Dami Dami
253375.100	1109905.412	Daudun Gini
255289.909	1117305.803	Dnakwala
262538.518	1119137.897	Dnakwo
251409.970	1095202.402	Ebbe
255264.982	1113654.567	Farin Dutse
242303.779	1095265.543	Gidan Basakuri
260710.706	1108085.614	Gidan Galadima
255177.254	1100709.326	Gidan Goma
249782.311	1113692.371	Gidan Madaki
236817.876	1095304.678	Gidan Madatsi
231454.805	1111943.507	Gidan Magwi
251575.162	1119212.482	Gidan Mama
260661.718	1100672.773	Gidan Patuko
247918.162	1113705.415	Gidan Sarumai
251434.863	1098853.688	Gidan Tarasilawa
205660.248	1082592.489	Gijiwa
231386.506	1102758.785	Gijiwa
205660.248	1082592.489	Gijiwi
247866.286	1106291.995	Gini
251485.655	1106266.923	Gusuru
227724.893	1097252.709	Guwa
240583.819	1115528.223	Gwadara
240583.819	1115528.223	Gwadara Irina
251510.796	1109918.226	Gwope
266289.827	1122764.322	Iburu
253413.062	1115437.641	Irina
253400.894	1113667.326	Jagabay Ugwa
260759.281	1115387.841	Jagwana
234938.985	1093437.018	Kafa

(Source: NSEMA, 2021)

Appendix A12a: NSEMA DATA

Eastings	Northings	Name of Settlement
236898.013	1106370.189	Kauran Pawa
246093.218	1119251.039	Kawo
247982.902	1122889.240	Kawo
258699.988	1085969.981	Kmakma
216652.413	1084388.044	Kunu
242395.659	1108211.753	Kurmin Gurmana
249629.613	1091563.079	Kuta
258699.988	1085969.981	Kwakwa
238749.089	1104475.542	Kwatayi
220274.697	1084360.397	Kwochi
205748.823	1093660.237	Lawo
225818.126	1091733.561	Layi
205690.264	1086355.517	Luwa
229590.346	1111957.482	Maguga
231454.805	1111943.507	Maowo
231496.220	1117476.490	Masuku
255090.543	1087764.161	Nyagwa
244194.563	1098903.871	Padgaya
205748.823	1093660.237	Rawo
255277.058	1115424.862	Rumpa
207446.577	1086341.521	Sabon Gida
223938.399	1089866.288	Seikna
255189.938	1102590.254	Shaga
260637.709	1097021.682	Shakwada
251498.596	1108147.897	Shamiki
234979.170	1098969.828	Sumaila
246105.811	1121021.437	Tunga Makuba
251575.162	1119212.482	Tunga Mamma Agwagwa
225887.135	1100918.567	Tungan Gamba
246105.811	1121021.437	Tungan Makuba
253438.982	1119199.565	Ungwan Kawo
236738.536	1084239.221	Ungwan Makama
229384.906	1084292.436	Ungwan Zarumayi
253362.920	1108135.102	Yako
249743.852	1108160.027	Yelwa
233333.203	1113810.819	Zangoro
260649.340	1098791.907	Zumba
233333.203	1113810.819	Zungoro

(Source: NSEMA, 2021)

Appendix B1: Discharge rate at selected nodes using DEMs source

ID	UAV 1 m Discharge (m/s^3)	InSAR 10 m Discharge (m/s^3)	SRTM 30 m Discharge (m/s^3)
A01	114.38	114.38	114.38
A02	982.14	1137.03	1154.42
A03	244.82	144.72	219
A04	164.32	166.67	152.48
A05	322.99	327.25	293.92
A06	71.75	183.46	146.16
A07	96.68	53.80	227.45
A08	72.83	115.79	314.13
A09	411.48	561.24	69.9
A10	74.73	74.73	74.73
A11	161.14	161.14	161.14
A12	264.57	264.57	264.57
A13	73.96	73.96	73.96
A14	343.64	343.64	343.64

Appendix B2: Discharge rate differences between UAV, InSAR, and SRTM

ID	UAV-InSAR	InSAR-SRTM	UAV-SRTM
A01	0	0	0
A02	-154.89	-17.39	-172.28
A03	100.1	-74.28	25.82
A04	-2.35	14.19	11.84
A05	-4.26	33.33	29.07
A06	-111.71	37.3	-74.41
A07	42.88	-173.65	-130.77
A08	-42.96	-198.34	-241.3
A09	-149.76	491.34	341.58
A10	0	0	0
A11	0	0	0
A12	0	0	0
A13	0	0	0
A14	0	0	0

Appendix B3: Flow velocity of selected nodes calculated using DEMs source

ID	UAV 1 m Velocity (m/s^2)	InSAR 10 m Velocity (m/s^2)	SRTM 30 m Velocity (m/s^2)
A01	1.27	1.27	1.27
A02	7.71	8.93	9.07
A03	1.71	1.01	1.53
A04	1.2	1.22	1.12
A05	1.48	1.5	1.35
A06	0.46	1.18	0.94
A07	0.45	0.25	1.06
A08	0.46	0.74	1.99
A09	2.56	3.49	0.43
A10	0.43	0.43	0.43
A11	0.91	0.91	0.91
A12	1.46	1.46	1.46
A13	0.43	0.43	0.43
A14	1.72	1.72	1.72

Appendix B4: Flow velocity difference between UAV, InSAR, and SRTM DEMs

ID	UAV-InSAR	InSAR-SRTM	UAV-SRTM
A01	0	0	0
A02	-1.22	-0.14	-1.36
A03	0.7	-0.52	0.18
A04	-0.02	0.1	0.08
A05	-0.02	0.15	0.13
A06	-0.72	0.24	-0.48
A07	0.2	-0.81	-0.61
A08	-0.28	-1.25	-1.53
A09	-0.93	3.06	2.13
A10	0	0	0
A11	0	0	0
A12	0	0	0
A13	0	0	0
A14	0	0	0

Appendix B5: Elevation of the selected nodes for the three DEMs

Sta_ID	Elevation (m)	Elevation (m)	Elevation (m)
A01	348.46	373.32	373.07
A02	348.16	372.12	280.09
A03	251.16	272.64	256.09
A04	212.97	233.35	223.20
A05	198.36	218.35	211.10
A06	197.93	215.55	209.33
A07	195.72	214.86	197.05
A08	194.53	211.86	174.97
A09	174.39	174.39	174.39
A010	174.30	174.30	174.30
A011	167.08	167.08	167.08
A012	159.30	159.30	159.30
A013	159.12	159.12	159.12
A014	128.00	128.00	128.00

Appendix B6: Differences in elevation between UAV, InSAR, and SRTM DEMs

ID	UAV-InSAR	InSAR-SRTM	UAV-SRTM
A01	-24.86	0.25	-24.61
A02	-23.96	92.03	68.07
A03	-21.48	16.55	-4.93
A04	-20.38	10.15	-10.23
A05	-19.99	7.25	-12.74
A06	-17.62	6.22	-11.4
A07	-19.14	17.81	-1.33
A08	-17.33	36.89	19.56
A09	0	0	0
A10	0	0	0
A11	0	0	0
A12	0	0	0
A13	0	0	0
A14	0	0	0